(2)

NSWCDD/TR-92/503

TRACKING FILTERS FOR PRECISION ELECTRONIC SUPPORT MEASURES (ESM) SYSTEMS

BY J. DARREN PARKER
ELECTRONIC WARFARE SYSTEMS DIVISION
SHIP DEFENSE SYSTEMS DEPARTMENT

DECEMBER 1992

NAVAL SURFACE WARFARE CENTER
DAHLGREN DIVISION
Dahlgren, Virginia 22448-5000

NSWCDD/TR-92/503

TRACKING FILTERS FOR PRECISION ELECTRONIC SUPPORT MEASURES (ESM) SYSTEMS

BY J. DARREN PARKER
ELECTRONIC WARFARE SYSTEMS DIVISION
SHIP DEFENSE SYSTEMS DEPARTMENT

DECEMBER 1992

NAVAL SURFACE WARFARE CENTER
DAHLGREN DIVISION
Dahlgren, Virginia 22448-5000

FOREWORD

This work supports an ongoing effort at the Naval Surface Warfare Center, Dahlgren Division (NSWCDD) to determine effective algorithms for correlating tracks from radar and Electronic Support Measures (ESM) systems with angular measurement accuracies on the order of 0.1 deg. This research investigated two tracking filters that can be used in an ESM system to generate bearing and elevation tracks and was performed in support of the Surface-Launched Weaponry Technology Block.

This report was reviewed by Larry Sumner, Electronic Warfare Systems Integration Branch, Tom Kimbrell, Head, Electronic Warfare Systems Integration Branch; and Richard Lee, Head, Electronic Warfare Systems Division.

Approved by:

T. C. Pendergraft, Head

Ship Defense Systems Department

ABSTRACT

Both an α,β and an α,β,γ filter have been used to estimate the true bearing and elevation of high-speed maneuvering targets from measurements made by a shipboard electronic support measures (ESM) sensor. The motivation for this research is the need for correlating radar and ESM tracks. Four Mach 3 target trajectories with a data rate of 10 Hz and a measurement noise standard deviation of 0.1 deg were used to test the filters. Consistency tests were used to determine the best values for the steady-state gains of the filters. Both filters are computationally simple and provide estimates of greater accuracy than the ESM measurements. It was determined that an α,β filter provides better estimates than an α,β,γ filter for most of the tested target trajectories. Two exceptions are the bearing for a Mach 3 crossing target at ranges less than 20 km and the elevation of a Mach 3 target at ranges less than 5 km. Both filters are recommended for radar-to-ESM track correlation research. The α,β filter should be tested first since it is simpler and provides better estimates for most of the cases tested.

CONTENTS

ILLUSTRATIONS

ILLUSTRATIONS (CONTINUED)

ILLUSTRATIONS (CONTINUED)

ILLUSTRATIONS (CONTINUED)

ILLUSTRATIONS (CONTINUED)

CHAPTER 1
INTRODUCTION

Electronic support measures (ESM) sensors detect and make measurements on electromagnetic energy emitted from radar systems in the environment; these measurements include frequency, pulse width, pulse amplitude, pulse repetition interval, and intra-pulse modulations. However, the only measurements that can be used to track the kinematics of the target are bearing and elevation.

The primary requirement for having tracking filters in a shipboard ESM system comes from the need to correlate ESM tracks with the tracks of radars and other onboard sensors. It is not necessary for the ESM system to be able to determine the target's position in three-dimensional space since the radar tracks provide this information. However, it is necessary for the ESM system to provide accurate angle rate estimates in order to reliably correlate its tracks with those of the radar, so that these systems can be used cooperatively against all threats.

Another requirement for the ESM system is to track hundreds of platforms at once, which will force the tracking filters to be computationally simple. For this reason, this research investigated two of the more computationally simple tracking filters known. Further research will be performed to determine the effectiveness of these filters for correlating radar and ESM tracks. If these filters prove inadequate for this function, then other more complex tracking filters will be investigated for this purpose.

A single type of tracking filter will not likely provide adequate performance for all targets since an ESM sensor must track many targets with widely varying capabilities for maneuvering and with widely varying pulse repetition intervals. However, ESM sensors can associate measurements with the correct target with a high probability of success due to the large number

of parameters they measure and their target identification abilities. Therefore, the target tracking function for an ESM sensor can use the emitter identification information to assign an appropriate tracking filter for each target based on the platform type; e.g., the ESM tracking algorithm can have a table of filter gains and data rates based on platform type (missile, attack aircraft, ships, etc.). Then, the appropriate gains and data rates can be chosen to track that particular platform.

The research discussed here concentrates on evaluating the performance of two computationally simple tracking filters against highly maneuverable Mach 3 targets using an extremely slow data rate (i.e., on the order of 10 Hz). For slower targets, both filters can be adjusted to provide better estimates by decreasing the process noise variance (i.e., the steady state gains). Likewise, if the ESM sensor can give a higher data rate, then the tracking filter can be adjusted to improve the quality of the estimates. Therefore, further research must be performed using slower targets and faster data rates in order to obtain optimal performance from the tracking filters discussed in this report.

The tracking filters for radar sensor applications have generally been implemented in Cartesian coordinates. This is possible because the radar measures all three spherical coordinates (range, bearing, and elevation), so a transformation to Cartesian coordinates can be performed. Most shipboard ESM sensors do not make range measurements because to do so requires either a maneuver of the sensor platform or triangulation of angle measurements from two or more sensors. This research assumed that no range measurement is available since the targets of interest can perform maneuvers of greater magnitude than a ship. As discussed by Gorecki, range is unobservable by a passive sensor unless the sensor platform performs maneuvers (in directions orthogonal to the line of sight) of at least one order of magnitude greater than the maneuvers performed by the target.[1] Also, triangulation will likely require a data link between ships which may not be available at all times.

A tracking algorithm that has been successfully implemented in aircraft passive sensor applications is the Modified Spherical Coordinates (MSC) angle-only filter.[2,3] It uses the Extended Kalman Filter and states that are defined in the MSC coordinate system in a manner that

decouples the range estimate from the angle and angle rate estimates to prevent degradation of the quality of the angle and angle rate estimates when good range estimates are not available. The aircraft can only obtain good range estimates using passive sensors by maneuvering when the target is not maneuvering or by triangulation using measurements from the passive sensors of other platforms. If effective and reliable techniques for obtaining range estimates using shipboard ESM sensors are developed, then the MSC angle-only filter should be considered. However, the lack of passive ranging techniques and the computational complexity of the MSC angle-only filter make it an unlikely candidate to accomplish the goals of this research.

An α,β and an α,β,γ filter have been tested as ESM tracking filters against four different target trajectories. Both filters track bearing and elevation measurements independently. Both filter designs are based on the assumption that the true bearing and elevation measurements are uncorrelated. The true bearing and elevation will be correlated with range; but, as stated above, it is assumed that no range measurements are available. Consistency tests are used to determine appropriate values for the process noise variances. Results are presented to demonstrate that both filters provide adequate bearing and elevation estimates for all of the tested trajectories. Significance tests of the differences in mean squared errors are used to compare the performance of the α,β and the α,β,γ filters. It is shown that the α,β filter provides better estimates for most of the trajectories tested.

CHAPTER 2
FILTER DESCRIPTIONS

The two tracking filters tested are both standard Kalman filters operating on the bearing and elevation measurements independently. The only difference in the two tracking filters is the number of states estimated; the α,β filter uses a constant first derivative prediction matrix (referred to as a 2 state filter), and the α,β,γ filter uses a constant second derivative prediction matrix (referred to as a 3 state filter). The Kalman filter equations are presented first followed by the prediction matrices for the 2 and 3 state filters.

The Kalman filter equations are presented in order to define several terms that will be used in later sections. The first step performed by a Kalman filter is to predict the current estimate and its covariance to the time of the next measurement using the equations

$$\hat{x}_{k+1|k}=F_k\hat{x}_{k|k} \tag{2.1}$$

$$P_{k+1|k}=F_kP_{k|k}F_k^T+Q_k \tag{2.2}$$

where $\hat{x}_{j|k}$ is the state estimate at time j given the measurements up to time k, $P_{j|k}$ is its covariance, F_k is the state transition matrix, and Q_k is the covariance of the process noise.[4] The next step is to calculate the covariance of the innovations and then the filter gain using the equations

$$S_{k+1}=H_{k+1}P_{k+1|k}H_{k+1}^T+R_{k+1} \tag{2.3}$$

$$W_{k+1}=P_{k+1|k}H_{k+1}S_{k+1}^{-1} \tag{2.4}$$

where H_k is the measurement matrix, R_k is the covariance of the measurement noise, S_k is the

covariance of the innovation (defined below), and W_k is the filter gain.[4] The last step is to calculate the innovation, the new state estimate, and its covariance using the equations

$$v_{k+1}=z_{k+1}-H_{k+1}\hat{x}_{k+1|k} \tag{2.5}$$

$$\hat{x}_{k+1|k+1}=\hat{x}_{k+1|k}+W_{k+1}v_{k+1} \tag{2.6}$$

$$P_{k+1|k+1}=P_{k+1|k}-W_{k+1}S_{k+1}W_{k+1}^{T} \tag{2.7}$$

where z_k is the measurement at time k and v_k is the innovation.[4]

These Kalman filter equations are used for both the 2 and 3 state tracking filters. The only differences between these filters are the matrices F_k and Q_k in Equations (2.1) and (2.2) above. For the 2 state filter, F_k is given by[5]

$$F_k=\begin{bmatrix}1 & T\\ 0 & 1\end{bmatrix} \tag{2.8}$$

where T is the time step between measurements; for the 3 state filter, F_k is given by[5]

$$F_k=\begin{bmatrix}1 & T & \frac{1}{2}T^2\\ 0 & 1 & T\\ 0 & 0 & 1\end{bmatrix} \tag{2.9}$$

The process noise covariance matrix, Q_k , is given by

$$Q_k=G_k^{T}q_kG_k \tag{2.10}$$

where q_k is the process noise variance that must be set by the filter designer, and the vector, G_k, corresponds to the F_k for the filter.[5] For the 2 state filter with F_k in Equation (2.8), G_k

is given by

$$G_k=\left[\frac{1}{2}T^2 \quad T\right] \tag{2.11}$$

and by[5]

$$G_k=\left[\frac{1}{2}T^2 \quad T \quad 1\right] \tag{2.12}$$

for the 3 state filter with F_k in Equation (2.9).[5]

CHAPTER 3
CONSISTENCY TESTS

Several consistency tests can be used to match the process noise variance, q_k, in Equation (2.10) to a particular target trajectory. The consistency tests that are performed for Monte Carlo simulations are described first, followed by descriptions of the tests that can be performed on a single run.

The consistency tests for Monte Carlo simulations of tracking filters are performed on the sample average of the normalized state estimation error squared, the sample average of the normalized innovation squared, and the sample autocorrelation statistic of the innovations. The normalized state estimation error squared is given by

$$\epsilon_k = \tilde{x}_{k|k}^T P_{k|k}^{-1} \tilde{x}_{k|k} \tag{3.1}$$

where

$$\tilde{x}_{k|k} = x_k - \hat{x}_{k|k} \tag{3.2}$$

is the difference between the true state and the state estimate at time k.[4] The sample average of ϵ_k is computed over all of the Monte Carlo runs by the equation[4]

$$\bar{\epsilon}_k = \frac{1}{N} \sum_{i=1}^{N} \epsilon_k^i \tag{3.3}$$

The sample average, $\bar{\epsilon}_k$, is compared to a confidence region defined by thresholds obtained from a Chi-squared table. If $\bar{\epsilon}_k$ is within the confidence region, the filter's errors are consistent with the filter's covariances. A similar test is performed on the sample average of the normalized

innovation squared. The normalized innovation squared is computed by the equation[4]

$$\epsilon_k^{\nu} = \nu_k^T S_k^{-1} \nu_k \tag{3.4}$$

The sample average of ϵ_k^{ν} is denoted by $\bar{\epsilon}_k^{\nu}$. The last consistency test for Monte Carlo simulations uses a sample autocorrelation statistic of the innovations that is computed by the equation[4]

$$\bar{\rho}_{kj} = \sum_{i=1}^{N} (\nu_k^i)^T \nu_j^i \left[\sum_{i=1}^{N} (\nu_k^i)^T \nu_k^i \sum_{i=1}^{N} (\nu_j^i)^T \nu_j^i \right]^{-\frac{1}{2}} \tag{3.5}$$

The filter's innovations are considered uncorrelated (or white) if $\bar{\rho}_{kj}$ is within a confidence region defined by thresholds taken from a table of the Normal density function.

The consistency tests of the innovations can also be performed on a single run of the filter by using time averages instead of sample averages. The test statistic for consistent innovations in a single run is

$$\bar{\epsilon}^{\nu} = \frac{1}{K} \sum_{k=1}^{K} \nu_k^T S_k^{-1} \nu_k \tag{3.6}$$

and the test statistic for the autocorrelation of the innovations in a single run is[4]

$$\bar{\rho}_l = \sum_{k=1}^{K} (\nu_k)^T \nu_{k+l} \left[\sum_{k=1}^{K} (\nu_k)^T \nu_k \sum_{k=1}^{K} (\nu_{k+l})^T \nu_{k+l} \right]^{-\frac{1}{2}} \tag{3.7}$$

CHAPTER 4
FILTER COMPARISONS

A comparison between two tracking filters can be made using a significance test of the sample mean of the differences in squared error. Comparing the root-mean-squared errors (RMSE) alone is not effective because a confidence region is needed to determine if the differences in RMSE are significant. The hypothesis that algorithm 1 is better than algorithm 2 is accepted if the sample mean of the differences in squared error given by

$$\mu = \frac{\bar{\Delta}}{\sigma_{\bar{\Delta}}} \tag{4.1}$$

is greater than a threshold taken from a table of the Normal density.[4] In Equation (4.1),

$$\bar{\Delta} = \frac{1}{N}\sum_{i=1}^{N}\left(C_i^2 - C_i^1\right)^2 \tag{4.2}$$

is the sample mean of the differences in squared error where C_i^m is the squared error for algorithm m at a particular time and

$$\sigma_{\bar{\Delta}}^2 = \frac{1}{N^2}\sum_{i=1}^{N}\left(\Delta_i - \bar{\Delta}\right)^2 \tag{4.3}$$

is the variance of the differences in squared error.[4]

CHAPTER 5
FILTER INITIALIZATION

The procedure for choosing the initial estimates and their covariances is described in this section. For the 2 state filter, the initial estimate is computed from[4]

$$\hat{x}_{0|0}=\left[z_0 \quad (z_0-z_{-1})/T\right]^T \tag{5.1}$$

Similarly, the initial estimate for the 3 state filter is computed from

$$\hat{x}_{0|0}=\begin{bmatrix} z_0 \\ (z_0-z_{-1})/T \\ (z_0-2z_{-1}+z_{-2})/T^2 \end{bmatrix} \tag{5.2}$$

The covariances are given by[4]

$$P_{0|0}=\begin{bmatrix} R_0 & R_0/T \\ R_0/T & 2R_0/T^2 \end{bmatrix} \tag{5.3}$$

for the 2 state filter and by

$$P_{0|0}=\begin{bmatrix} R_0 & R_0/T & R_0/T^2 \\ R_0/T & 2R_0/T^2 & 3R_0/T^3 \\ R_0/T^2 & 3R_0/T^3 & 6R_0/T^4 \end{bmatrix} \tag{5.4}$$

for the 3 state filter.

CHAPTER 6
TARGET TRAJECTORIES

ESM measurements can be generated by converting trajectories formed in Cartesian coordinates into spherical coordinates and adding pseudorandom noise sequences to the bearing and elevation data. Two unrealistic but reasonable assumptions make the generation of the target trajectories easier. One is to assume the earth is flat, which is reasonable for the short ranges used in the trajectories discussed in this report; the other is to assume the ESM sensor is at zero altitude. This assumption causes the true elevation measurements to always be positive. For an actual shipboard system tracking a sea skimming missile, the true elevation measurements will be negative. However, the magnitude of the true elevation rate is the same in either case, so the positive elevation measurements are considered to be reasonable. Zero mean pseudorandom number sequences with a white Gaussian distribution are used to add errors to the true bearing and elevation. A standard deviation of 0.1 deg (1.73 mrad) and a data rate of 10 Hz is used for all the simulations discussed here. For Monte Carlo simulations, a new pseudorandom number sequence is generated for each run, so the measurement errors are independent from run to run.

Four different target trajectories were generated to test the ESM tracking filters; all are Mach 3 targets that remain at constant altitude. The ESM sensor is located at the origin for all four trajectories. The first target moves in a straight line directly towards the sensor; it is referred to as the radial target. The second target moves in a straight line on a crossing trajectory; it is referred to as the crossing target. The third target moves in a straight line towards the sensor and performs a single S-turn in the middle of the trajectory; it is referred to as the S-turn target. The last target is a radial target that performs jinking type maneuvers; it is referred to as the jinking target. Each of these trajectories is presented (all of the figures referred to in this section are located in Appendix A).

6.1 RADIAL TARGET

The radial target starts at XY coordinates (25 km, 0 m) and ends at (510 m, 0 m). The true bearing, elevation, and elevation rate for this target are shown in Figures A-1, A-2, and A-3, respectively. The target maintained a constant altitude of 20 m and a constant speed of Mach 3 (1029 m/s) throughout the trajectory. The elevation increases almost linearly until about 20 s into the trajectory, where it increases rapidly because the target is at close range.

6.2 CROSSING TARGET

A plot of the XY plane view of the crossing target is given in Figure A-4. The crossing target starts at XY coordinates (10 km, -23 km) and ends at (10 km, 23 km). These points are labeled 't=0' and 't=41.0' in Figure A-4. The closest point of approach occurs midway through the trajectory at a range of 10 km. The target maintained a constant altitude of 20 m and a constant speed of Mach 3 (1029 m/s) throughout the trajectory. The true bearing and bearing rate for this target are shown in Figures A-5 and A-6, respectively. As shown is Figure A-6, the largest absolute value of the bearing rate occurs at 20 s into the trajectory, and the maximum change in the bearing rate occurs at 10 and 30 s into the trajectory. The true elevation and elevation rate for this target are shown in Figures A-7 and A-8, respectively.

6.3 S-TURN TARGET

A plot of the XY plane view of this trajectory is given in Figure A-9. The target starts at XY coordinates (25 km, -925 m), and ends at (1.95 km, -58 m). The target maintained a constant altitude of 30.5 m and a constant speed of Mach 3 (1006 m/s) throughout the trajectory. The target moves in a straight line for 10 s. It then performs a 15 g, constant speed turn towards the positive Y direction for 2.5 s and then a 15 g, constant speed turn towards the negative Y direction for 2.5 s. The target moves in a straight line towards the ESM sensor for the last 8 s of the trajectory. The velocities and accelerations for this trajectory are shown in Figures A-10 and A-11. Notice in Figure A-11 that there are no instantaneous changes in the acceleration because they were filtered through a second-order system. The true bearing, bearing rate, elevation, and elevation rate are shown in Figures A-12, A-13, A-14, and A-15, respectively.

6.4 JINKING TARGET

A plot of the XY plane view of this trajectory is given in Figure A-16. The target starts at XY coordinates (25 km, 0 m), and ends at (1.06 k ٦, 0 m). These points are labeled 't=0.0' and 't=23.8' in Figure A-16. Also, every 10th data point is labeled with an 'O' in the figure for clarity. The target maintained a constant altitude of 50 m and a constant speed of Mach 3 (1006 m/s) throughout the trajectory. The target moves in a straight line for 5 s. It then begins jinking maneuvers that last until 21.8 s through the trajectory. The term jinking maneuver refers to alternating accelerations orthogonal to the velocity vector. The velocities and accelerations for this target are shown in Figures A-17 and A-18, respectively. The Z velocity for this target is zero and is not shown in Figure A-17. Likewise, the X and Z accelerations are zero and are not shown in Figure A-18. The Y acceleration changes instantaneously from +15 g to -15 g. The accelerations were not filtered through the second-order system to make it easier to direct the target toward the ESM sensor located at the origin. The target moves in a straight line towards the ESM sensor for the last 2 s of the trajectory. The true bearing, bearing rate, elevation, and elevation rate are shown in Figures A-19, A-20, A-21, and A-22, respectively. Notice in Figures A-19 and A-20 that the jinking maneuvers cause faster changes in the bearing as the target closes in range.

CHAPTER 7
PROCESS NOISE VARIANCE SELECTION

The filter consistency tests are used to select the best value of the process noise variance for each filter for each trajectory. The single run tests are used to determine a reasonable range of values for the process noise variance, and the Monte Carlo simulations are performed to find the best value for the variance. An explanation of the procedures used to select the thresholds for the consistency tests are given. Then, the variances chosen for each filter for each trajectory are presented. This chapter concludes with an example of the procedure used to select the process noise variance for a filter.

7.1 CONSISTENCY TEST THRESHOLDS

The sample average of the normalized state estimation error squared, $\bar{\epsilon}_k$, given by Equation (3.3), is tested during Monte Carlo simulations. This statistic is compared to a threshold from a Chi-square table and has Nn_x degrees-of-freedom (DOF) where N is the number of Monte Carlo runs and n_x is the number of states estimated by the filter.[4] The 95-percent confidence region for the 2 state filter (a 95-percent confidence region was used in the tests for all statistics) is 1.5 to 2.6 since there are 100 DOF (N=50 and n_x=2) and the limits from the table (74.2 and 129.6) must be divided by N. Similarly, the confidence region for the 3 state filter is 2.2 to 3.9 since there are 90 DOF (N=30 and n_x=3) and the limits from the table (65.6 and 118.1) must be divided by N.

The normalized innovations, ϵ_k^{ν} given by Equation (3.4), is tested during Monte Carlo simulations and single runs of the filters. Both test statistics are Chi-squared distributed, but with a different number of DOF. The sample average statistic, $\bar{\epsilon}_k^{\nu}$, has Nn_z DOF where n_z is the number of measurements for each estimate (1 for all cases considered here). The confidence region for the 2 state filter is 0.65 to 1.43 since there are 50 DOF (N=50 and n_z=1) and the limits from the table are 32.3 and 71.4. Similarly, the confidence region for the 3 state filter is 0.56 to 1.57 since there are 30 DOF (N=30 and n_z=1) and the limits from the table are 16.8 and 47.0. The time average statistic, $\bar{\epsilon}^{\nu}$ given by Equation (3.6), has Kn_z DOF, where K is the number of estimates used to compute the average. The confidence region for both the 2 and 3 state filters is 0.74 to 1.3 since the time averages were computed using blocks of 100 estimates. Only 100 estimates were used since the largest degree of freedom listed in the Chi-squared tables is 100. For DOF greater than 100, the statistic is approximately Gaussian.[4] However, the author chose to limit the number of estimates used to compute the average to 100 instead of approximating the distribution by a Gaussian.

The sample autocorrelation statistic, $\bar{\rho}_{kj}$ given by Equation (3.5), is tested during Monte Carlo simulations, and the time average autocorrelation statistic, $\bar{\rho}_l$ given by Equation (3.7), is tested during single run tests. Only the single step difference autocorrelation statistic is computed in all cases (i.e., k-j=1 for $\bar{\rho}_{kj}$). For large N, $\bar{\rho}_{kj}$ is approximately normal with variance $1/N$, so the confidence region is taken from a table of the Normal distribution.[4] The confidence region for $\bar{\rho}_{kj}$ is ± 0.28 for the 2 state filter and ± 0.36 for the 3 state filter. Likewise, for large K, $\bar{\rho}_l$ is approximately normal with variance $1/K$.[4] The confidence region for $\bar{\rho}_l$ is ± 0.2 for both the 2 state filter and the 3 state filter since both use averages of 100 estimates.

7.2 CHOSEN VALUES FOR PROCESS NOISE VARIANCES

The value of the process noise variance, q_k, was chosen as the maximum value for which the filter did not violate any of the Monte Carlo simulation consistency tests. This is the most effective method for selecting the process noise variance since the process noise accounts for all of the modeling inaccuracies of the Kalman filter. The Kalman filter's constant state transition matrix is the dominate cause of these modeling inaccuracies. The test of $\bar{\epsilon}_k$ was relaxed to include values smaller than the lower threshold defining the confidence region since this was the case for both filters on all of the trajectories. This condition indicates that the filter's covariances predict larger errors than reality (i.e., the filter is pessimistic). The q_k chosen for each filter for each trajectory are presented in Table 1. The units for all the values shown in the table are rad^2/s^4.

TABLE 1. CHOSEN VALUES OF PROCESS NOISE VARIANCE

Trajectory	2 State Filte.		3 State Filter	
	Bearing	Elevation	Bearing	Elevation
Radial	10^{-3}	10^{-3}	10^{-3}	10^{-3}
Crossing	10^{-4}	10^{-4}	10^{-6}	10^{-6}
S-Turn	10^{-3}	10^{-7}	10^{-5}	10^{-7}
Jinking	5×10^{-3}	5×10^{-4}	5×10^{-4}	5×10^{-6}

7.3 EXAMPLE OF PROCESS NOISE VARIANCE SELECTION

The $\bar{\epsilon}_k^{\nu}$ and $\bar{\rho}_{kj}$ of the bearing for 30 Monte Carlo runs of the 3 state filter on the crossing trajectory are shown in Figures B-1 and B-2 which are located in Appendix B. In these figures, the area between the horizontal lines is the 95-percent confidence region. The Y axis label in Figure B-1, 'SAMPLE AVG NORM INNOV - BEAR' denotes the $\bar{\epsilon}_k^{\nu}$ for the bearing

innovations. Likewise, the Y axis label 'SAMPLE AUTOCORR INNOV - BEAR' in Figure B-2 denotes the $\bar{\rho}_{kj}$ for the bearing innovations. Notice in these figures that most of the $\vec{\epsilon}_k^{\nu}$ and $\bar{\rho}_{kj}$ are within the confidence region and the mean of $\vec{\epsilon}_k^{\nu}$ over the trajectory is close to one and the mean of $\bar{\rho}_{kj}$ is close to zero. The q_k for this filter was 10^{-6}. Other Monte Carlo simulations for this filter were performed with q_k of 10^{-5} and 10^{-7}. For $q_k=10^{-5}$, more of the $\vec{\epsilon}_k^{\nu}$ and $\bar{\rho}_{kj}$ were below the lower threshold of the confidence region, and their means were not as close to their optimum values of 1 and 0, respectively. For $q_k=10^{-7}$, a significant number of the $\vec{\epsilon}_k^{\nu}$ and $\bar{\rho}_{kj}$ exceeded the upper threshold of the confidence region at the middle of the trajectory where the change in bearing approaches zero as shown in Figures B-3 and B-4. Thus, the designer selected $q_k=10^{-6}$ for this filter and trajectory. This procedure was repeated for all four trajectories for both filters to select the q_k shown in Table 1.

CHAPTER 8
RESULTS

The techniques described were utilized to evaluate the performance of 2 and 3 state filters for four target trajectories. The results of the 2 state filter are given first followed by the results for the 3 state filter. Finally, comparisons of the performance of the 2 and 3 state filters are presented.

8.1 RESULTS FOR 2 STATE FILTER

The following subsections are organized in the same manner. Sample bearing, bearing rate, elevation, and elevation rate estimates from a single run of the 2 state filters are presented. Then, the RMSE for these estimates from 50 Monte Carlo runs of the 2 state filters are presented. Each subsection concludes with plots of the consistency test statistics from 50 Monte Carlo runs of the 2 state filters. All of the figures referred to in this section are located in Appendix C.

8.1.1 Radial Target

The bearing, bearing rate, elevation, and elevation rate estimates from a single run of the 2 state filters on the radial target are shown in Figures C-1, C-2, C-3, and C-4, respectively. The true states are plotted in each figure for reference. These figures are intended to give the reader an intuitive understanding of the quality of the estimates generated by the filters. Since these estimates are from a single run of the filters, no conclusions on the average performance of the filters should be drawn from them.

The RMS bearing, bearing rate, elevation, and elevation rate errors from 50 Monte Carlo runs of the 2 state filters on the radial target are shown in Figures C-5, C-6, C-7, and C-8, respectively. The horizontal lines in Figures C-5 and C-7 correspond to the standard deviation of the measurement noise (0.1 deg or 1.74 mrad) and is provided as a reference to determine the

amount of noise removed by the filter. In Figure C-5, the RMS bearing error has been reduced from 1.74 mrad to 1 mrad. In Figure C-6, the RMS bearing rate error is 2.8 mrad/s. In Figure C-7, the RMS elevation error has been reduced from 1.74 mrad to 1 mrad through most of the trajectory, but the error increases rapidly in the last second of the trajectory. This occurs because the filter assumes the elevation increases linearly, but the true elevation is increasing much faster than a linear slope. The same effect can be seen in the elevation rate estimates. The author is not concerned about the large errors in the elevation and elevation rate estimates during the last second of the trajectory since the target is within 2 km of the ship. When the missile reaches a range of 2 km from the ship, the radar-to-ESM correlation should have already been completed. Also, the accuracy of the elevation estimates will still be sufficient to support the electronic countermeasures (ECM) system since it will use beamwidths that are much larger than the elevation errors.

Plots of the consistency test statistics from 50 Monte Carlo runs of the 2 state filters on the radial target are given in Figures C-9 through C-14. The area between the horizontal lines is the 95-percent confidence region. The Y axis labels used in these figures are defined as follows: 'SAMPLE AVG NORM INNOV' denotes $\bar{\epsilon}_k^{\nu}$ given by Equation (3.4), 'SAMPLE AUTOCORR INNOV' denotes $\bar{\rho}_{kj}$ given by Equation (3.5), and 'NORM STATE EST ERROR SQUARED' denotes $\bar{\epsilon}_k$ given by Equation (3.3). The Chi-square test of the bearing innovations is given in Figure C-9. Most of the points are within the 95-percent confidence region, so the bearing innovations are consistent with their covariances. The Chi-square test of the elevation innovations is given in Figure C-10. This figure shows that the elevation innovations are consistent until the last seconds of the trajectory. For reasons mentioned previously, this is not a reason for concern. The whiteness test of the bearing innovations is shown in Figure C-11. For this figure and all subsequent whiteness tests, only the $\bar{\rho}_{kj}$ for $k-j=1$ is shown. As shown in this figure, the innovations are roughly uncorrelated. The whiteness test for the elevation innovations is shown in Figure C-12. The innovations become significantly correlated at the end of the trajectory due to the large errors in the elevation estimates. The Chi-square test of the bearing estimation error is shown in Figure C-13. The confidence region is not shown since the thresholds are on the

order of one. Since the test data are much smaller than the lower threshold, the author concludes that the filter's error covariances, P_k given by Equation (2.2), predict larger errors than actually occur (i.e., the filter is pessimistic). This condition is considered acceptable since it is not critical that the P_k predict the exact amount of error in the estimates; it is only important that the P_k do not underestimate the amount of error in the estimates. This is equivalent to using a one-sided confidence region instead of a two-sided confidence region. A one-sided confidence region will used on all subsequent Chi-square tests of the state estimation error. The Chi-square test of the elevation estimation error is shown in Figure C-14. The data up to 22 s through the trajectory are on the order of 10^{-5} and cannot be seen in the figure. The large errors in the elevation and elevation rate estimates cause the sharp increase in $\bar{\epsilon}_k$ in the last seconds of Figure C-14. Again, the missile is at a very short range at this point, so large elevation estimate errors are not significant. Thus, all of the consistency tests passed. so the process noise variances used for these simulations are good values.

8.1.2 Crossing Target

The bearing, bearing rate, elevation, and elevation rate estimates from a single run of the 2 state filters on the crossing target are shown in Figures C-15 through C-18. In Figure C-15, the difference between the sample bearing estimate and the true bearing is too small to be seen. The errors in the sample bearing rate estimate in Figure C-16 are smallest in the middle of the trajectory where the bearing rate is nearly constant for a short time. This makes sense because the state transition matrix, F_k given by Equation (2.8), assumes that the true bearing rate is constant. In Figure C-17, the sample elevation estimate looks similar to the sample bearing estimate for the radial target shown in Figure C-1 since the true elevation remains almost constant over the trajectory. Similarly, the sample elevation rate estimate for the crossing target shown in Figure C-18 looks almost the same as the sample bearing rate estimate for the radial target shown in Figure C-2.

The RMS bearing, bearing rate, elevation, and elevation rate errors from 50 Monte Carlo runs of the 2 state filters on the crossing target are shown in Figures C-19, C-20, C-21, and C-22,

respectively. In Figure C-19, the correlation between the accuracy of the state transition matrix, F_k, and the accuracy of the estimates is demonstrated clearly. At the beginning, middle, and end of the trajectory where the true bearing rate is nearly constant, the RMS bearing error is at its minimum of 0.8 mrad (a 54-percent reduction from the 1.74 mrad measurement noise standard deviation). At the 15-s and 27-s points of the trajectory, the bearing rate is changing at its maximum rate, so the RMS bearing error is at its maximum of 1.4 mrad (only a 19.5-percent reduction from 1.74 mrad). The same correlation can be easily seen in the RMS bearing rate errors shown in Figure C-20. The minimum RMS bearing rate error occurs at the midpoint of the trajectory at 1.25 mrad/s, and the maximum error occurs at the 15-s and 27-s points at 4.25 mrad/s. In Figure C-21, the RMS elevation error has been reduced from 1.74 mrad to 0.8 mrad. The RMS elevation rate error remains at 1.25 mrad/s throughout the trajectory as shown in Figure C-22.

Plots of the consistency test statistics from 50 Monte Carlo runs of the 2 state filters on the crossing target are given in Figures C-23 through C-28. The Chi-square test of the bearing innovations is given in Figure C-23. Notice that a large number of the points are outside the 95-percent confidence region at the 15-s and 27-s points of the trajectory which indicates that the bearing innovations are not consistent with their covariances. However, if the process noise variance, q_k, is increased to improve the consistency of the innovations at these two points of the trajectory, then the innovations near the beginning, middle, and end of the trajectory will become less consistent. It was determined through many Monte Carlo simulations that the bearing innovations for this trajectory cannot be made more consistent than that shown in Figure C-23. In Figure C-24, it is shown that the elevation innovations are very consistent through the entire trajectory. This is not surprising since the true elevation rate is virtually constant, and the F_k predicts a constant elevation rate. The whiteness test of the bearing innovations is shown in Figure C-25. This test has the same problems that were encountered for the Chi-square test of the bearing innovations shown in Figure C-23. Again, it was found through Monte Carlo simulations that any attempt to reduce the positive correlation of the bearing innovations by increasing q_k will cause an increase in the negative correlation in the other parts of the

trajectory. The whiteness test for the elevation innovations in Figure C-26 shows that they are indeed uncorrelated in time. The Chi-square test of the bearing estimation error is shown in Figure C-27. The bearing estimation error is consistent using a one-sided confidence region. Using a two-sided confidence region, this filter is clearly pessimistic. The Chi-square test of the elevation estimation error in Figure C-28 demonstrates that they are consistent. As in the radial target case, all of the consistency tests passed, so the process noise variances used for these simulations are good values.

8.1.3 S-turn Target

The bearing, bearing rate, elevation, and elevation rate estimates from a single run of the 2 state filters on the S-turn target are shown in Figures C-29 through C-32. In Figure C-29, the reader can see that the bearing estimate follows the true bearing maneuver fairly well, but the estimates are somewhat noisy before and after the S-turn maneuver. This is a result of choosing the q_k large to allow significant deviations in the true bearing. The same is true of the bearing rate estimate in Figure C-30. In Figure C-31, the sample elevation estimate looks similar to the sample elevation estimate for the radial target shown in Figure C-3. However, the elevation estimate in Figure C-31 lags the true elevation to a larger degree than does the one in Figure C-3. This is due to the large differences in the q_k for the two filters. Referring to Table 1, the q_k for the elevation of the radial target was chosen as 10^{-3}, which allows the filter to follow the changes in the true elevation more closely at the expense of degraded estimates when the true elevation does not change. The q_k for the S-turn target was chosen as 10^{-7}, which tightens the filter's estimates causing it to lag behind the changes in the true elevation. Since the true elevation for these two targets is similar, comparing the sample elevation estimates from these two filters provides a good intuitive understanding of the relationship between q_k and the performance of the filter. As shown in Figure C-32, the lag in the elevation rate estimates is even more dramatic.

The RMS bearing, bearing rate, elevation, and elevation rate errors from 50 Monte Carlo runs of the 2 state filters on the S-turn target are shown in Figures C-33 through C-36. In Figure C-33, the RMS bearing error remains nearly constant throughout the trajectory at about 1.1 mrad

(a 37-percent reduction from the 1.74 mrad measurement noise standard deviation). Notice that one cannot easily see where the maneuver occurs near the middle of the trajectory. As discussed in the previous paragraph, this is caused by the rather large q_k chosen for this filter and trajectory. In Figure C-34, the maneuver is easier to see in the RMS bearing rate errors. If the q_k where smaller, then the RMS bearing rate error before and after the maneuver would be smaller, but it would be larger during the maneuver. In Figure C-35, the RMS elevation error is about 0.5 mrad in the middle of the trajectory which is a reduction of 71-percent from 1.74 mrad. However, at the end of the trajectory the elevation errors are growing quickly which is the consequence of having a small q_k. The RMS elevation rate error (Figure C-36) is very small in the middle of the trajectory but grows quickly at the end as did the RMS elevation error.

Plots of the consistency test statistics from 50 Monte Carlo runs of the 2 state filters on the S-turn target are given in Figures C-37 through C-42. The Chi-square test of the bearing innovations is given in Figure C-37. Most of the points are within the 95-percent confidence region, but the time average of these points is approximately 0.9 which indicates that the q_k is slightly too large. In Figure C-38, the elevation innovations are consistent until the end when the true elevation is changing quickly. The whiteness test of the bearing innovations (Figure C-39) indicates the bearing innovations have a slight negative correlation before and after the maneuver (which begins at the 10-s point and ends at the 15-s point) and have a slight positive correlation during the maneuver. This test indicates that the q_k cannot be made smaller since the bearing innovations will have a stronger correlation during the maneuver. In light of this test, the reader can appreciate why the q_k was not decreased. The whiteness test for the elevation innovations in Figure C-40 gives the same indications that the Chi-square test of the elevation innovations did in Figure C-38. The elevation innovations are uncorrelated until the end of the trajectory. The Chi-square tests of the bearing and elevation estimation error are shown in Figures C-41 and C-42, respectively. As was the case for both the radial and the crossing targets, they are consistent using a one-sided confidence region. As in the previous two target cases, all of the consistency tests passed, so the process noise variances used for these simulations are good values.

8.1.4 Jinking Target

The bearing, bearing rate, elevation, and elevation rate estimates from a single run of the 2 state filters on the jinking target are shown in Figures C-43 through C-46. In Figures C-43 and C-44, the bearing and bearing rate estimates follow the true bearing and bearing rate through the jinking maneuvers reasonably well. The q_k was intentionally chosen large to allow significant deviations in the true bearing similarly to the S-turn target discussed previously. In Figure C-45, the sample elevation estimate looks similar to the sample elevation estimates for the radial and S-turn targets shown in Figures C-3 and C-31, respectively. The jinking target elevation estimate in Figure C-45 is more similar to the radial target elevation estimate in Figure C-3 since the q_k for these filters are nearly the same (from Table 1, 5×10^{-4} for the jinking target and 1×10^{-3} for the radial target). Figure C-46 shows that the elevation rate estimate does not have a large lag behind the true elevation rate as one would except for a filter with a large q_k.

The RMS bearing, bearing rate, elevation, and elevation rate errors from 50 Monte Carlo runs of the 2 state filters on the jinking target are shown in Figures C-47 through C-50. In Figure C-47, the RMS bearing error remains nearly constant throughout the trajectory at about 1.3 mrad (a 25-percent reduction from the 1.74 mrad measurement noise standard deviation). As for the S-turn target, one cannot easily see where the maneuvers occur. In Figure C-48, one can see the jinking maneuvers toward the end of the trajectory in the RMS bearing rate errors. In Figure C-49, the RMS elevation error is about 0.9 mrad until the end of the trajectory which is a reduction of 48-percent from 1.74 mrad. The RMS elevation rate error (Figure C-50) is steady at about 2.2 mrad/s until the end of the trajectory where it grows quickly.

Plots of the consistency test statistics from 50 Monte Carlo runs of the 2 state filters on the jinking target are given in Figures C-51 through C-56. The Chi-square test of the bearing innovations is given in Figure C-51. Most of the points are within the 95-percent confidence region. The time average of the bearing innovations over the first 17 s of the trajectory is less than the optimum value of 1, but the time average from 17 to 22 s is very close to 1, which indicates that the q_k is too large over the first 17 s and is close to optimum from 17 to 22 s. In

Figure C-52, the elevation innovations are consistent until the end when the true elevation is changing quickly. Since more points fall below the confidence region than above, the q_k could have been decreased, but this would cause the elevation innovations to leave the confidence region more quickly at the end of the trajectory. The whiteness test of the bearing innovations (Figure C-53) indicates the bearing innovations have a significant negative correlation until about 17 s into the trajectory where the magnitude of the bearing rate changes are becoming large. The whiteness test for the elevation innovations (Figure C-54) shows they are slightly correlated until the end of the trajectory where they become strongly correlated. The Chi-square tests of the bearing and elevation estimation error are shown in Figures C-55 and C-56, respectively. As was the case for all of the previous targets, they are consistent using a one-sided confidence region. For the jinking target, the consistency tests passed (although not with flying colors), so the process noise variances used for these simulations are good values.

8.2 RESULTS FOR 3 STATE FILTER

The format of this section is the same as the one used in Section 8.1. Sample bearing, bearing rate, elevation, and elevation rate estimates from a single run of the 3 state filters are presented. Then, the RMSE from 30 Monte Carlo runs are presented. Each subsection concludes with plots of the consistency test statistics from these simulations to verify that the values chosen for the process noise variances are appropriate. All of the figures referred to in this section are located in Appendix D.

The results for the bearing rate rate and elevation rate rate estimates are not presented. This omission is justified for two reasons. First, this work is intended to support radar-to-ESM correlation studies, and most radar systems can provide angle and angle rate estimates but not angle rate rate estimates. Secondly, the reader can interpolate the results presented for the angle and angle rate estimates to determine the approximate performance of the 3 state filters for the angle rate rate estimates.

8.2.1 Radial Target

The bearing, bearing rate, elevation, and elevation rate estimates from a single run of the 3 state filters on the radial target are shown in Figures D-1, D-2, D-3, and D-4, respectively. The bearing and bearing rate estimates in Figures D-1 and D-2 are rather noisy, which illustrates one of the disadvantages to using an excessively high-order filter. The filter is estimating both the first and second derivatives of the bearing, and from these figures, it is obvious that the true first and second derivatives are zero. Therefore, the filter is wasting information (i.e., the measurements) by trying to estimate states that are zero. Figures D-3 and D-4 show that the elevation and elevation rate estimates are somewhat noisy in the first 20 s of the trajectory, but the looseness in the filter allows the estimates to follow the quick increase of the true elevation and rate fairly well.

The RMS bearing, bearing rate, elevation, and elevation rate errors from 30 Monte Carlo runs of the 3 state filters on the radial target are shown in Figures D-5 through D-8. The horizontal lines in Figures D-5 and D-7 correspond to the standard deviation of the measurement noise (0.1 deg or 1.74 mrad) and is provided as a reference to determine the amount of noise removed by the filter. In Figure D-5, the RMS bearing error has been reduced from 1.74 mrad to about 1.3 mrad, which is a 25-percent decrease. In Figure D-6, the RMS bearing rate error is approximately 8 mrad/s. In Figure D-7, the RMS elevation error has been reduced from 1.74 mrad to 1.4 mrad, which is a 20-percent decrease. In Figure D-8, the RMS elevation rate error remains at about 8 mrad/s until the end of the trajectory where the sharp rise in the true elevation rate causes the errors to increase quickly.

Plots of the consistency test statistics from 30 Monte Carlo runs of the 3 state filters on the radial target are given in Figures D-9 through D-14. The area between the horizontal lines is the 95-percent confidence region (refer to Section 8 1 for an explanation of the Y axis labels used in these figures). The Chi-square test of the bearing innovations is given in Figure D-9. Most of the points are within the 95-percent confidence region, so the bearing innovations are consistent with their covariances. Since the time average of these points is close to 0.8, the q_k could actually be slightly smaller than it is. The Chi-square test of the elevation innovations

presented in Figure D-10 shows that the elevation innovations are consistent. The whiteness test of the bearing innovations is shown in Figure D-11. For this figure and all subsequent whiteness tests, only the $\bar{\rho}_{kj}$ for $k-j=1$ is shown. As shown in this figure, the innovations have a slight negative correlation, which is another indication that the q_k could have been smaller. The whiteness test for the elevation innovations shown in Figure D-12 is similar to that of the bearing innovations. They have a slight negative correlation. The Chi-square test of the bearing estimation error is shown in Figure D-13. The confidence region is not shown since the thresholds are on the order of one. As was the case for the 2 state filters, the 3 state filters are usually pessimistic. For this reason, a one-sided confidence region will be used on most of the following Chi-square tests of the state estimation error. The Chi-square test of the elevation estimation error is shown in Figure D-14. The data up to 24 s through the trajectory are on the order of 10^{-3} and cannot be seen in the figure. The large errors in the elevation rate rate estimates are the major cause for the sharp increase in $\bar{\epsilon}_k$ in the last second of Figure D-14. Again, the missile is at a very short range at this point, so large elevation estimate errors are not significant. Thus, all of the consistency tests passed, so the process noise variances used for these simulations are good values.

8.2.2 Crossing Target

The bearing, bearing rate, elevation, and elevation rate estimates from a single run of the 3 state filters on the crossing target are shown in Figures D-15 through D-18, respectively. In Figure D-15, the difference between the sample bearing estimate and the true bearing is too small to be seen. The errors in the sample bearing rate estimate in Figure D-16 are about the same magnitude through the entire trajectory. The sample elevation and elevation rate estimates shown in Figures D-17 and D-18 are somewhat noisy and are similar to the bearing and bearing rate estimates for the radial target shown in Figures D-3 and D-4.

The RMS bearing, bearing rate, elevation, and elevation rate errors from 30 Monte Carlo runs of the 3 state filters on the crossing target are shown in Figures D-19, D-20, D-21, and D-22, respectively. In Figure D-19, the RMS bearing error is approximately 0.9 mrad throughout the trajectory, which is a 48-percent reduction from the 1.74 mrad measurement noise standard

deviation. The RMS bearing rate error remains virtually constant at 1.8 mrad/s. There is a slight increase in the RMS error around the 20-s point, which is a result of the true bearing rate rate approaching zero at this point. In Figure D-21, the RMS elevation error has been reduced from 1.74 mrad to 0.8 mrad which is a 54-percent reduction. The RMS elevation rate error remains at 1.5 mrad/s throughout the trajectory as shown in Figure D-22.

Plots of the consistency test statistics from 30 Monte Carlo runs of the 3 state filters on the crossing target are given in Figures D-23 through D-28. All of these consistency tests passed, so the chosen values for q_k are appropriate.

8.2.3 S-turn Target

The bearing, bearing rate, elevation, and elevation rate estimates from a single run of the 3 state filters on the S-turn target are shown in Figures D-29 through D-32. In Figure D-30, the largest error in the sample bearing rate estimate occurs at about the 13-s point where the bearing rate rate changes quickly.

The RMS bearing, bearing rate, elevation, and elevation rate errors from 30 Monte Carlo runs of the 3 state filters on the S-turn target are shown in Figures D-33 through D-36. In Figure D-33, the RMS bearing error remains nearly constant throughout the trajectory at about 1.1 mrad (a 37-percent reduction from the 1.74 mrad measurement noise standard deviation). The maneuver that occurs near the middle of the trajectory cannot be seen in the RMS bearing errors. In Figure D-34, the maneuver is easier to see in the RMS bearing rate errors which vary between 3 mrad/s and 6 mrad/s. In Figure D-35, the RMS elevation error is about 0.8 mrad throughout the trajectory, which is a reduction of 54-percent from 1.74 mrad. At the end of the trajectory, the elevation errors are growing but do not exceed the 1.74-mrad line. The RMS elevation rate error (Figure D-36) is steady at 1 mrad/s until the end where it begins increasing.

Plots of the consistency test statistics from 30 Monte Carlo runs of the 3 state filters on the S-turn target are given in Figures D-37 through D-42. The Chi-square tests of the bearing and elevation estimation errors are shown in Figures D-41 and D-42, respectively. As was the case for both the radial and the crossing targets, they are consistent using a one-sided confidence region.

The large peaks that appear in these figures are primarily due to the large errors in the angle rate rates. As in the previous two target cases, all of the consistency tests passed, so the process noise variances used for these simulations are good values.

8.2.4 Jinking Target

The bearing, bearing rate, elevation, and elevation rate estimates from a single run of the 3 state filters on the jinking target are shown in Figures D-43 through D-46. In Figures D-43 and D-44, the bearing and bearing rate estimates follow the true bearing and bearing rate through the jinking maneuvers reasonably well. In Figure D-45, the sample elevation estimate looks similar to the sample elevation estimates for the radial and S-turn targets shown in Figures D-3 and D-31, respectively.

The RMS bearing, bearing rate, elevation, and elevation rate errors from 30 Monte Carlo runs of the 3 state filters on the jinking target are shown in Figures D-47 through D-50. In Figure D-47, the RMS bearing error is approximately 1.3 mrad (a 25-percent reduction from the 1.74 mrad measurement noise standard deviation). In Figure D-48, one can see the jinking maneuvers toward the end of the trajectory in the RMS bearing rate errors. In Figure D-49, the RMS elevation error is about 1 mrad until the end of the trajectory which is a reduction of 43-percent from 1.74 mrad. The RMS elevation rate error (Figure D-50) is steady at about 2.2 mrad/s until the end of the trajectory where it grows quickly.

Plots of the consistency test statistics from 30 Monte Carlo runs of the 3 state filters on the jinking target are given in Figures D-51 through D-56. All the consistency tests passed, so the process noise variances used for these simulations are good values.

8.3 COMPARISON OF 2 AND 3 STATE FILTERS

The reader may have noticed that little effort has been made to compare the results of the 2 and 3 state filters in the previous sections. This section was included to fill this void. Monte Carlo simulations were performed and the statistic given by Equation (4.1) was computed to compare the bearing, bearing rate, elevation, and elevation rate estimates from the 2 and 3 state

filters. The results of these simulations are presented in this section. All of the figures referred to in this section are located in Appendix E.

In all of the figures, if the comparison statistic is above the upper threshold, then the hypothesis that the 2 state filter's estimates are better than the 3 state filter's estimates is accepted. Likewise, if the comparison statistic is below the lower threshold, then the hypothesis that the 3 state filter's estimates are better than the 2 state filter's estimates is accepted. If the comparison statistic is between the two thresholds, then neither hypothesis is accepted. Both thresholds correspond to 95-percent probabilities that the hypothesis is correct.

8.3.1 Radial Target

Plots of the results of a comparison between the 2 and 3 state filters for 50 Monte Carlo runs using the radial target are shown in Figures E-1 to E-4. The performance of the 2 state filter was significantly better than that of the 3 state filter since all of the test statistics are greater than the upper threshold that defines the 95-percent confidence region. The only exception is the elevation statistics in the last few seconds of the trajectory (Figures E-3 and E-4). Here the true elevation has a significant second derivative, and the 3 state filter's estimates are better.

8.3.2 Crossing Target

Plots of the results of a comparison between the 2 and 3 state filters for 50 Monte Carlo runs using the crossing target are shown in Figures E-5 to E-8. In Figures E-5 and E-6, the bearing and bearing rate comparison statistics are below the lower threshold for most of the trajectory, so the 3 state filter's bearing and bearing rate estimates are better. Notice at the 21-s point of the trajectory that the 2 state filter's estimates are better since the true bearing rate rate is approximately zero. From Figures E-7 and E-8, the 2 state filter's elevation and elevation rate estimates are better throughout the trajectory.

8.3.3 S-turn Target

Plots of the results of a comparison between the 2 and 3 state filters for 50 Monte Carlo runs using the S-turn target are shown in Figures E-9 to E-12. Figures E-9 and E-10 show that

both filters give bearing and bearing rate estimates of approximately the same quality. In the first turn on the S-turn, which occurs from 10 s to 12.5 s in these figures, the 3 state filter's estimates appear to be better. However, not enough points fall below the lower threshold to justify a conclusion that the 3 state filter's estimates are superior. In Figures E-11 and E-12, all of the points before the 20 s point are above the upper threshold, so the 2 state filter's estimates are better. The 3 state filter's estimates are definitely better during the last few seconds of the trajectory.

8.3.4 Jinking Target

Plots of the results of a comparison between the 2 and 3 state filters for 50 Monte Carlo runs using the jinking target are shown in Figures E-13 to E-16. In Figures E-13 and E-14, most of the points are above the upper threshold until the last few maneuvers occur from 17s to 21 s. Thus, the 2 state filter's bearing and bearing rate estimates are better until the end of the trajectory. In Figures E-15 and E-16, most of the points fall between the two thresholds, so neither filter's elevation and elevation rate estimates are better. Of course, in the last few seconds of the trajectory, the 3 state filter's estimates are better.

CHAPTER 9
CONCLUSIONS AND RECOMMENDATIONS

Two Kalman filters were tested for estimating the true bearing, bearing rate, elevation, and elevation rate of high-speed targets using simulated measurements from a shipboard ESM receiver. The two Kalman filters tested were described in terms of the state transition matrix. The 2 state filter predicts the true state using a constant first derivative assumption, and the 3 state filter predicts the true state using a constant second derivative assumption. The steady state versions of these filters are the well known α,β and an α,β,γ filters. The steady state filters would be used in an actual implementation since they are computationally simpler. The Kalman filter versions were used in the research to simplify the coding of the algorithms.

Consistency tests were described as an effective method to determine the best process noise variance (i.e., the steady state gains) for each filter for each target trajectory tested. An example of this method of process noise variance selection was presented.

The four target trajectories used to test the tracking filters were presented. All were Mach 3 targets with a data rate of 10 Hz and a measurement noise standard deviation of 0.1 deg (1.74 mrad). Two targets moved in straight lines, and the other two performed maneuvers with 15-g accelerations.

A statistic that can be used to compare the estimates generated by two tracking filters was presented. This statistic was used to compare the bearing, bearing rate, elevation, and elevation rate estimates from the 2 and 3 state filters for all four target trajectories. The 2 state filter gave better bearing and bearing rate estimates for all targets except the crossing target. The 3 state filter's bearing and bearing rate estimates were superior for most of the crossing trajectory. The 2 state filter also gave better elevation and elevation rate estimates for all of the targets.

However, for the radial, S-turn, and jinking targets, the 3 state filter's elevation and elevation rate estimates were better in the last few seconds of the trajectories since the true elevation rate was changing quickly.

Both filters are recommended for radar-to-ESM track correlation research. The 2 state filter should be tested first since it is simpler and provides better estimates for most of the cases tested.

CHAPTER 10
REFERENCES

1. Gorecki, Frank D., "More On Angle-Only-Track, Observability and Information Theory," in AIAA Guidance, Navigation, and Control Conference, A Collection of Technical Papers, Part 1, Portland, OR, August 20-22, 1990, American Institute of Aeronautics and Astronautics, Washington, D. C., 1990, pp. 782-785.

2. Stallard, David V., "Angle-Only Tracking Filter in Modified Spherical Coordinates," in Journal of Guidance, Control, and Dynamics, Vol. 14, No. 3, May-June 1991, American Institute of Aeronautics and Astronautics, Washington, D. C., 1991, pp. 694-696.

3. Blackman, Samuel S., "Tracking Algorithm Descriptions," Hughes Aircraft Company, Electro-Optical and Data Systems Group, El Segundo, CA 90245, 1990.

4. Bar-Shalom, Yaakov and Thomas E. Fortmann, *Tracking and Data Association*, Academic Press, Inc., San Diego, CA 92101, 1988.

5. Kalata, Paul R., "The Tracking Index: A Generalized Parameter for $\alpha-\beta$ and $\alpha-\beta-\gamma$ Target Trackers," *IEEE Transactions on Aerospace and Electronic Systems*, Vol. AES-20, No. 2, March 1984, pp. 174-182.

APPENDIX A
PLOTS OF TARGET TRAJECTORIES

This appendix presents the four target trajectories used to test the 2 and 3 state filters. The trajectories are presented in the following order: radial target, crossing target, S-turn target, and jinking target.

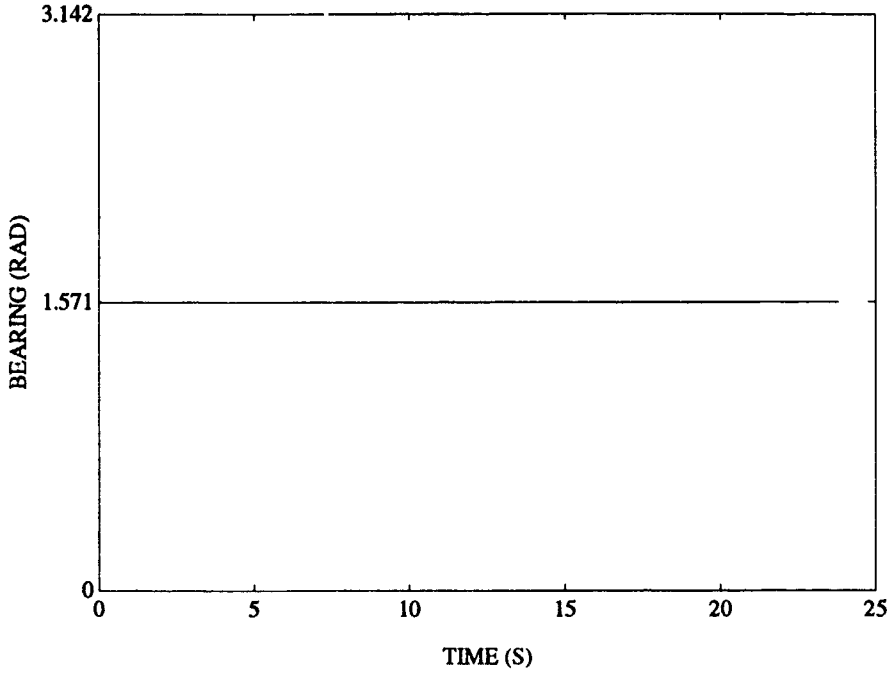

FIGURE A-1. TRUE BEARING FOR RADIAL TARGET

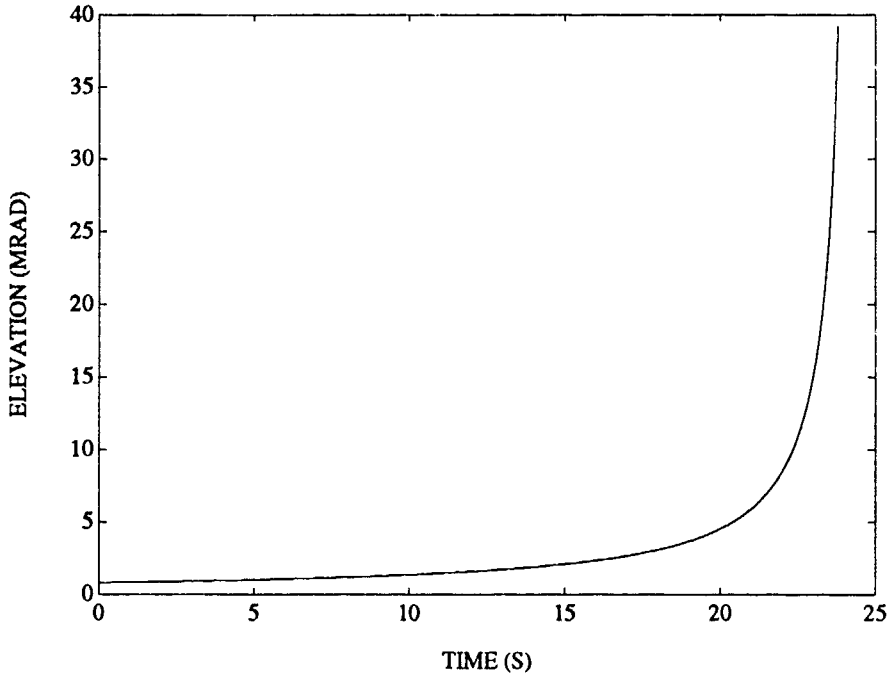

FIGURE A-2. TRUE ELEVATION FOR RADIAL TARGET

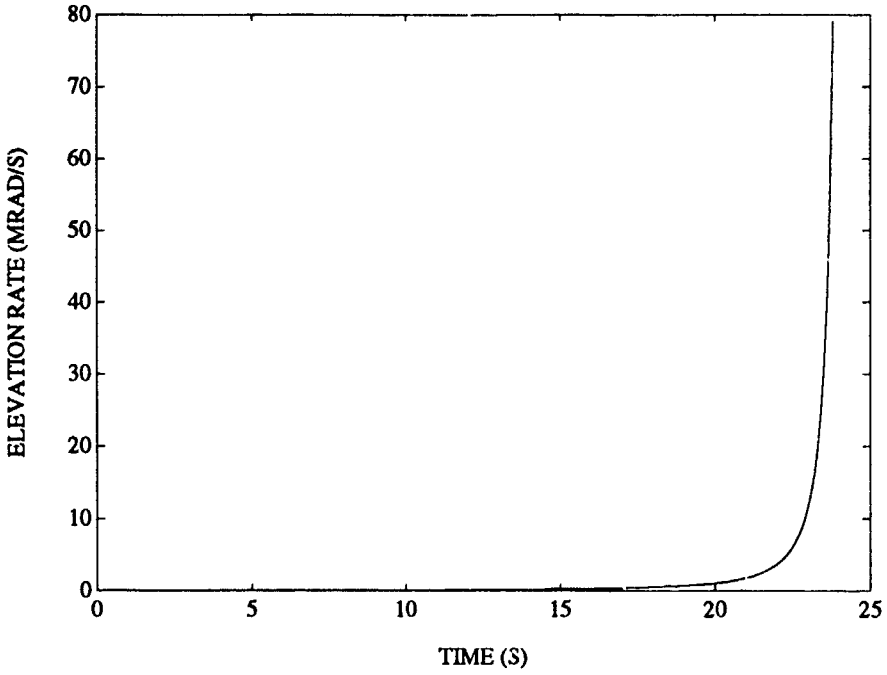

FIGURE A-3. TRUE ELEVATION RATE FOR RADIAL TARGET

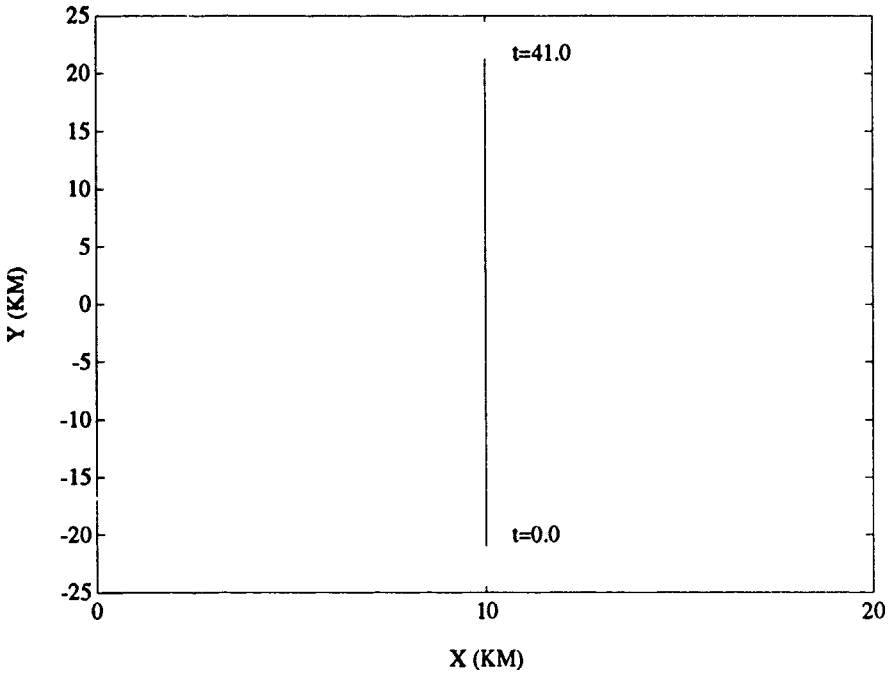

FIGURE A-4. X-Y PLANE FOR CROSSING TARGET

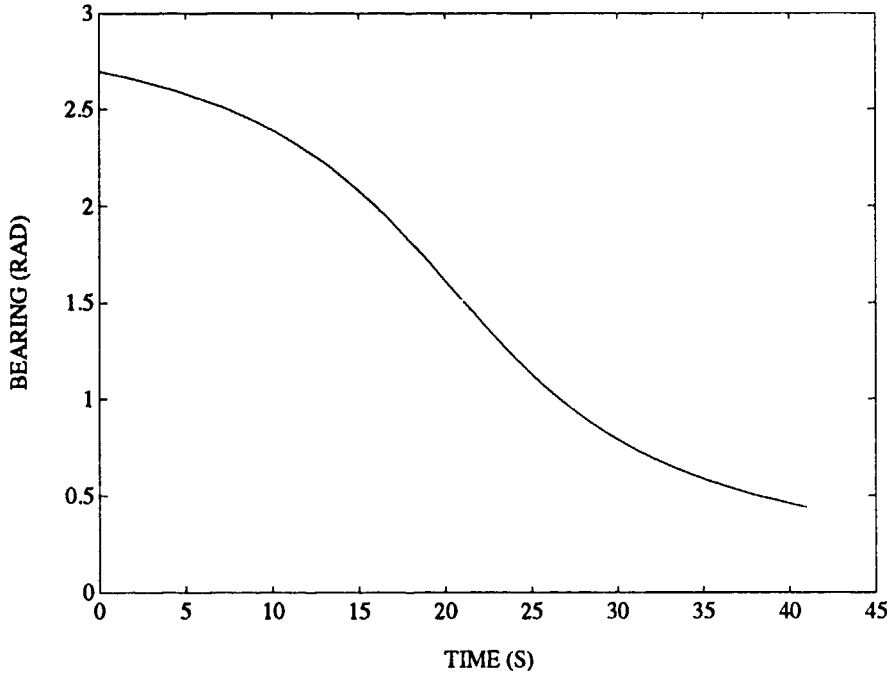

FIGURE A-5. TRUE BEARING FOR CROSSING TARGET

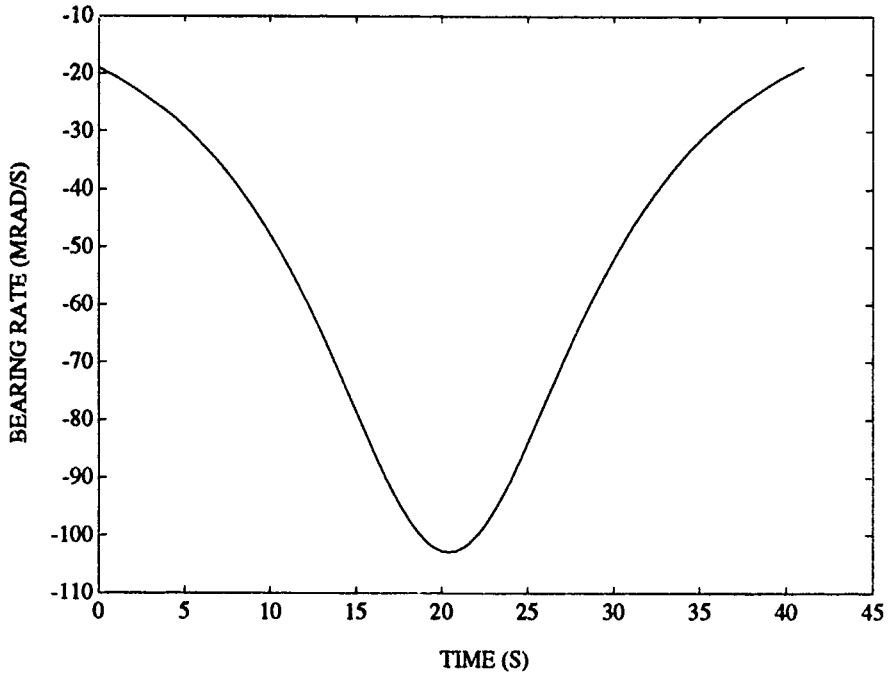

FIGURE A-6. TRUE BEARING RATE FOR CROSSING TARGET

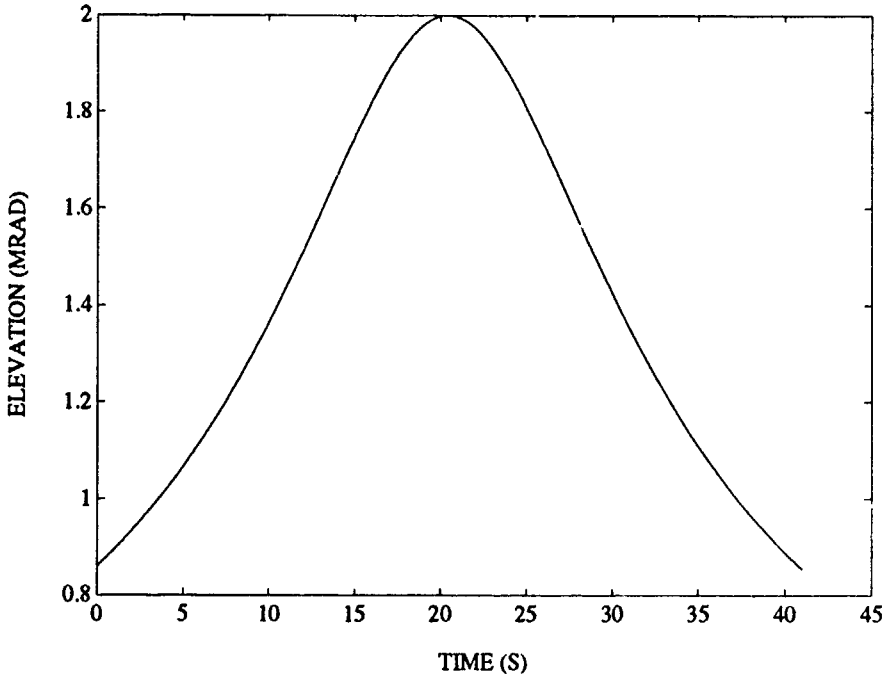

FIGURE A-7. TRUE ELEVATION FOR CROSSING TARGET

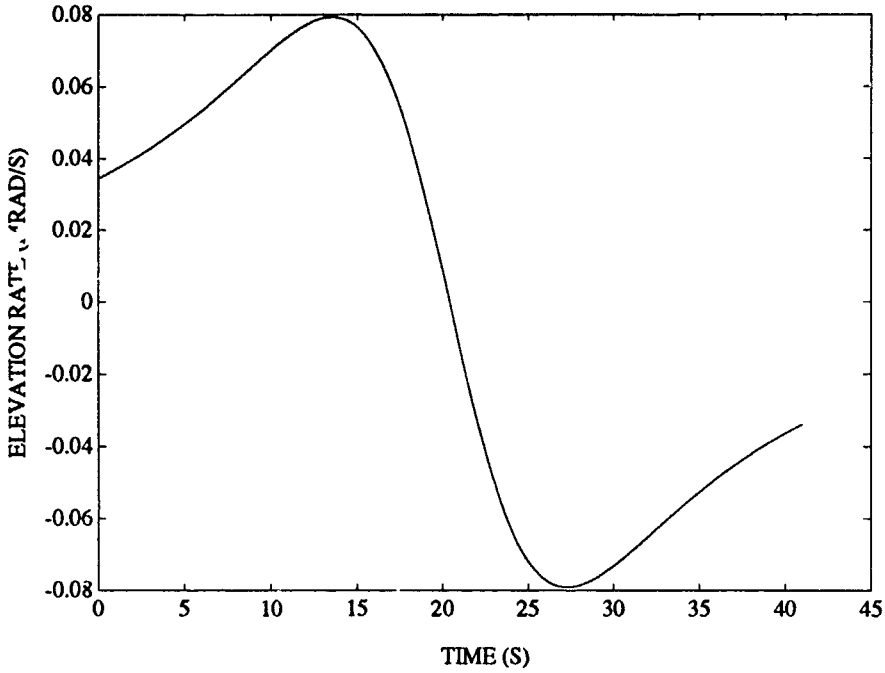

FIGURE A-8. TRUE ELEVATION RATE FOR CROSSING TARGET

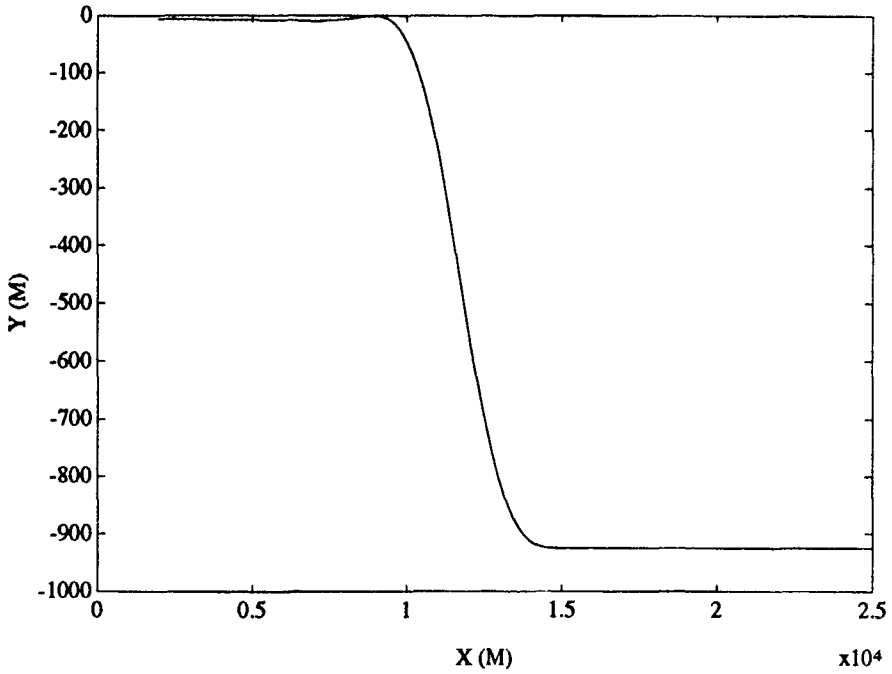

FIGURE A-9. X-Y PLANE FOR S-TURN TARGET

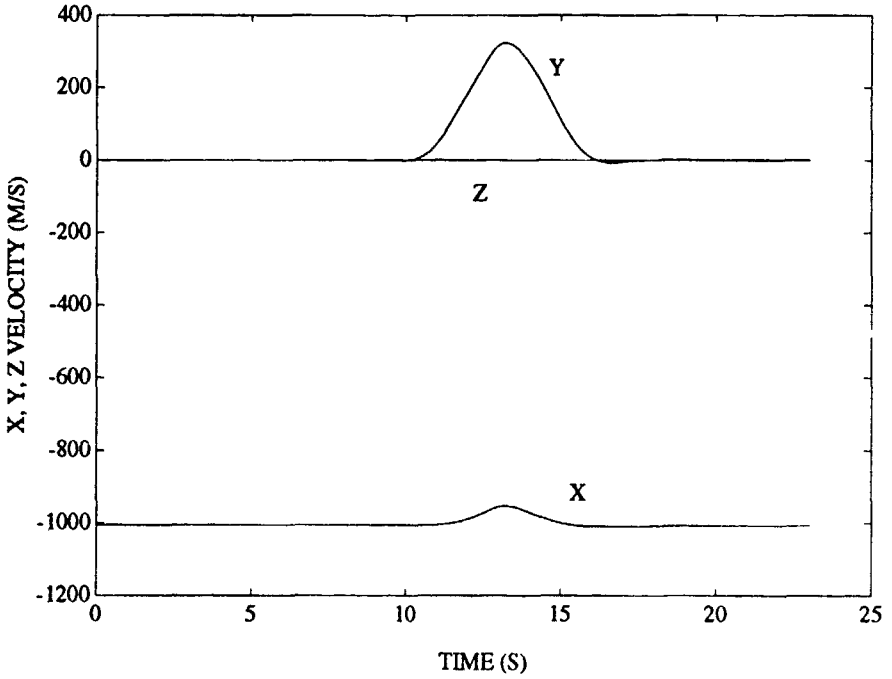

FIGURE A-10. TRUE VELOCITY FOR S-TURN TARGET

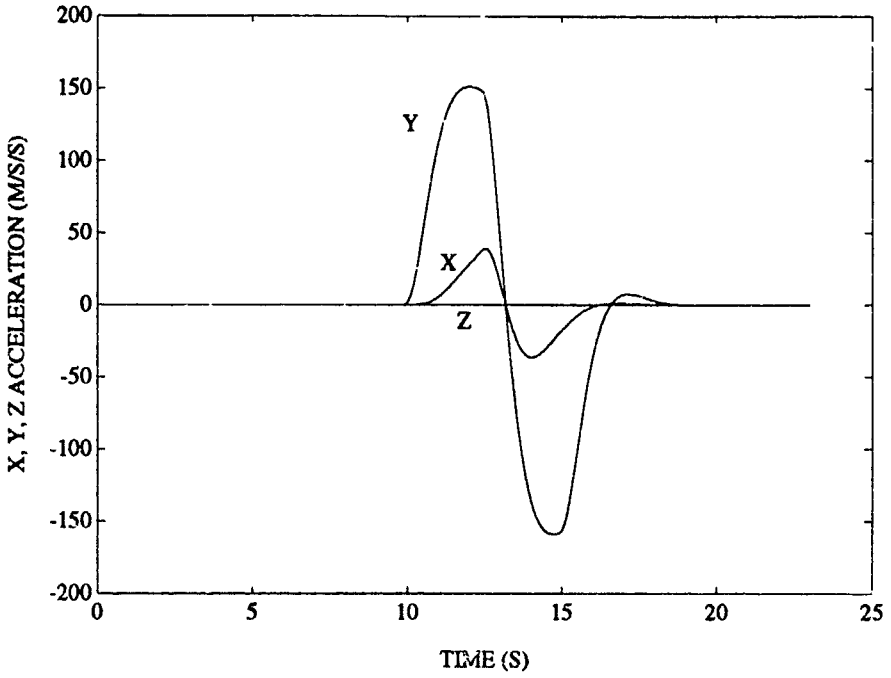

FIGURE A-11. TRUE ACCELERATION FOR S-TURN TARGET

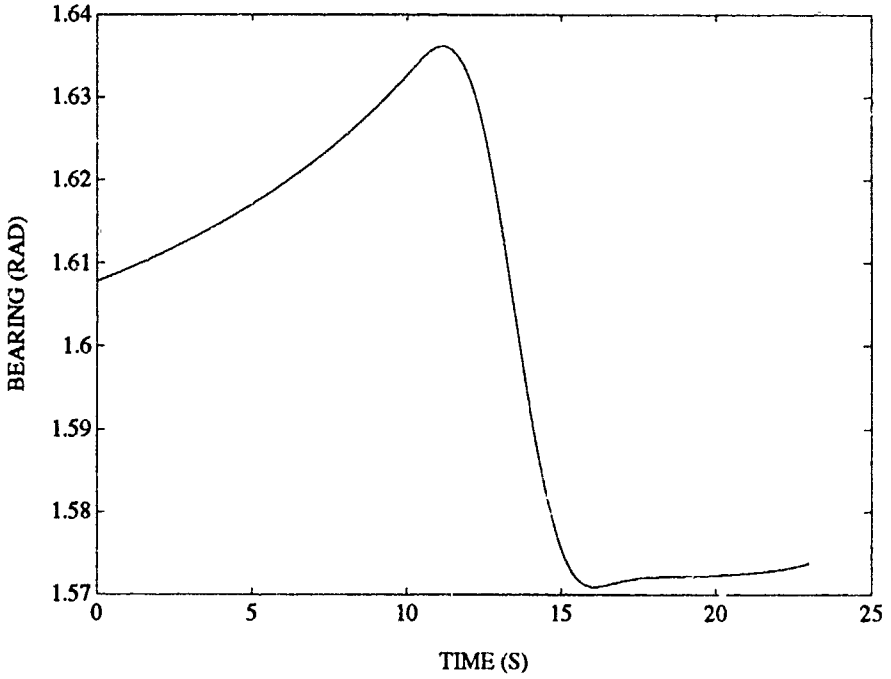

FIGURE A-12. TRUE BEARING FOR S-TURN TARGET

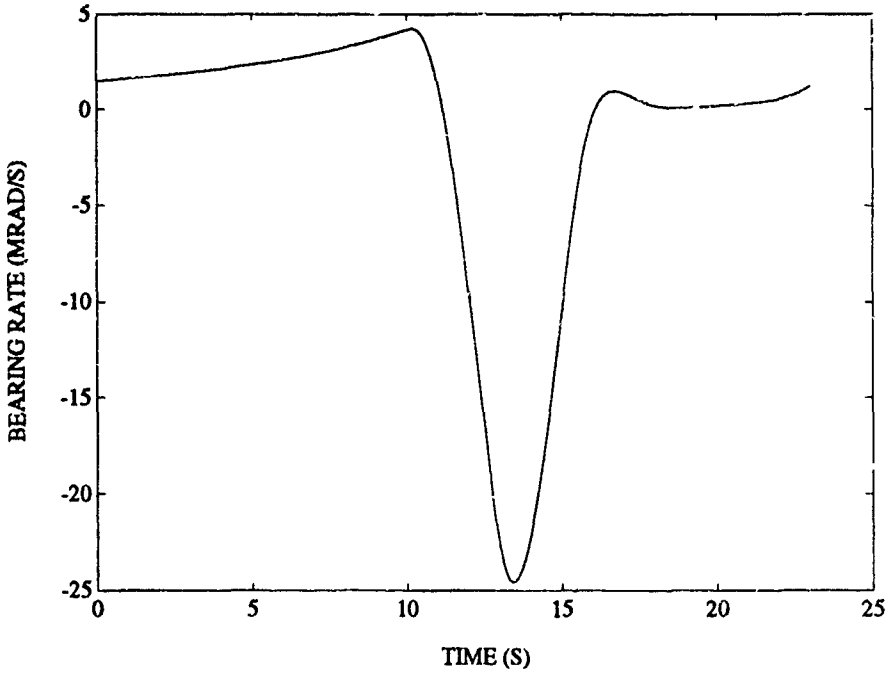

FIGURE A-13. TRUE BEARING RATE FOR S-TURN TARGET

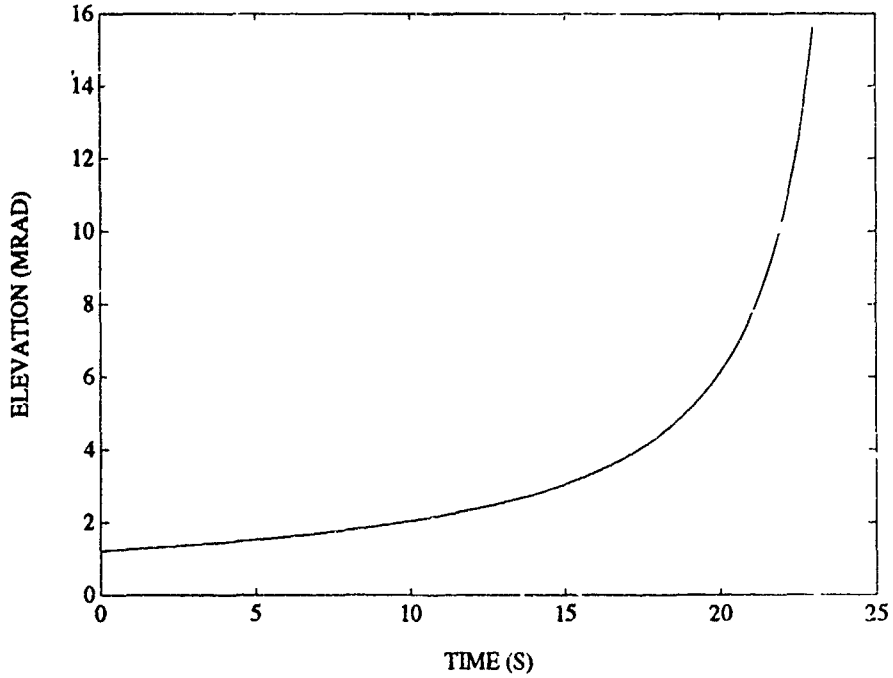

FIGURE A-14. TRUE ELEVATION FOR S-TURN TARGET

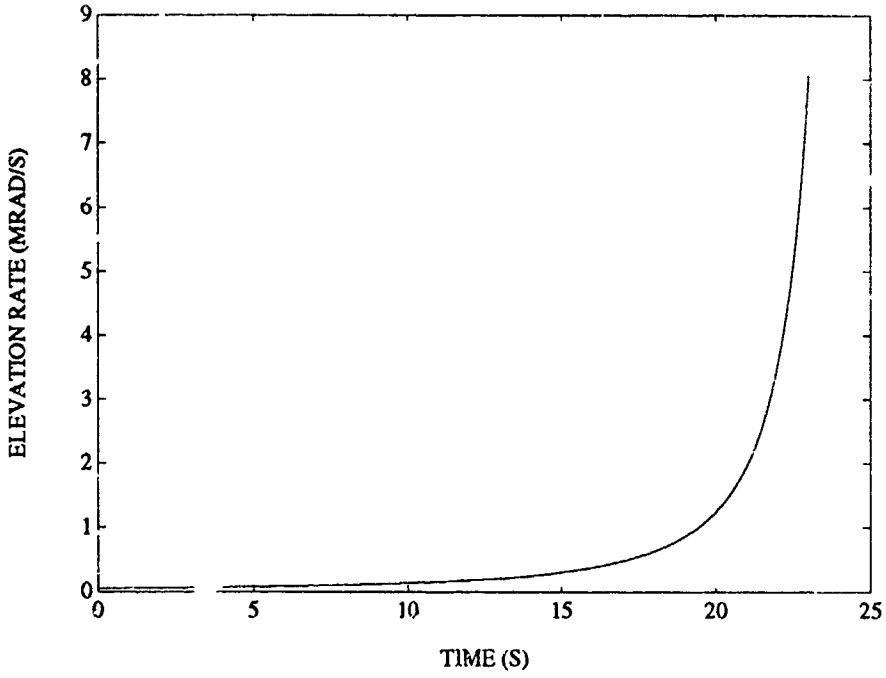

FIGURE A-15. TRUE ELEVATION RATE FOR S-TURN TARGET

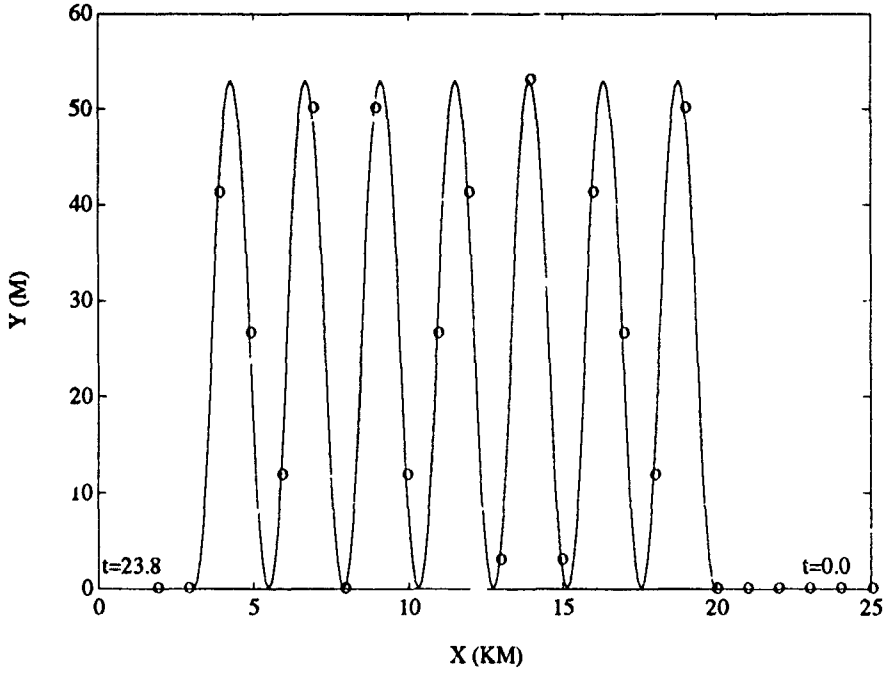

FIGURE A-16. X-Y PLANE FOR JINKING TARGET

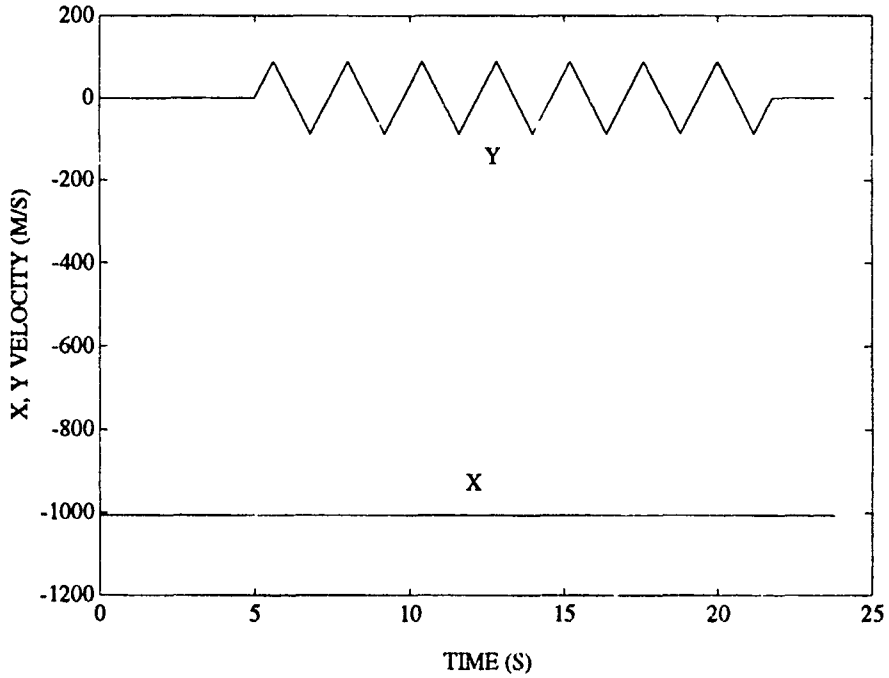

FIGURE A-17. TRUE VELOCITY FOR JINKING TARGET

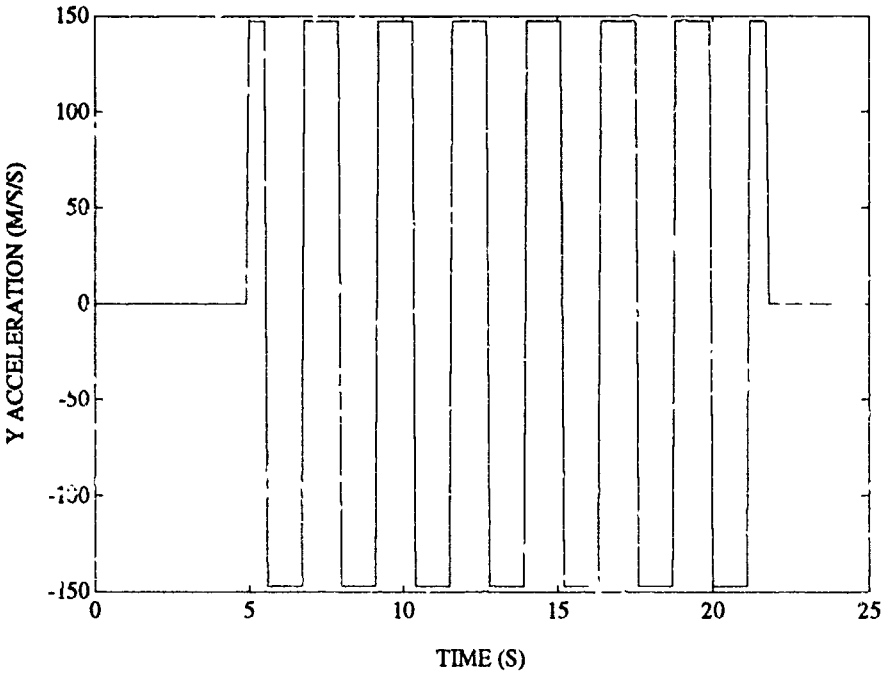

FIGURE A-18. TRUE ACCELERATION FOR JINKING TARGET

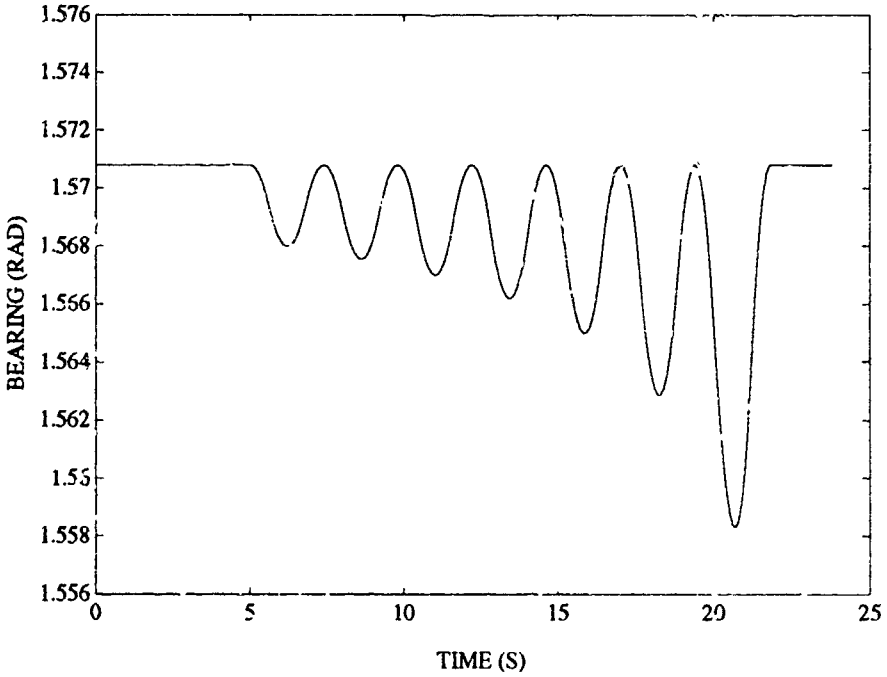

FIGURE A-19. TRUE BEARING FOR JINKING TARGET

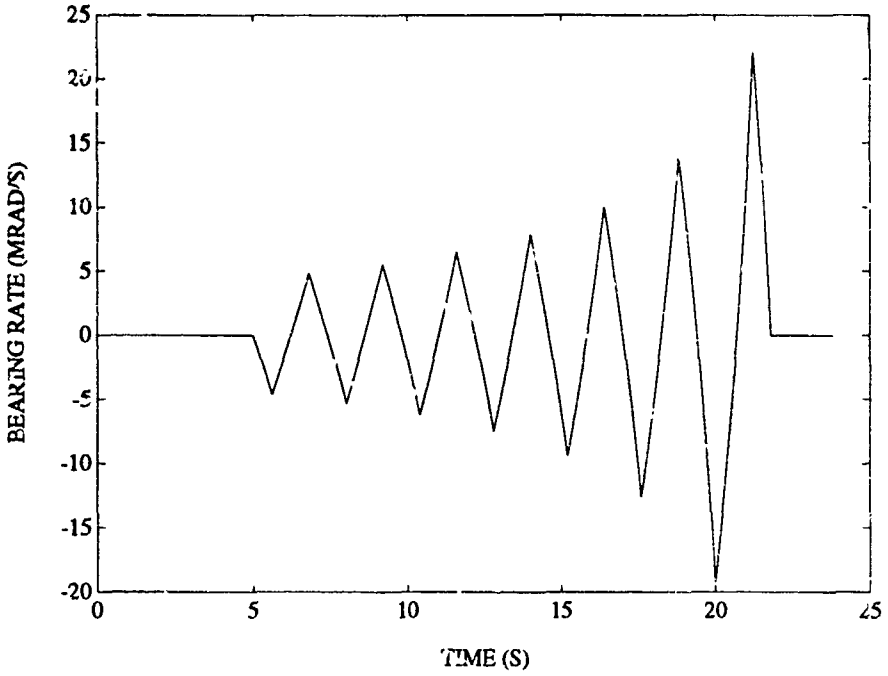

FIGURE A-20. TRUE BEARING RATE FOR JINKING TARGET

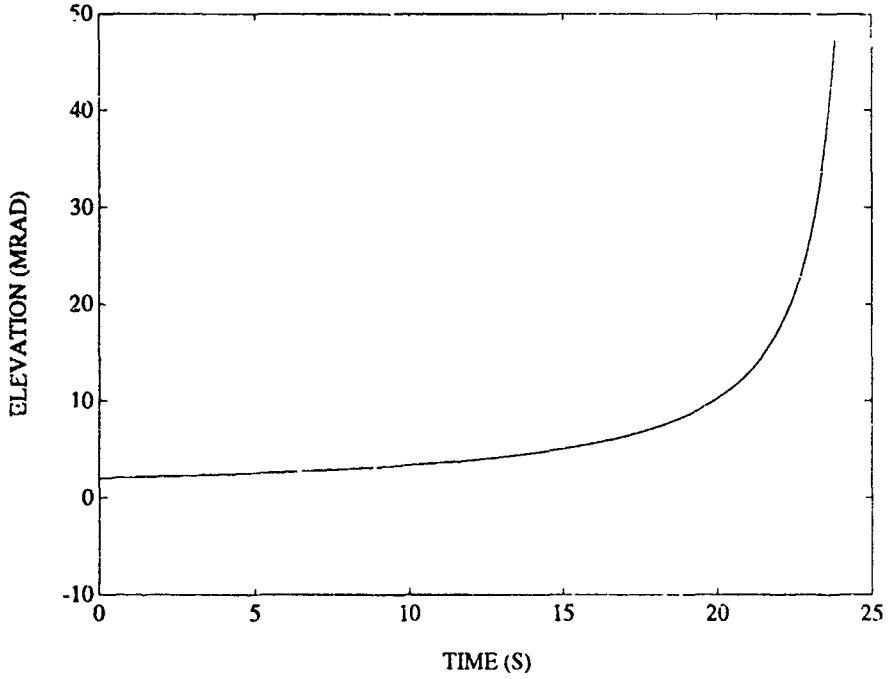

FIGURE A-21. TRUE ELEVATION FOR JINKING TARGET

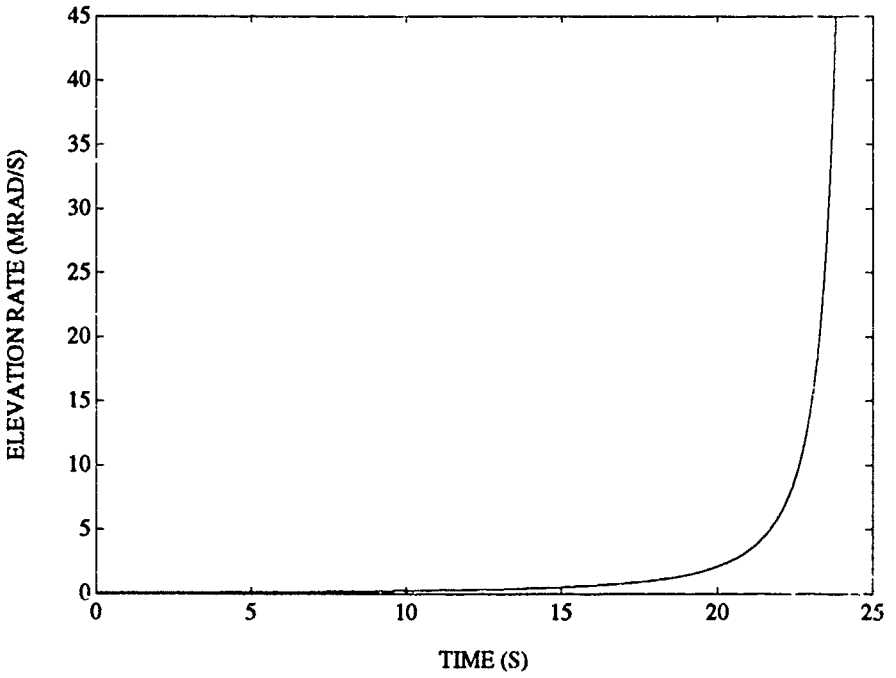

FIGURE A-22. TRUE ELEVATION RATE FOR JINKING TARGET

APPENDIX B
PLOTS OF PROCESS NOISE VARIANCE SELECTION

This appendix presents the results of the example of the process noise variance selection procedure. This example is for the 3 state filter on the crossing target. The consistency tests are used to determine the best value of the process noise variance for the particular trajectory.

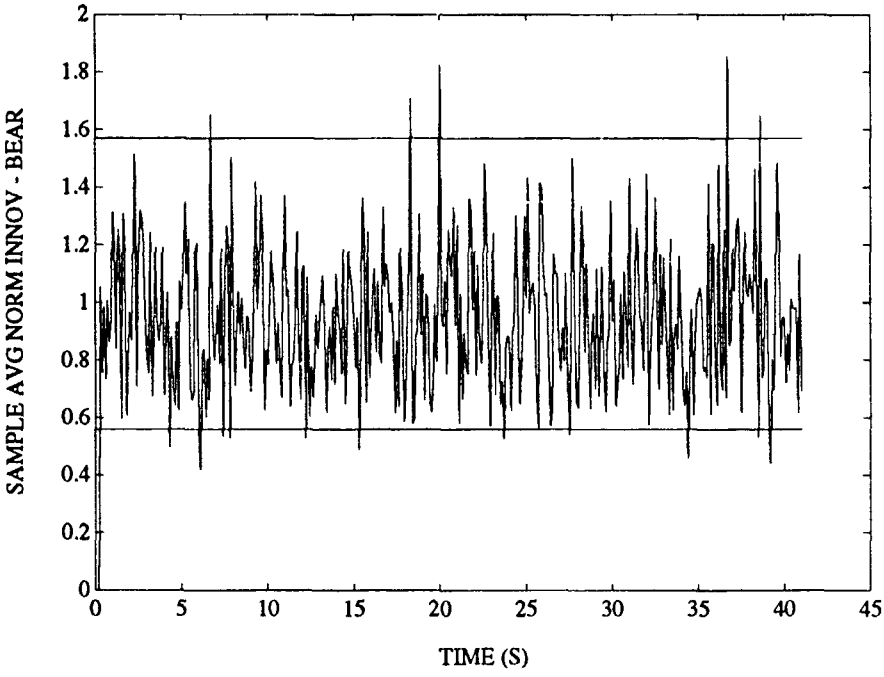

FIGURE B-1. CHI-SQUARE TEST OF BEARING INNOVATIONS FOR 3 STATE FILTER ON CROSSING TARGET WITH $q=10^{-6}$

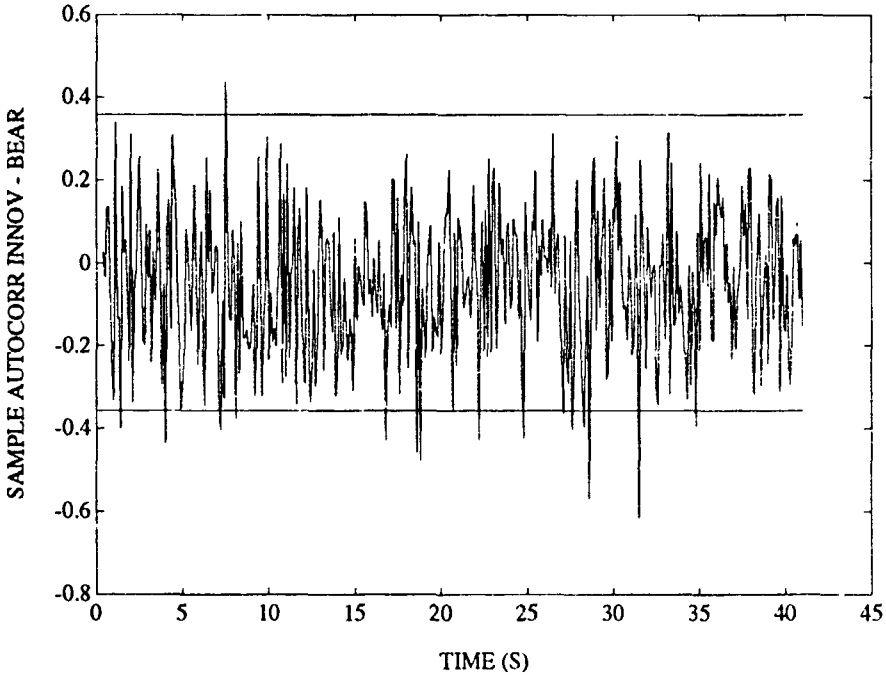

FIGURE B-2. WHITENESS TEST OF BEARING INNOVATIONS FOR 3 STATE FILTER ON CROSSING TARGET WITH $q=10^{-6}$

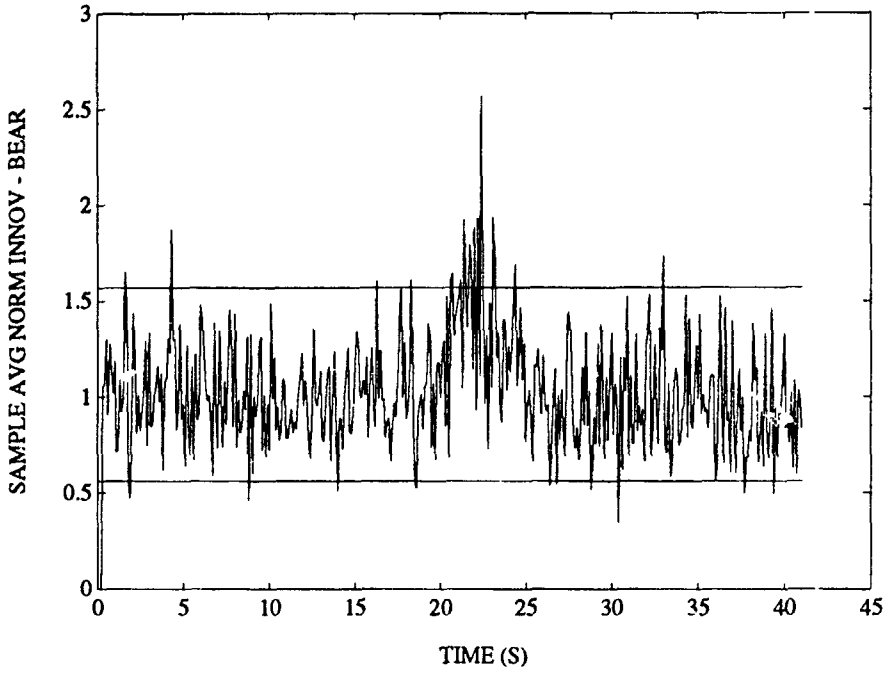

FIGURE B-3. CHI-SQUARE TEST OF BEARING INNOVATIONS FOR 3 STATE FILTER ON CROSSING TARGET WITH $q=10^{-7}$

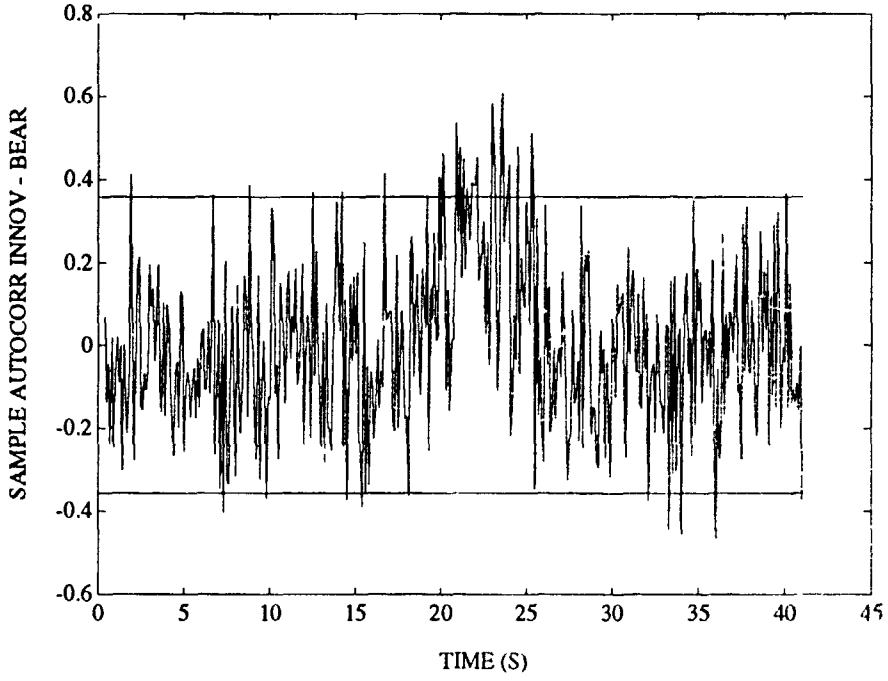

FIGURE B-4. WHITENESS TEST OF BEARING INNOVATIONS FOR 3 STATE FILTER ON CROSSING TARGET WITH $q=10^{-7}$

APPENDIX C
PLOTS OF 2 STATE FILTER RESULTS

This appendix presents the results of simulations performed for the 2 state filters. The results are presented in the following order: radial target, crossing target, S-turn target, and jinking target.

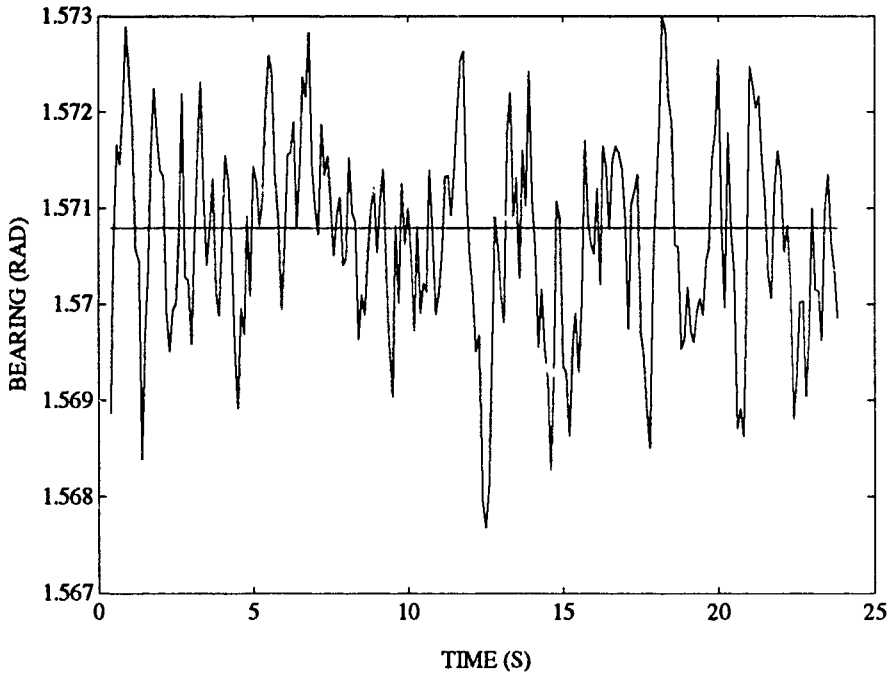

FIGURE C-1. SAMPLE BEARING ESTIMATE FOR 2 STATE FILTER ON RADIAL TARGET

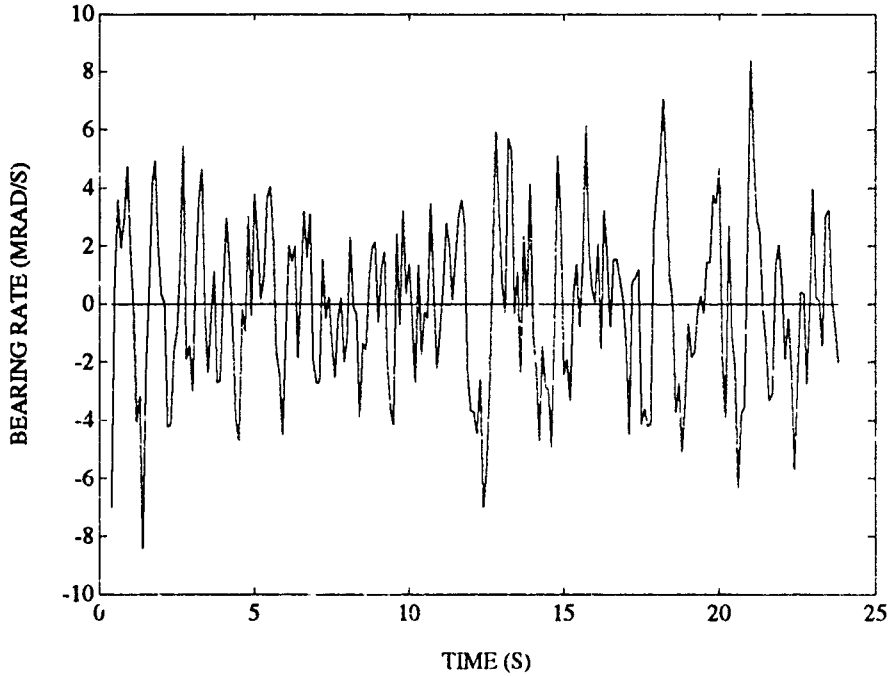

FIGURE C-2. SAMPLE BEARING RATE ESTIMATE FOR 2 STATE FILTER ON RADIAL TARGET

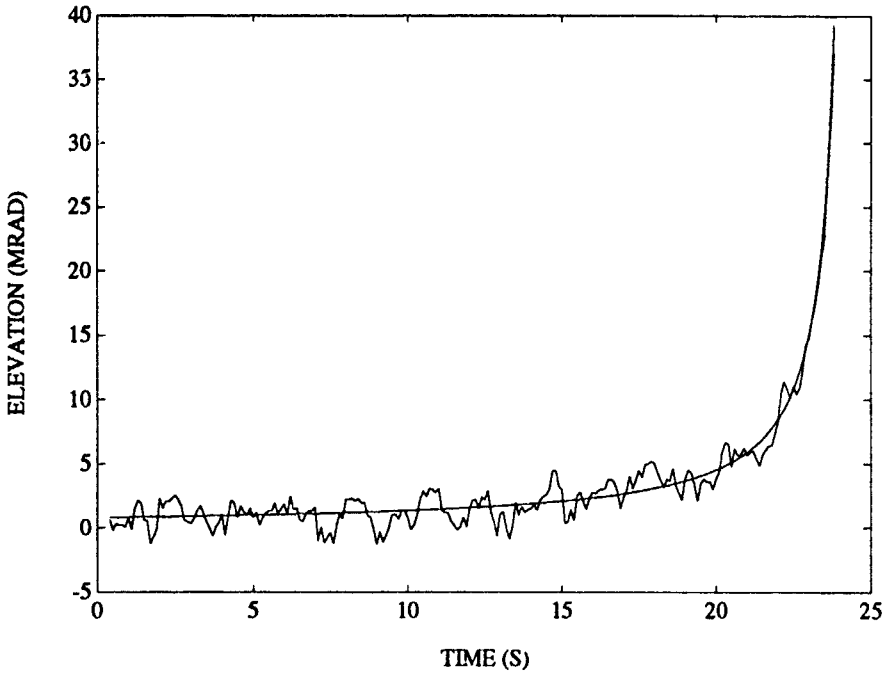

FIGURE C-3. SAMPLE ELEVATION ESTIMATE FOR 2 STATE FILTER ON RADIAL TARGET

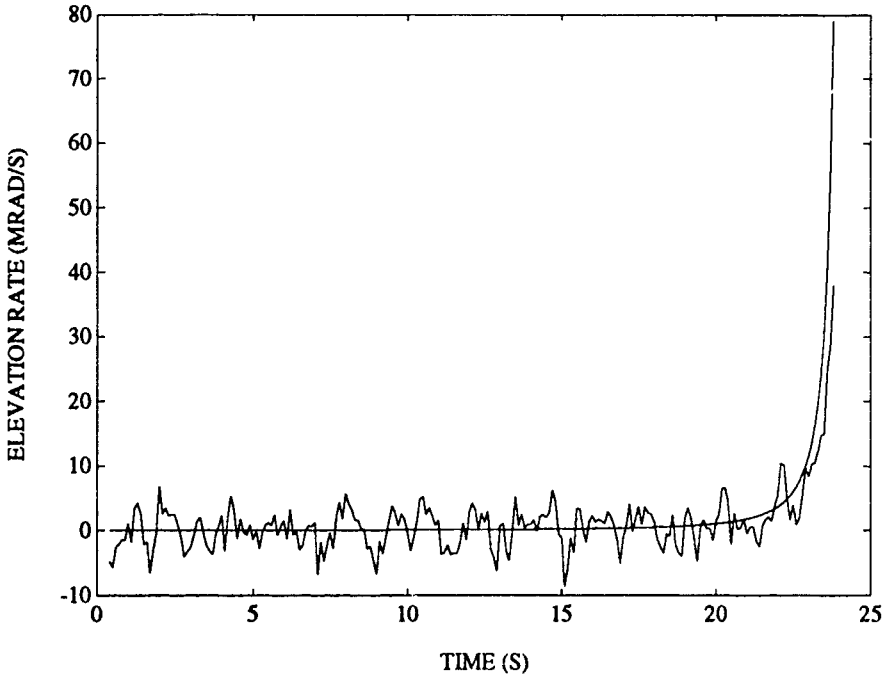

FIGURE C-4. SAMPLE ELEVATION RATE ESTIMATE FOR 2 STATE FILTER ON RADIAL TARGET

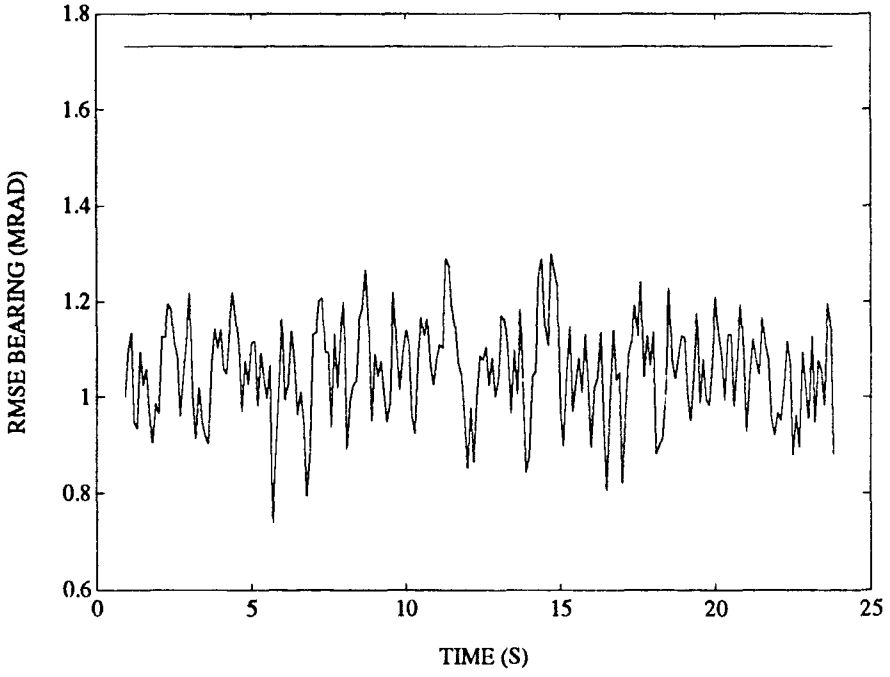

FIGURE C-5. RMS BEARING ERROR FOR 2 STATE FILTER ON RADIAL TARGET

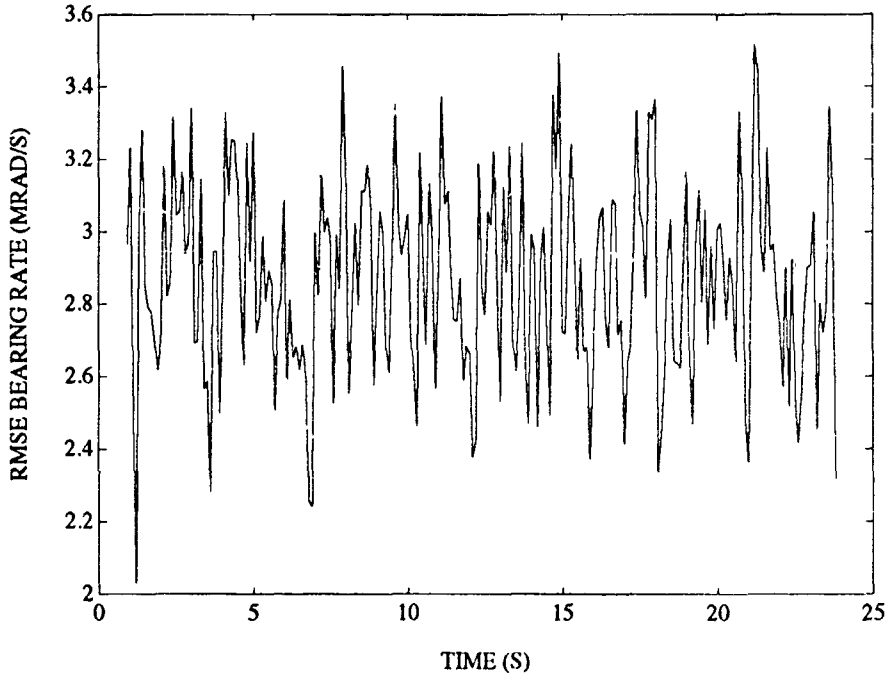

FIGURE C-6. RMS BEARING RATE ERROR FOR 2 STATE FILTER ON RADIAL TARGET

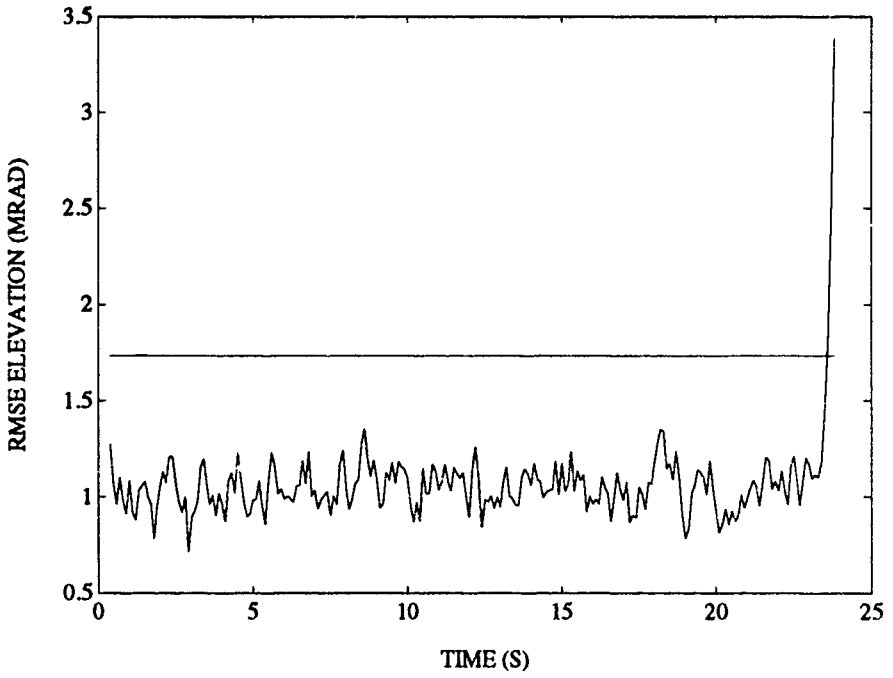

FIGURE C-7. RMS ELEVATION ERROR FOR 2 STATE FILTER ON RADIAL TARGET

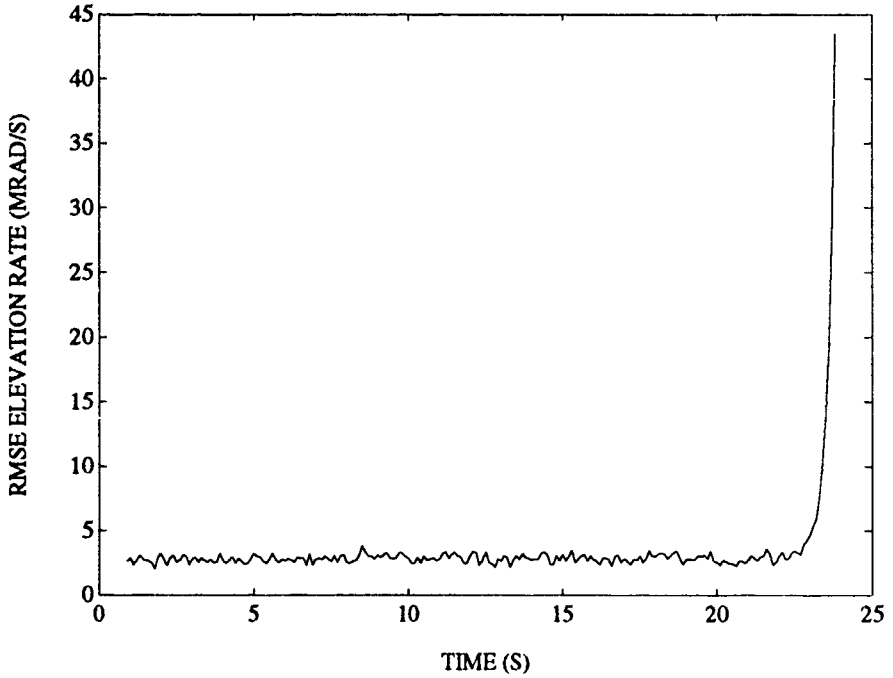

FIGURE C-8. RMS ELEVATION RATE ERROR FOR 2 STATE FILTER ON RADIAL TARGET

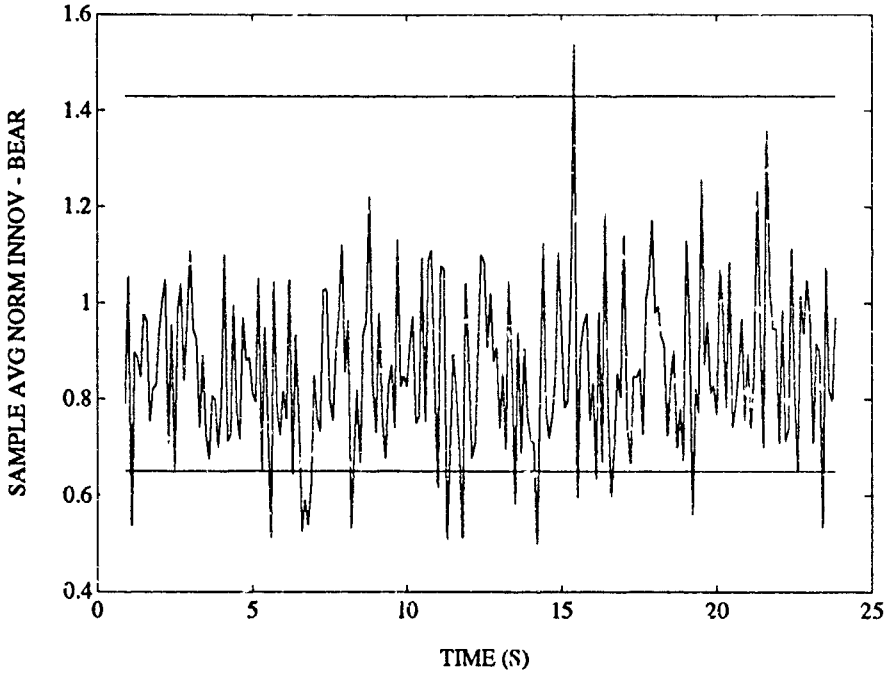

FIGURE C-9. CHI-SQUARE TEST OF BEARING INNOVATIONS FOR 2 STATE FILTER ON RADIAL TARGET

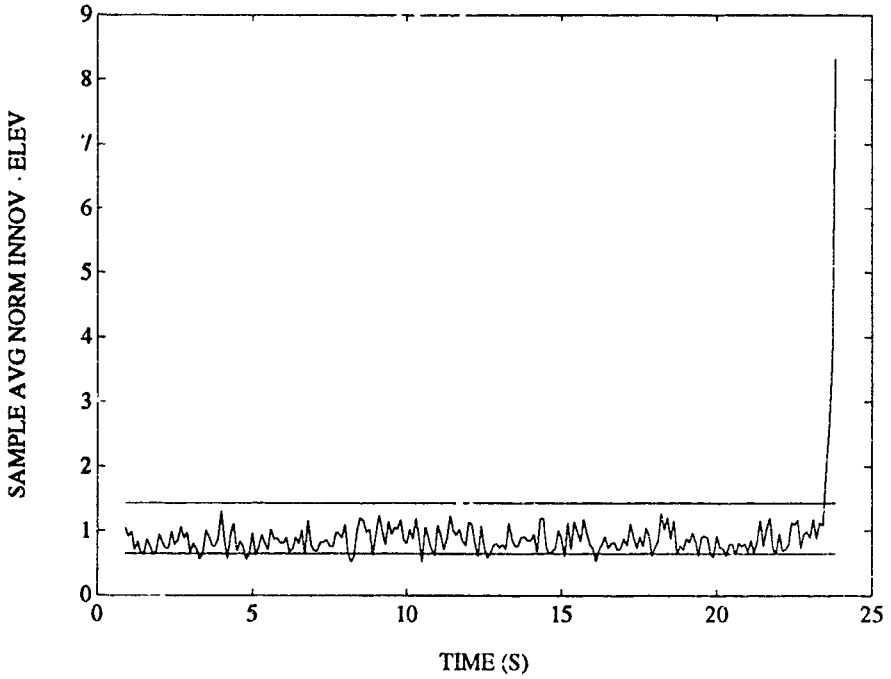

FIGURE C-10. CHI-SQUARE TEST OF ELEVATION INNOVATIONS FOR 2 STATE FILTER ON RADIAL TARGET

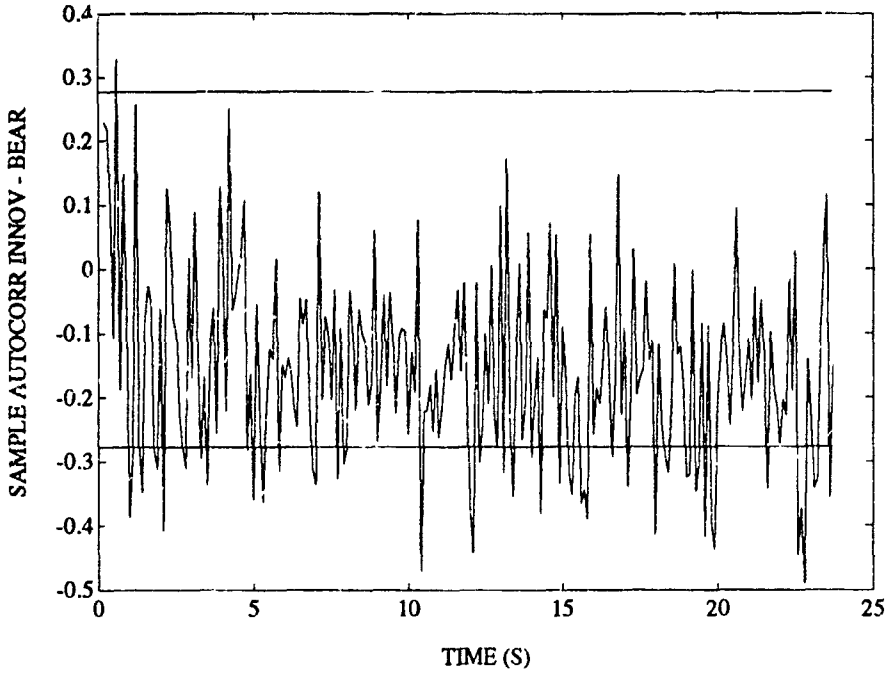

FIGURE C-11. WHITENESS TEST OF BEARING INNOVATIONS FOR 2 STATE FILTER ON RADIAL TARGET

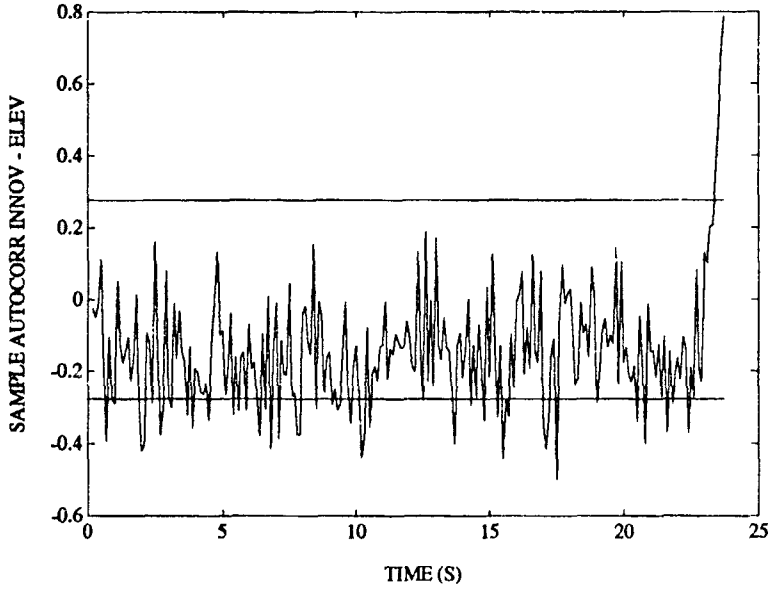

FIGURE C-12. WHITENESS TEST OF ELEVATION INNOVATIONS FOR 2 STATE FILTER ON RADIAL TARGET

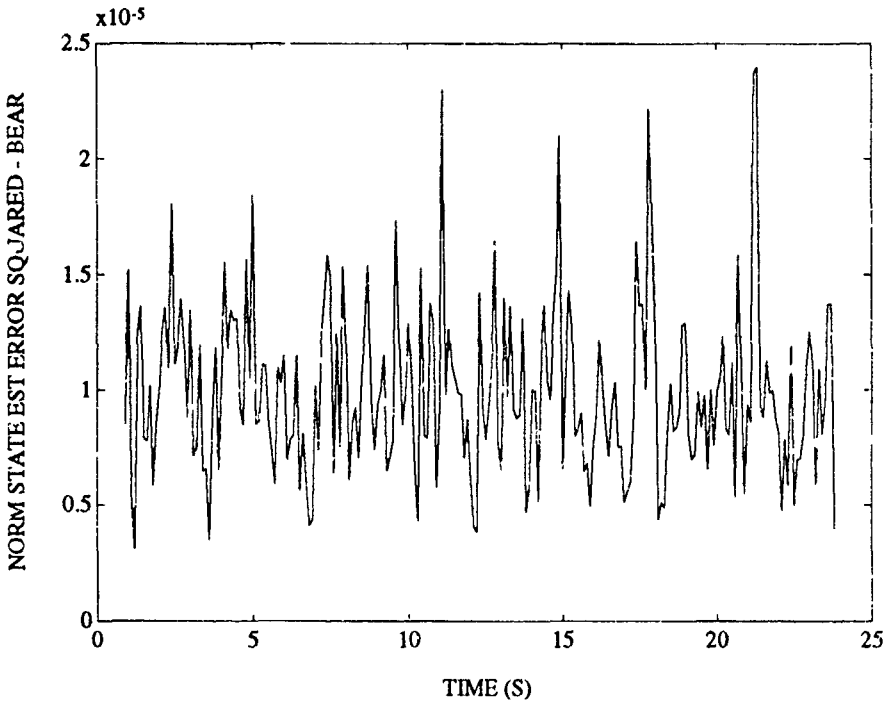

FIGURE C-13. CHI-SQURE TEST OF BEARING ESTIMATION ERROR FOR 2 STATE FILTER ON RADIAL TARGET

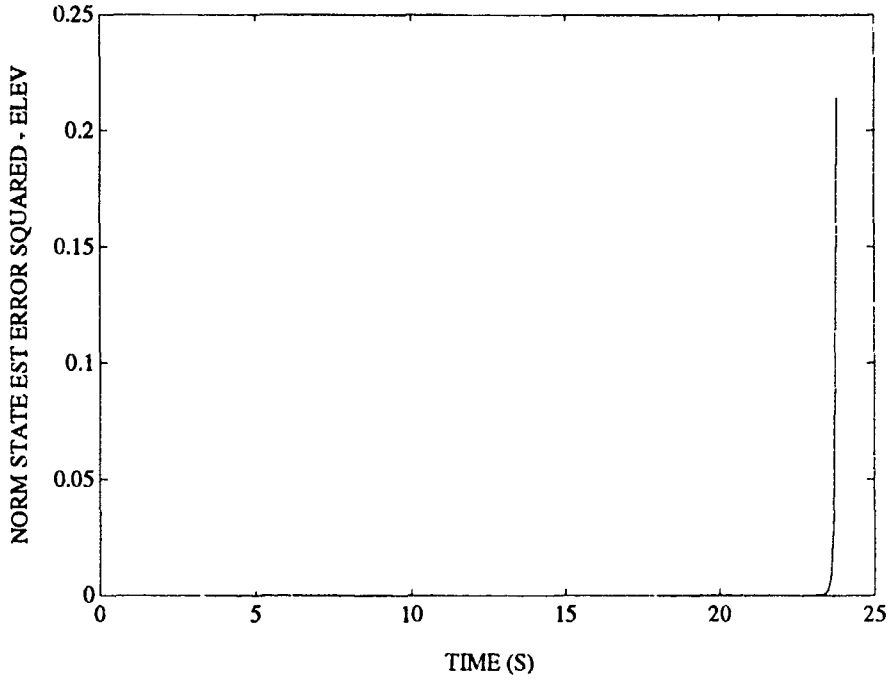

FIGURE C-14. CHI-SQUARE TEST OF ELEVATION ESTIMATION ERROR FOR 2 STATE FILTER ON RADIAL TARGET

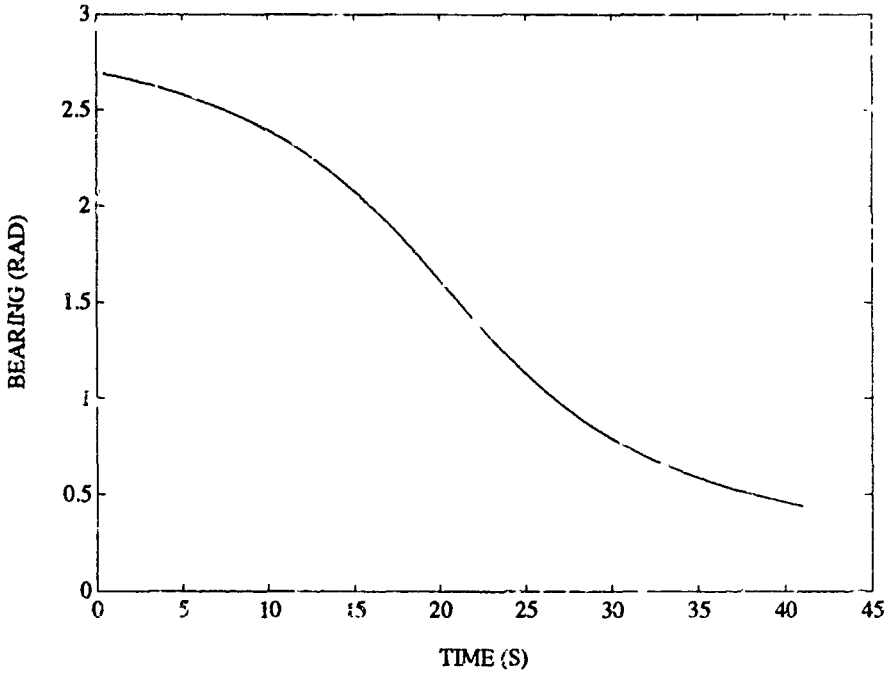

FIGURE C-15. SAMPLE BEARING ESTIMATE FOR 2 STATE FILTER ON CROSSING TARGET

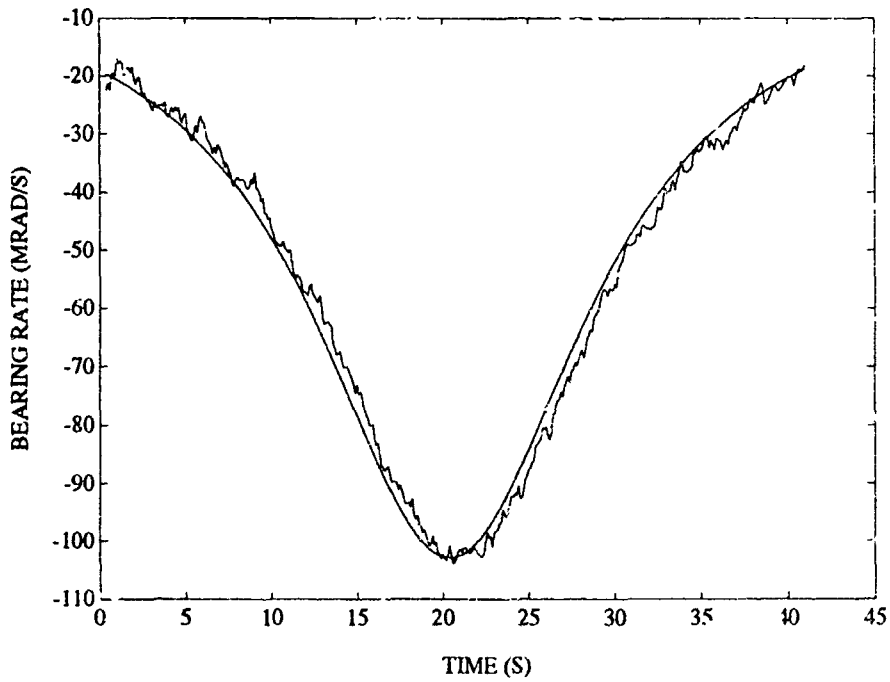

FIGURE C-16. SAMPLE BEARING RATE ESTIMATE FOR 2 STATE FILTER ON CROSSING TARGET

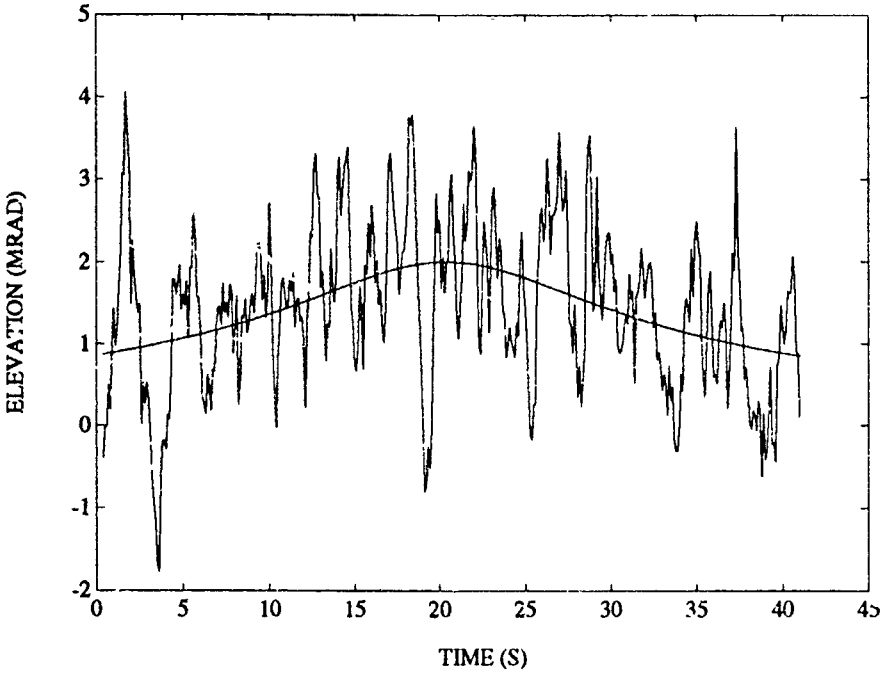

FIGURE C-17. SAMPLE ELEVATION ESTIMATE FOR 2 STATE FILTER ON CROSSING TARGET

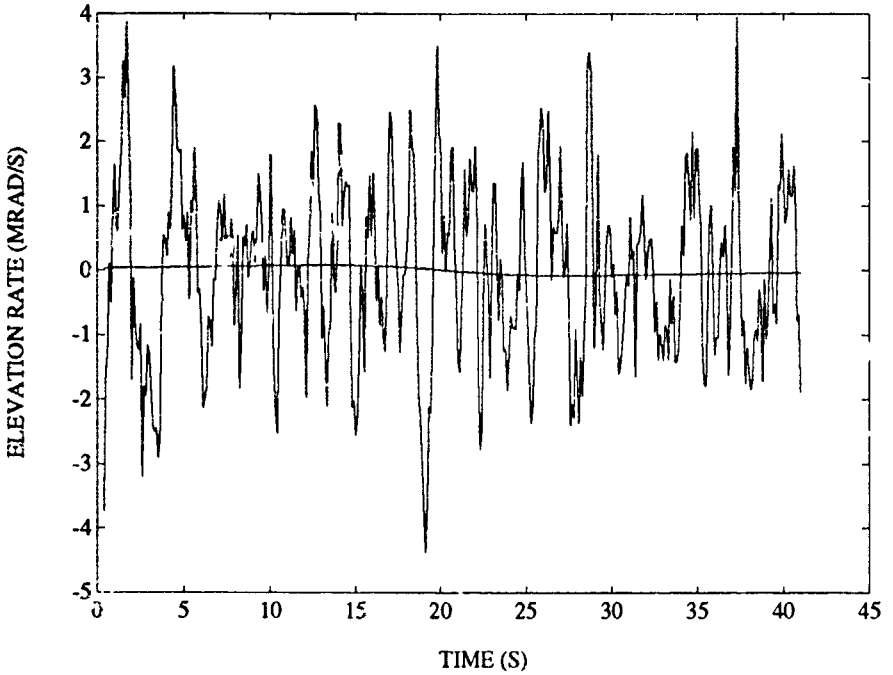

FIGURE C-18. SAMPLE ELEVATION RATE ESTIMATE FOR 2 STATE FILTER ON CROSSING TARGET

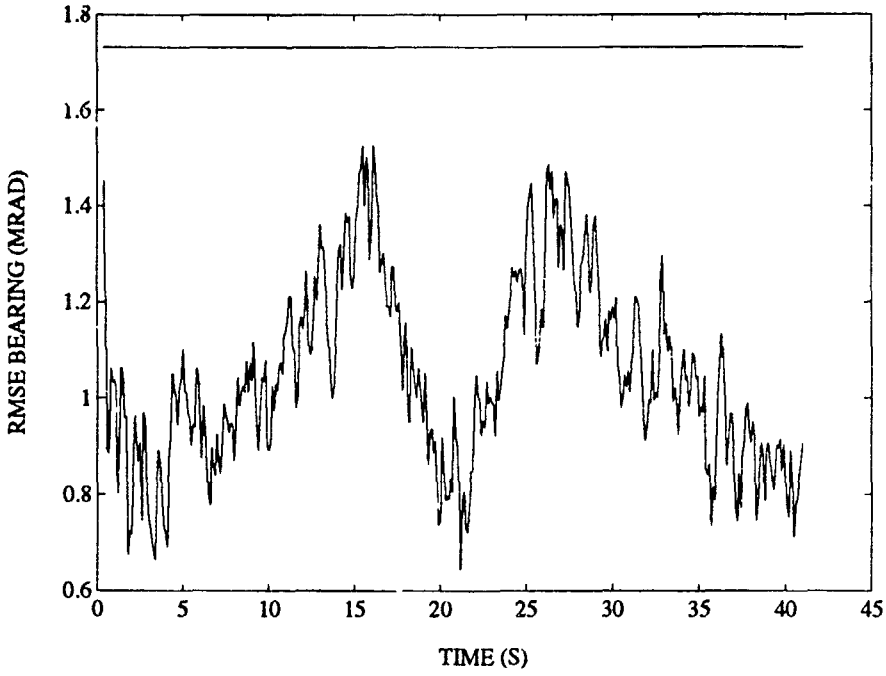

FIGURE C-19. RMS BEARING ERROR FOR 2 STATE FILTER ON CROSSING TARGET

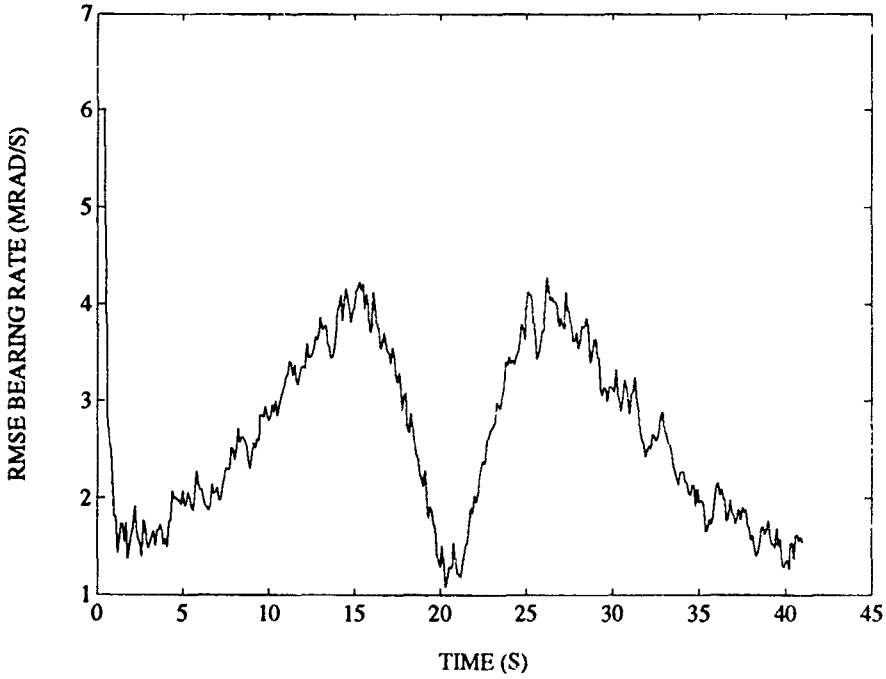

FIGURE C-20. RMS BEARING RATE ERROR FOR 2 STATE FILTER ON CROSSING TARGET

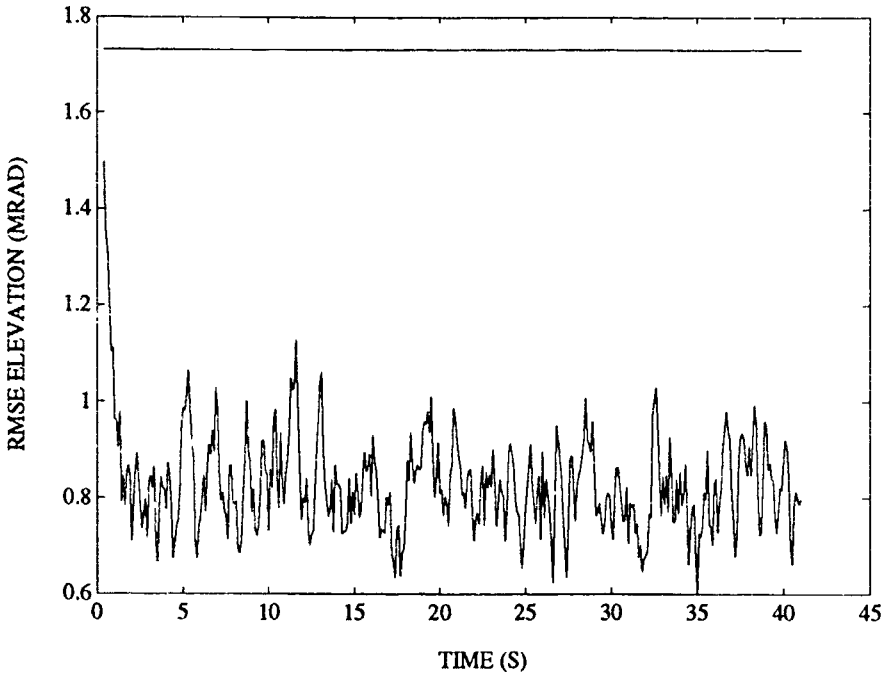

FIGURE C-21. RMS ELEVATION ERROR FOR 2 STATE FILTER ON CROSSING TARGET

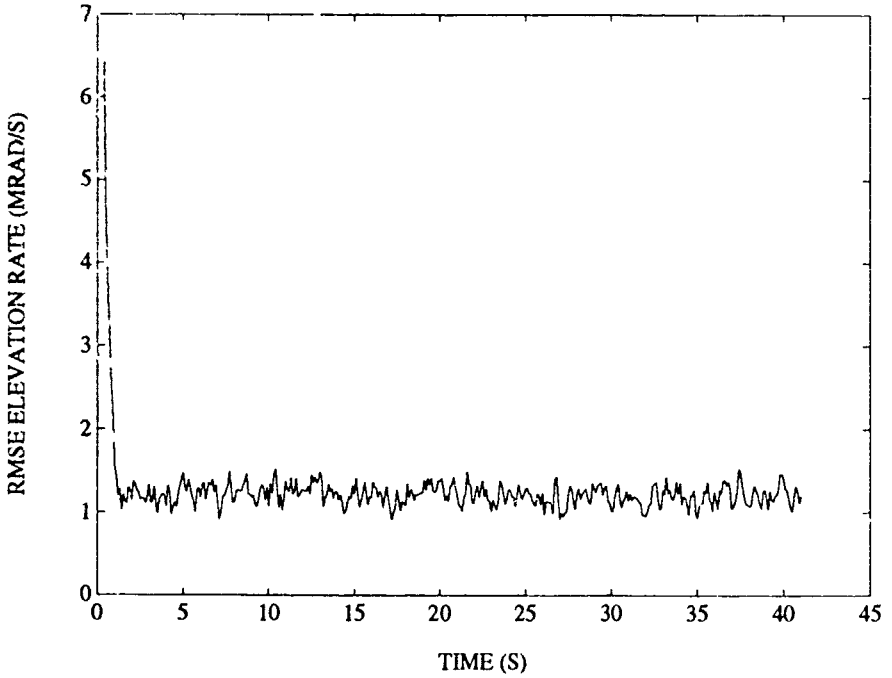

FIGURE C-22. RMS ELEVATION RATE ERROR FOR 2 STATE FILTER ON CROSSING TARGET

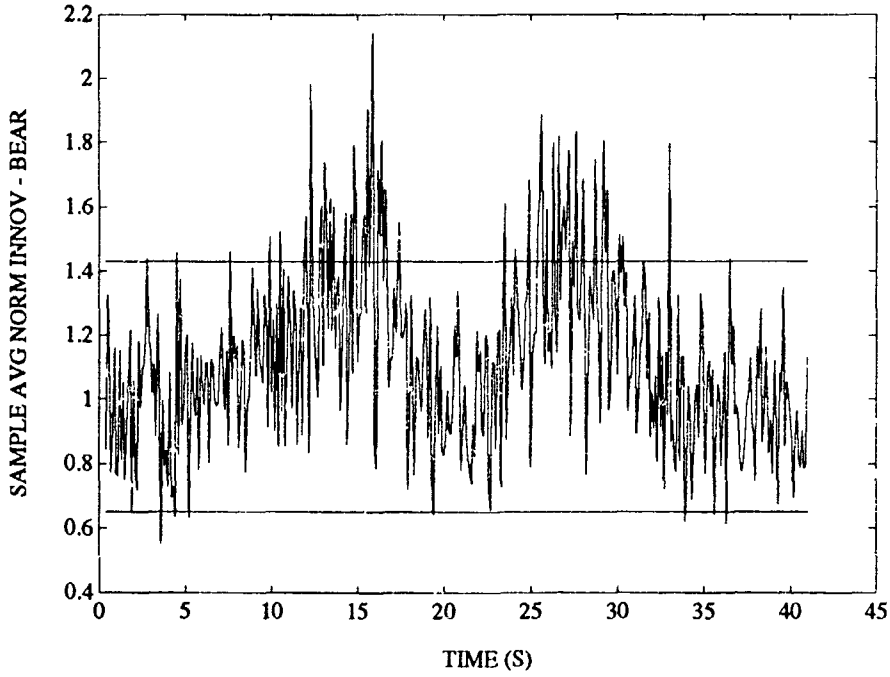

FIGURE C-23. CHI-SQUARE TEST OF BEARING INNOVATIONS FOR 2 STATE FILTER ON CROSSING TARGET

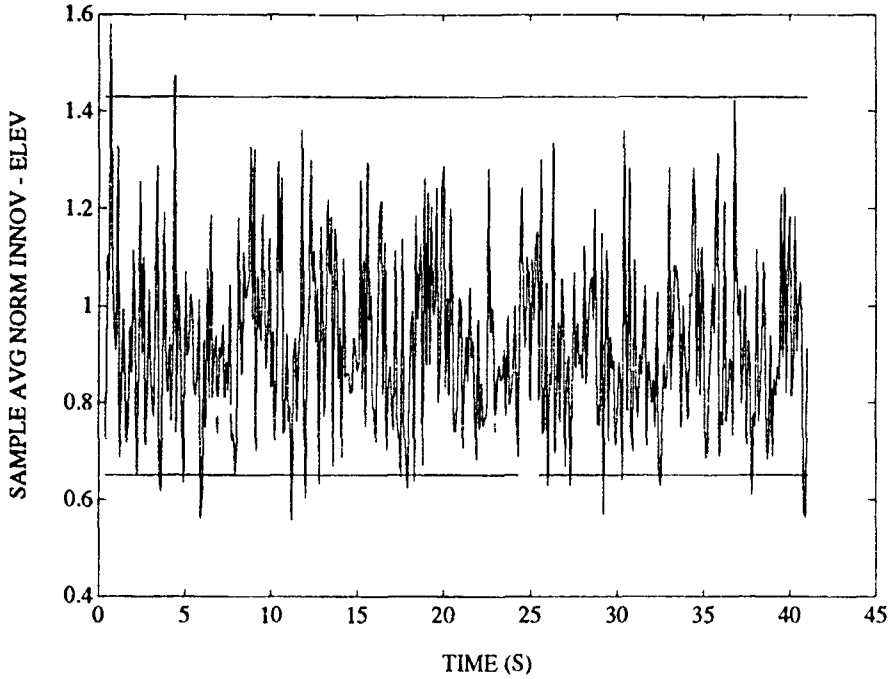

FIGURE C-24. CHI-SQUARE TEST OF ELEVATION INNOVATIONS FOR 2 STATE FILTER ON CROSSING TARGET

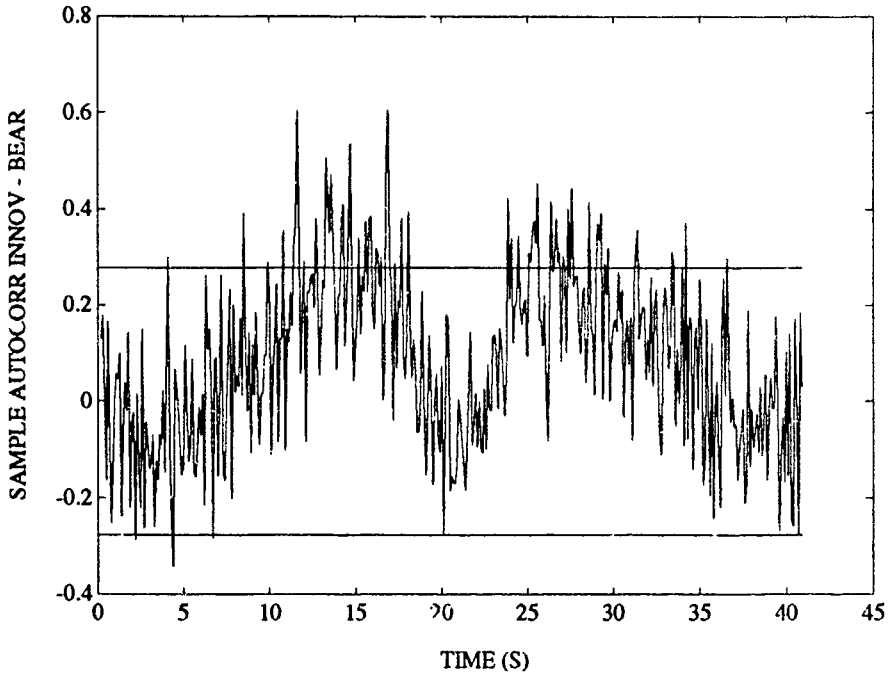

FIGURE C-25. WHITENESS TEST OF BEARING INNOVATIONS FOR 2 STATE FILTER ON CROSSING TARGET

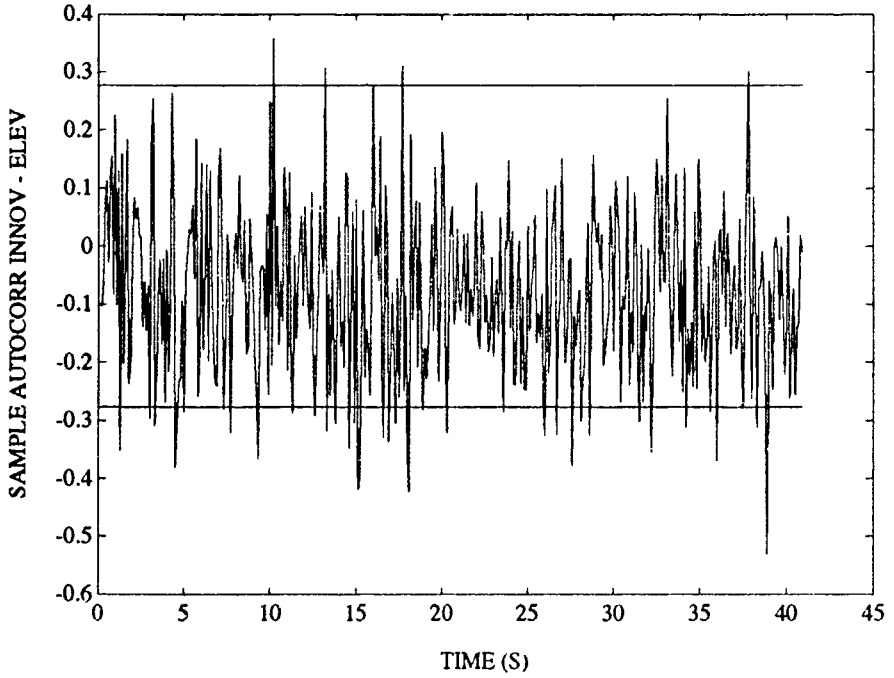

FIGURE C-26. WHITENESS TEST OF ELEVATION INNOVATIONS FOR 2 STATE FILTER ON CROSSING TARGET

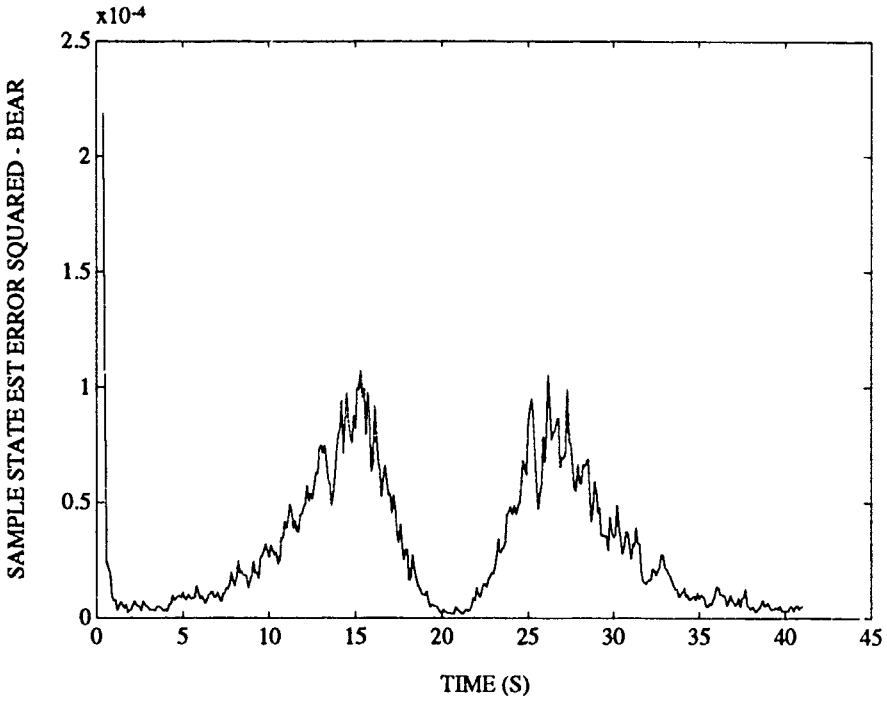

FIGURE C-27. CHI-SQUARE TEST OF BEARING ESTIMATION ERROR FOR 2 STATE FILTER ON CROSSING TARGET

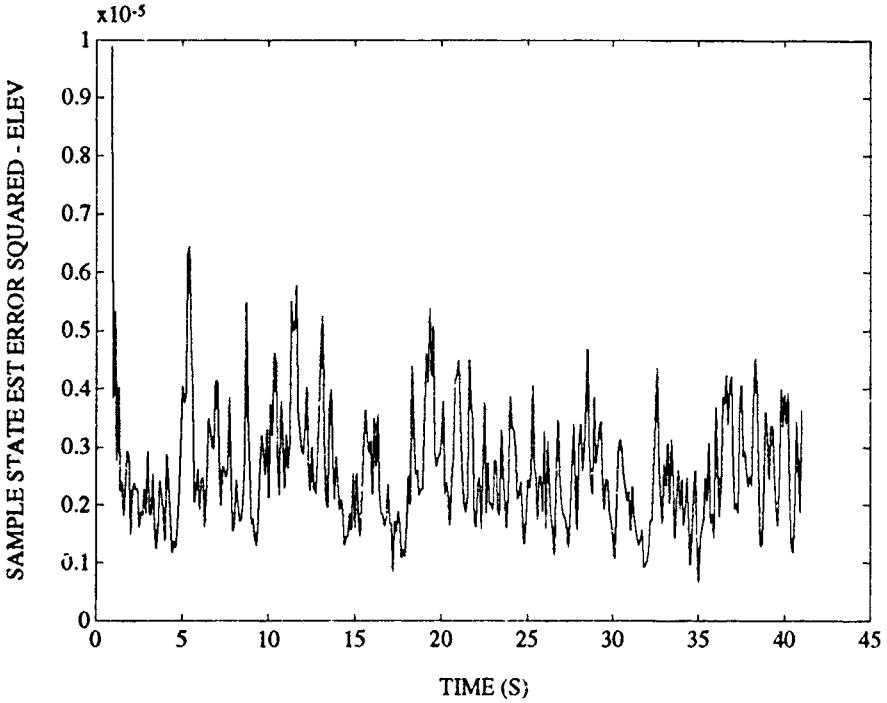

FIGURE C-28. CHI-SQUARE TEST OF ELEVATION ESTIMATION ERROR FOR 2 STATE FILTER ON CROSSING TARGET

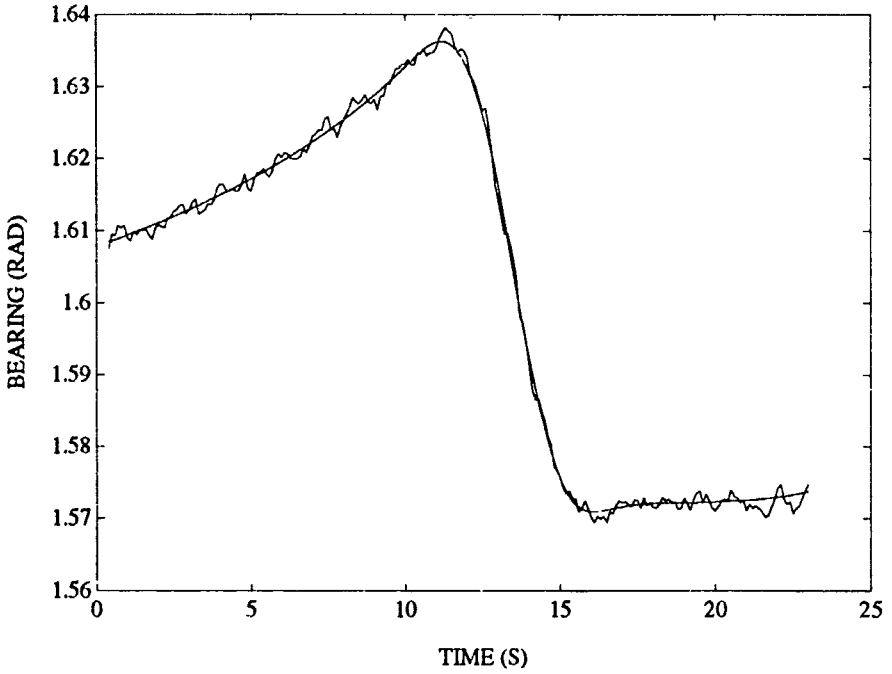

FIGURE C-29. SAMPLE BEARING ESTIMATE FOR 2 STATE FILTER ON S-TURN TARGET

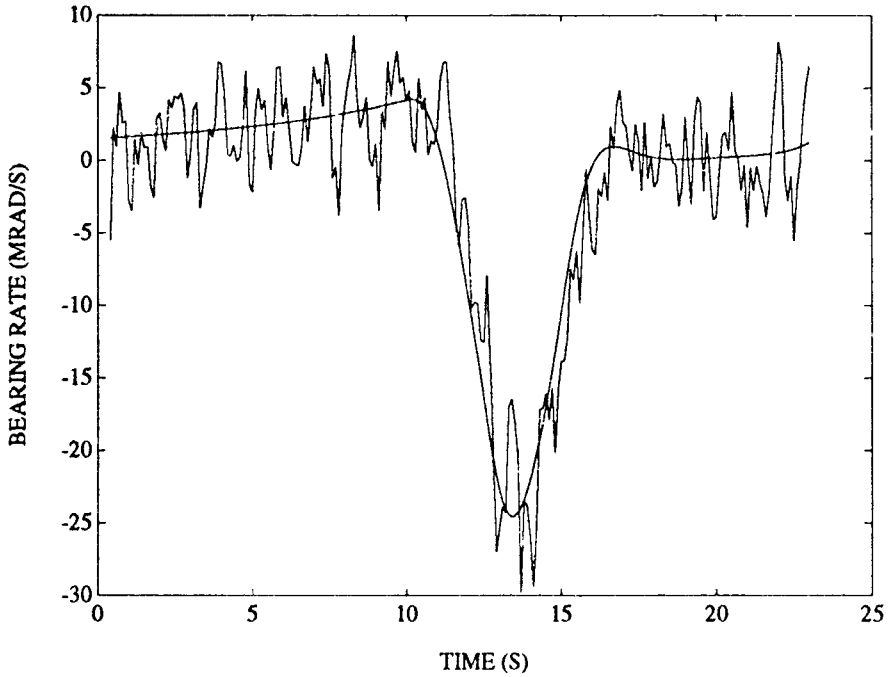

FIGURE C-30. SAMPLE BEARING RATE ESTIMATE FOR 2 STATE FILTER ON S-TURN TARGET

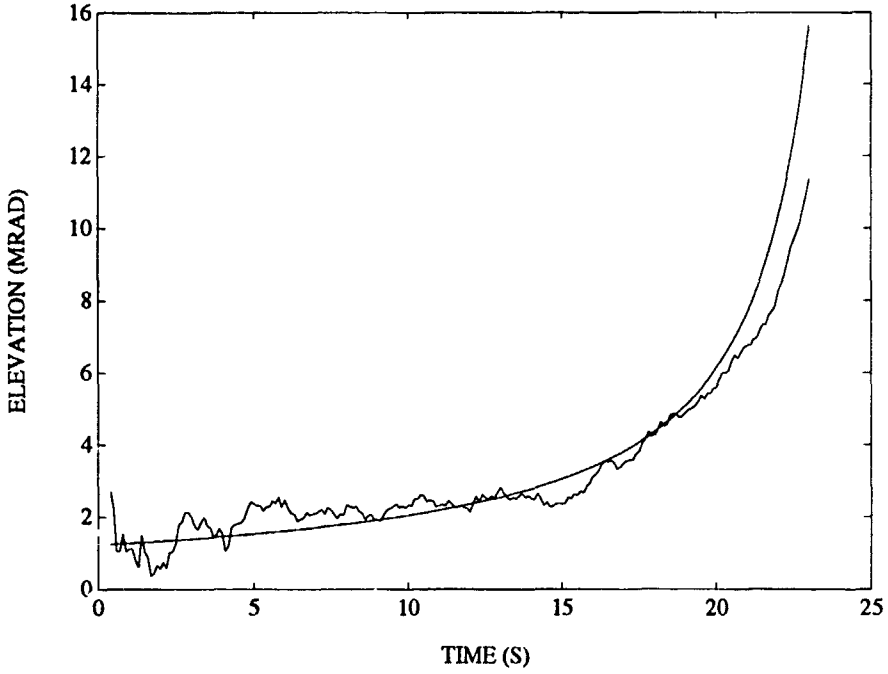

FIGURE C-31. SAMPLE ELEVATION ESTIMATE FOR 2 STATE FILTER ON S-TURN TARGET

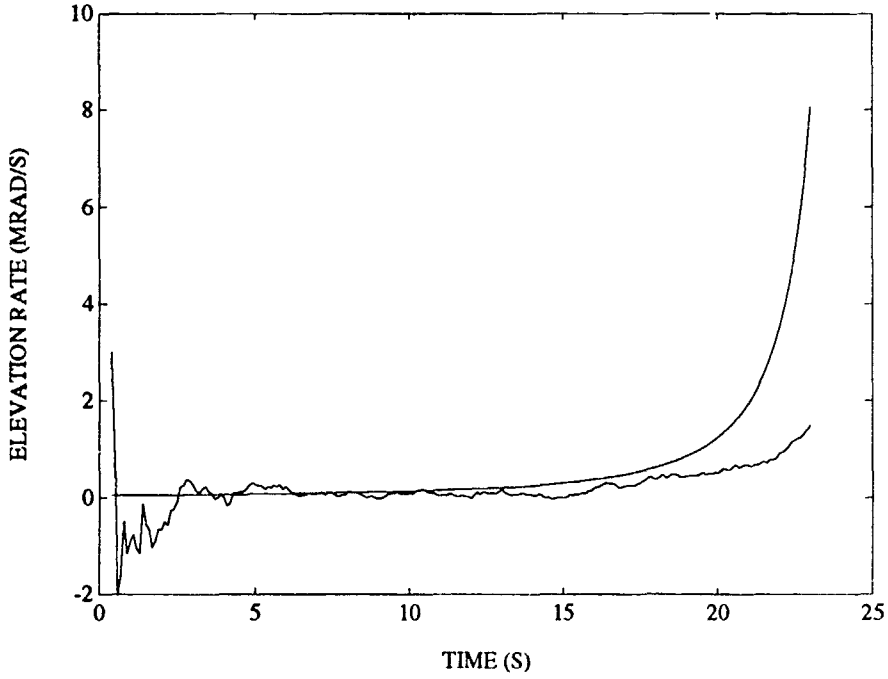

FIGURE C-32. SAMPLE ELEVATION RATE ESTIMATE FOR 2 STATE FILTER ON S-TURN TARGET

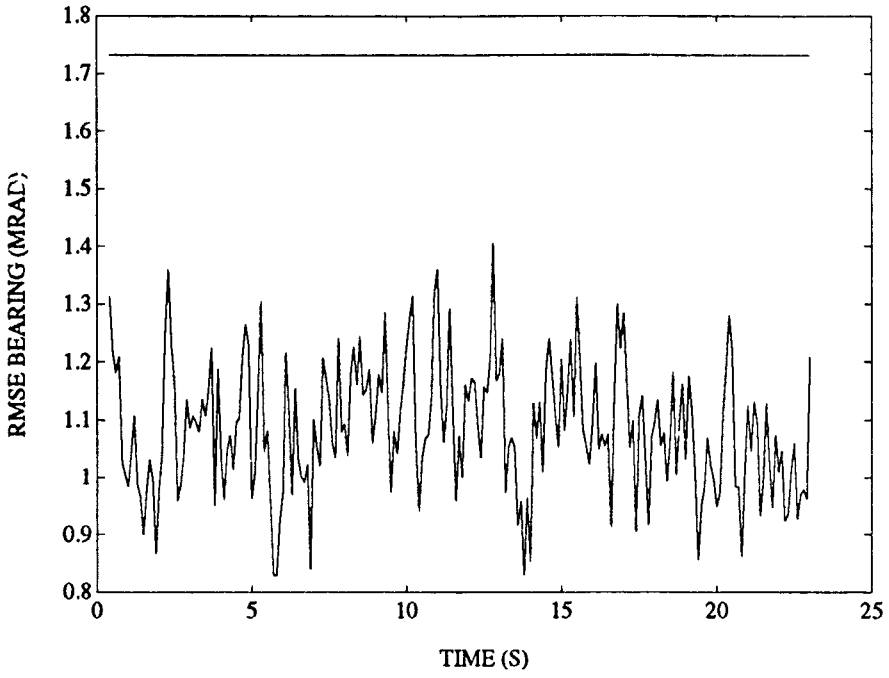

FIGURE C-33. RMS BEARING ERROR FOR 2 STATE FILTER ON S-TURN TARGET

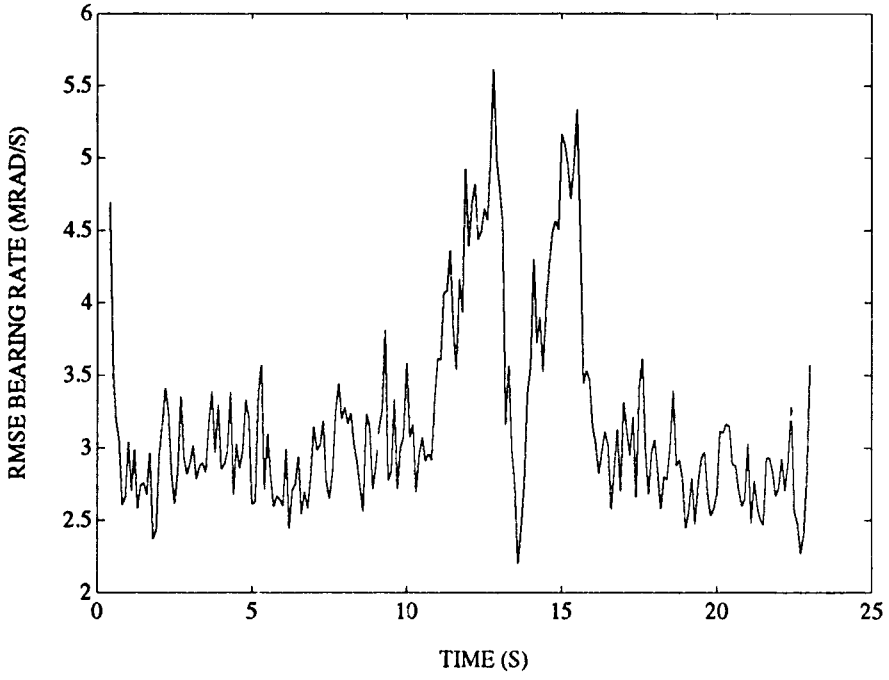

FIGURE C-34. RMS BEARING RATE ERROR FOR 2 STATE FILTER ON S-TURN TARGET

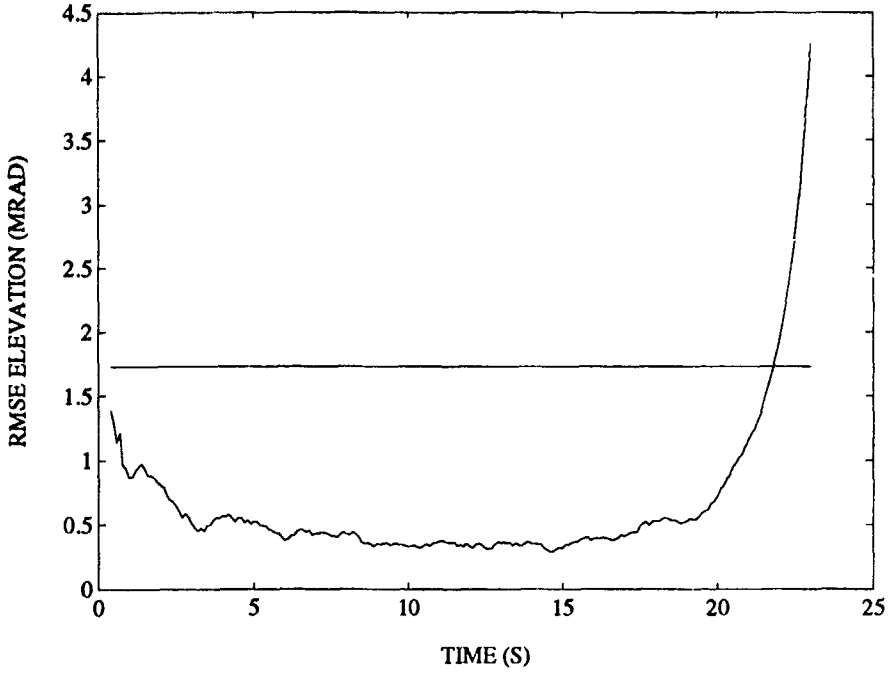

FIGURE C-35. RMS ELEVATION ERROR FOR 2 STATE FILTER ON S-TURN TARGET

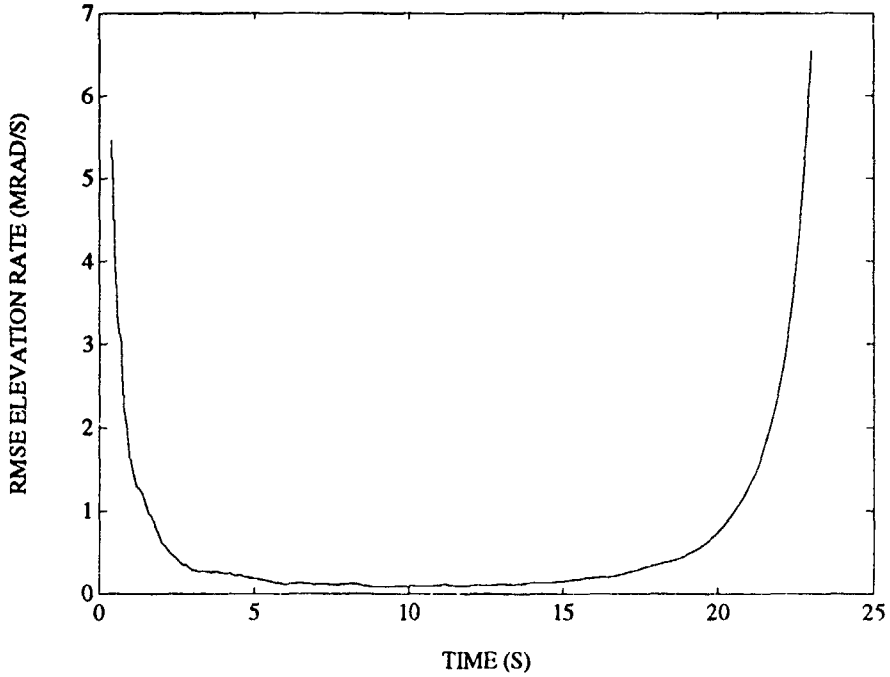

FIGURE C-36. RMS ELEVATION RATE ERROR FOR 2 STATE FILTER ON S-TURN TARGET

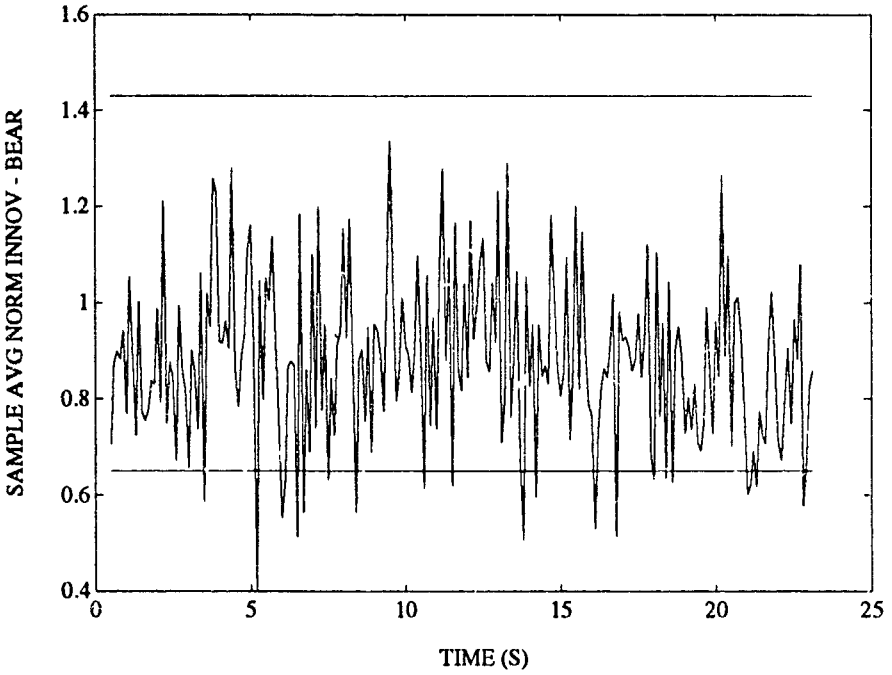

FIGURE C-37. CHI-SQUARE TEST OF BEARING INNOVATIONS FOR 2 STATE FILTER ON S-TURN TARGET

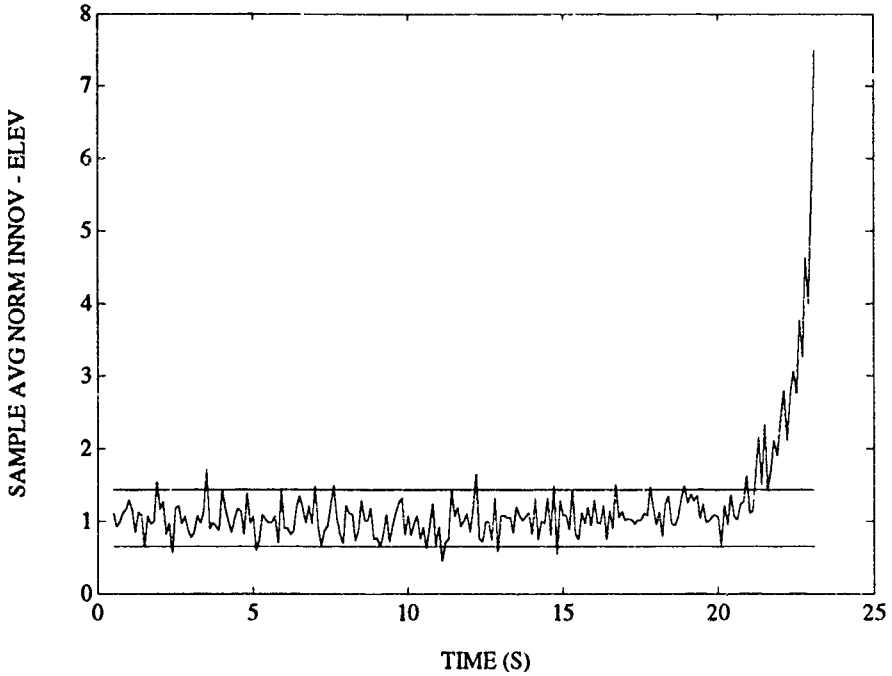

FIGURE C-38. CHI-SQUARE TEST OF ELEVATION INNOVATIONS FOR 2 STATE FILTER ON S-TURN TARGET

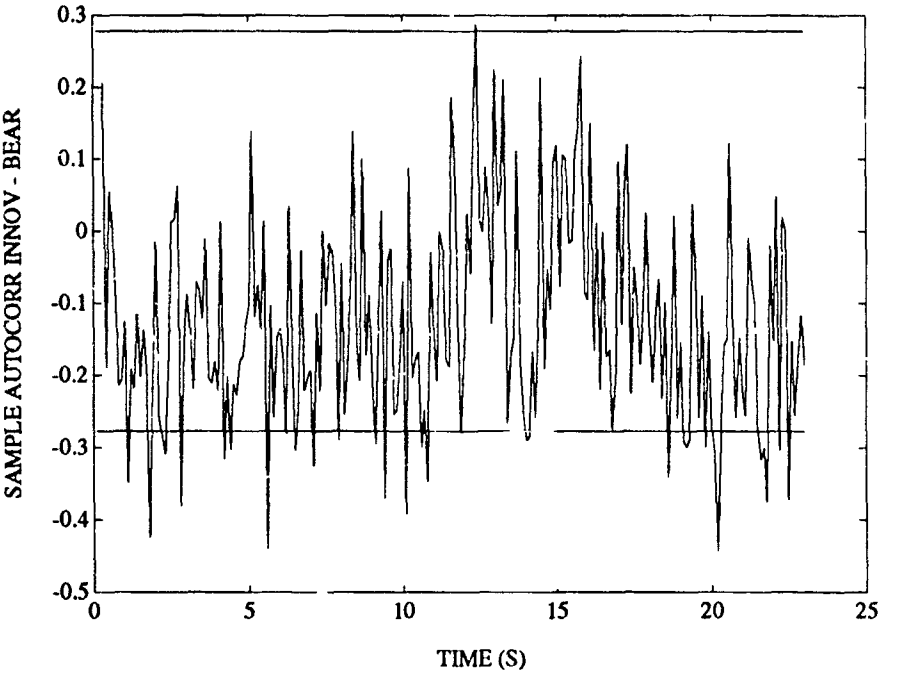

FIGURE C-39. WHITENESS TEST OF BEARING INNOVATIONS FOR 2 STATE FILTER ON S-TURN TARGET

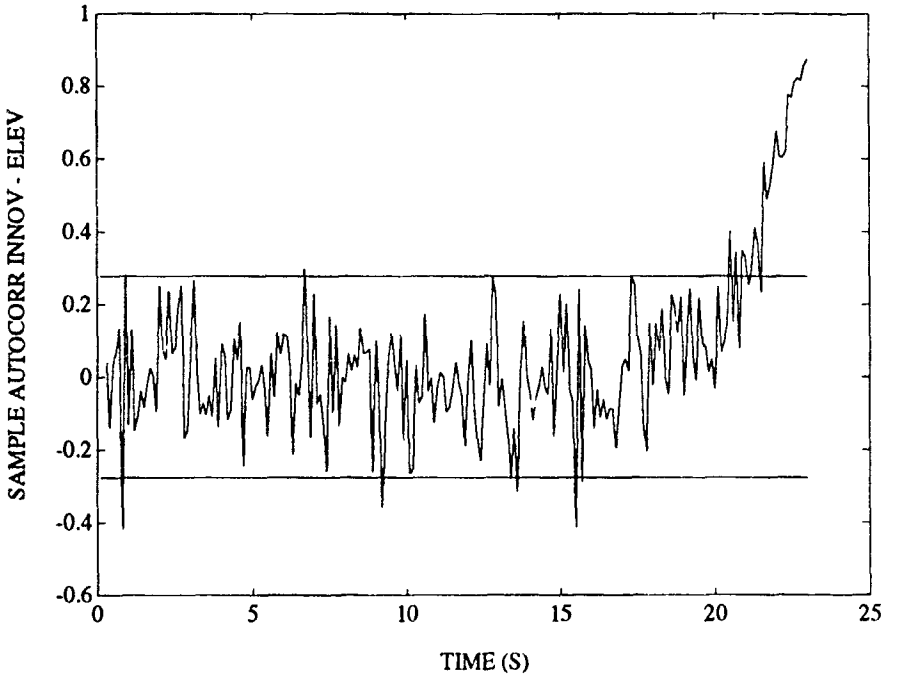

FIGURE C-40. WHITENESS TEST OF ELEVATION INNOVATIONS FOR 2 STATE FILTER ON S-TURN TARGET

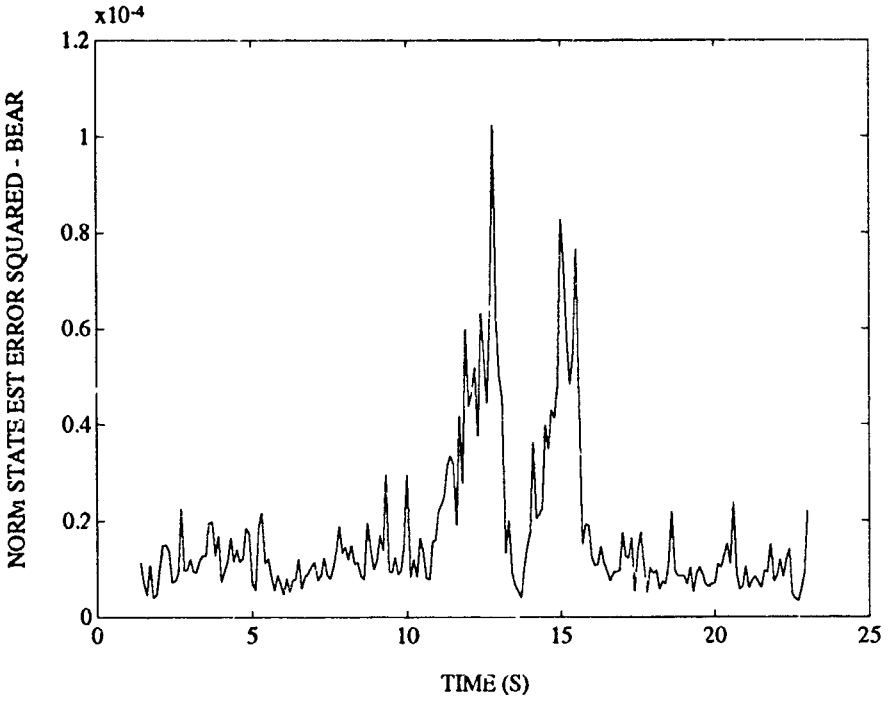

FIGURE C-41. CHI-SQUARE TEST OF BEARING ESTIMATION ERROR FOR 2 STATE FILTER ON S-TURN TARGET

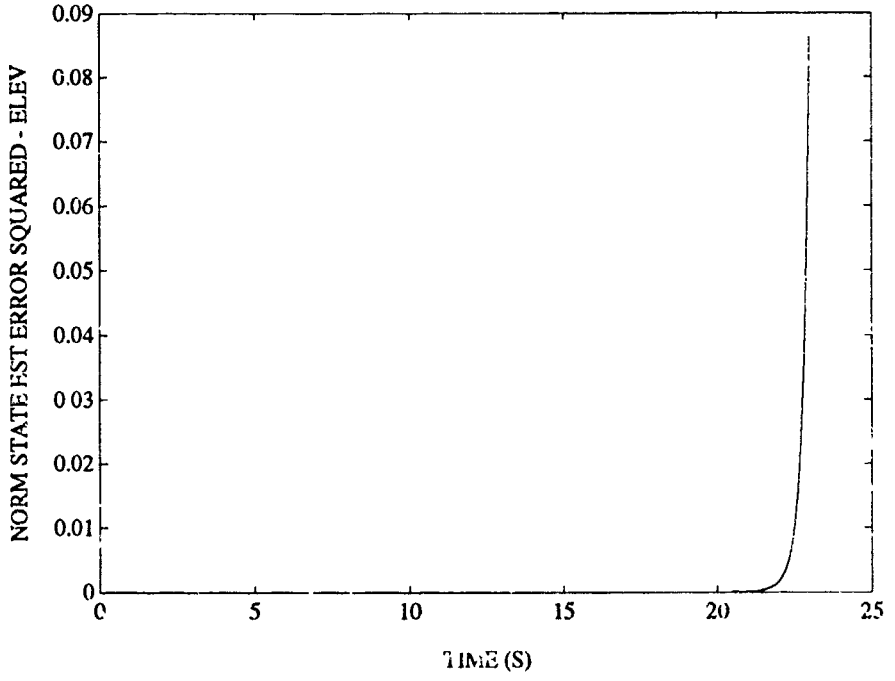

FIGURE C-42. CHI-SQUARE TEST OF ELEVATION ESTIMATION ERROR FOR 2 STATE FILTER ON S-TURN TARGET

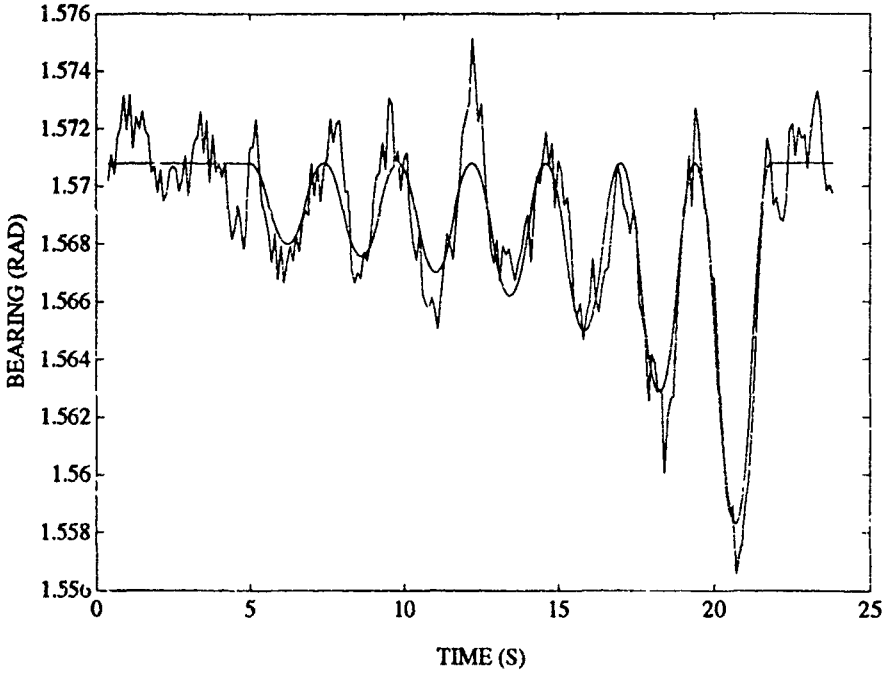

FIGURE C-43. SAMPLE BEARING ESTIMATE FOR 2 STATE FILTER ON JINKING TARGET

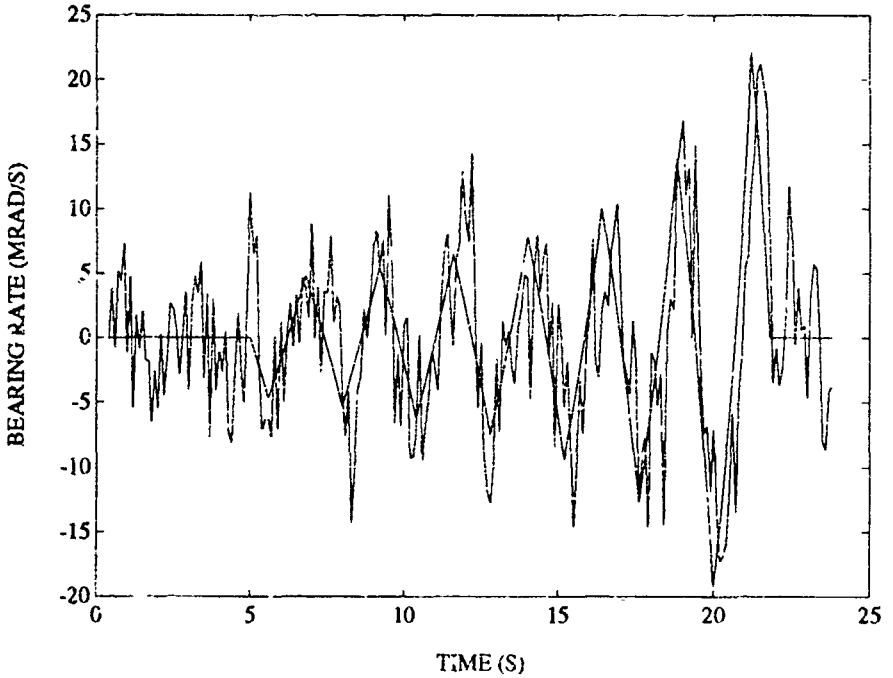

FIGURE C-44. SAMPLE BEARING RATE ESTIMATE FOR 2 STATE FILTER ON JINKING TARGET

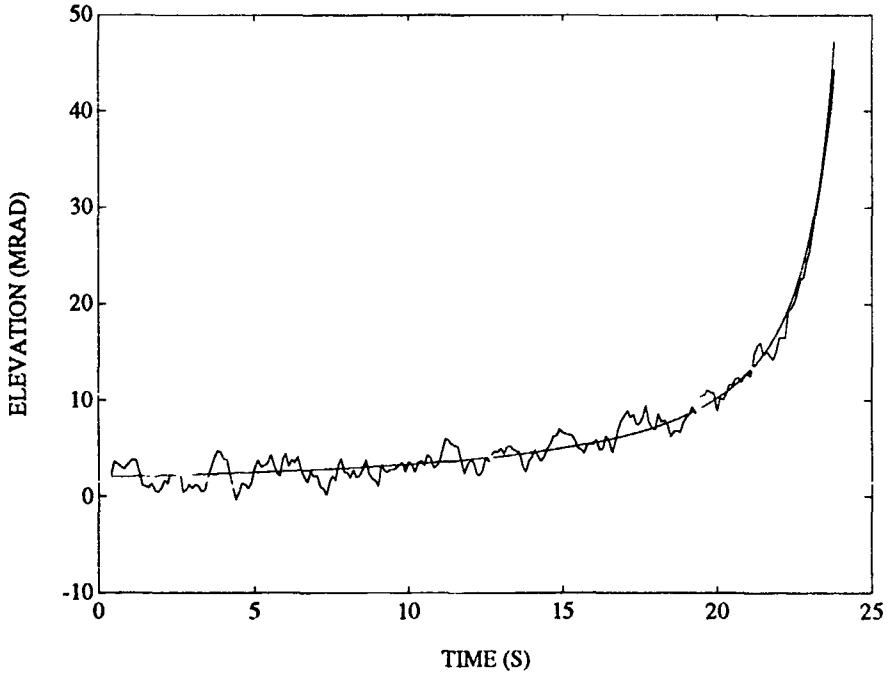

FIGURE C-45. SAMPLE ELEVATION ESTIMATE FOR 2 STATE FILTER ON JINKING TARGET

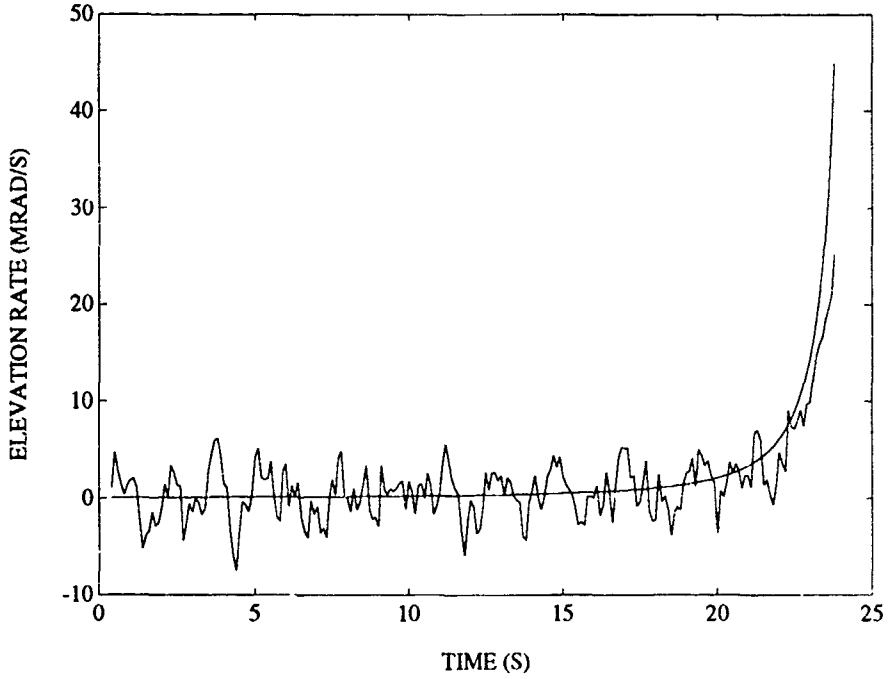

FIGURE C-46. SAMPLE ELEVATION RATE ESTIMATE FOR 2 STATE FILTER ON JINKING TARGET

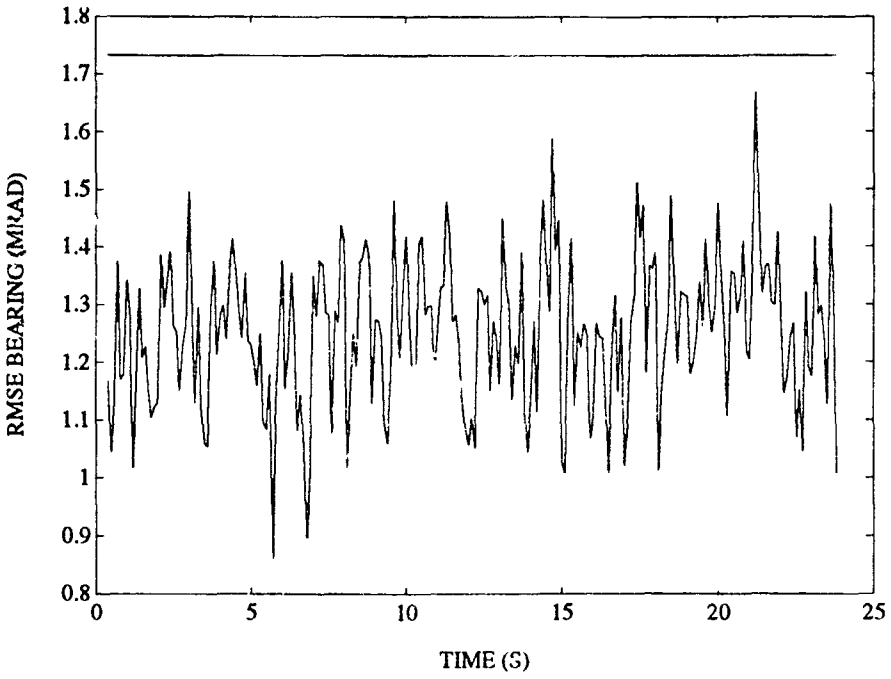

FIGURE C-47. RMS BEARING ERROR FOR 2 STATE FILTER ON JINKING TARGET

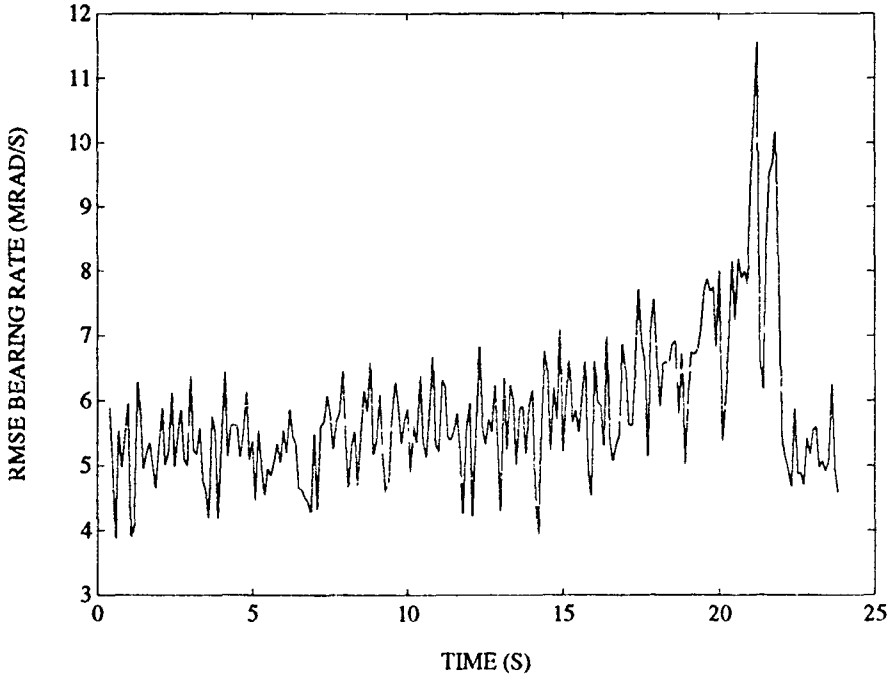

FIGURE C-48. RMS BEARING RATE ERROR FOR 2 STATE FILTER ON JINKING TARGET

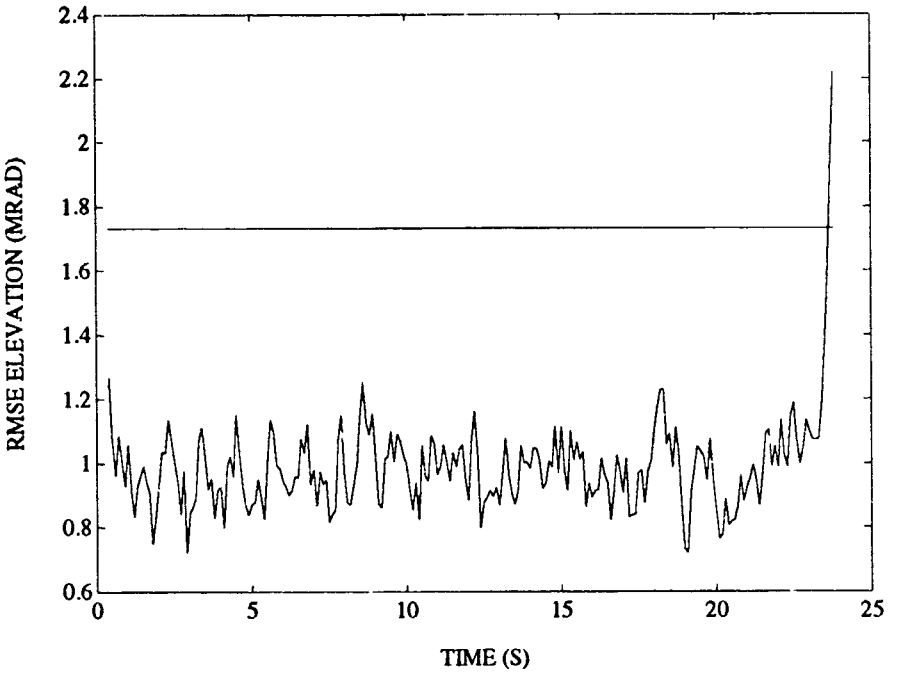

FIGURE C-49. RMS ELEVATION ERROR FOR 2 STATE FILTER ON JINKING TARGET

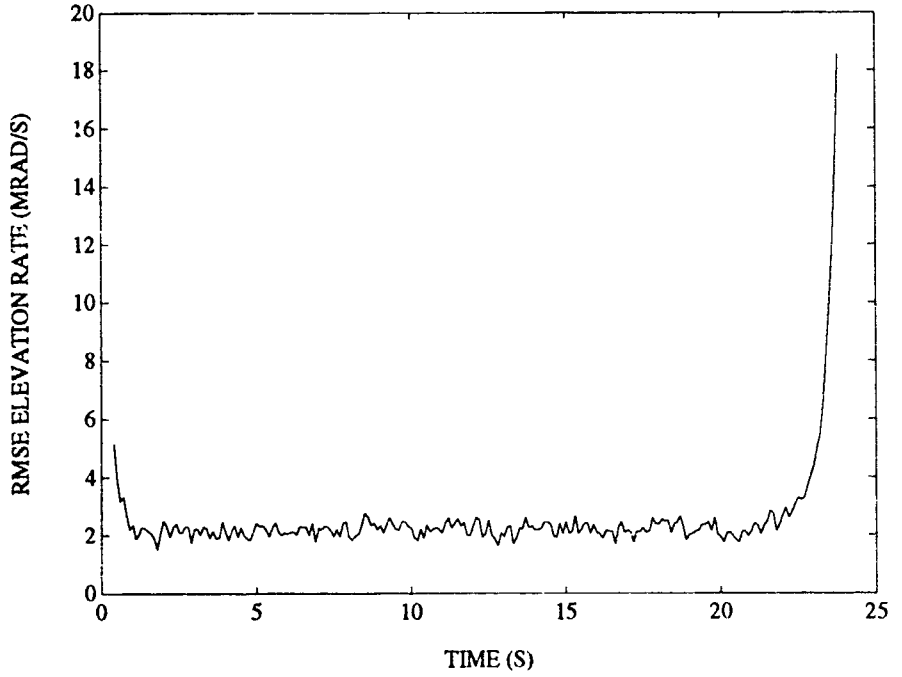

FIGURE C-50. RMS ELEVATION RATE ERROR FOR 2 STATE FILTER ON JINKING TARGET

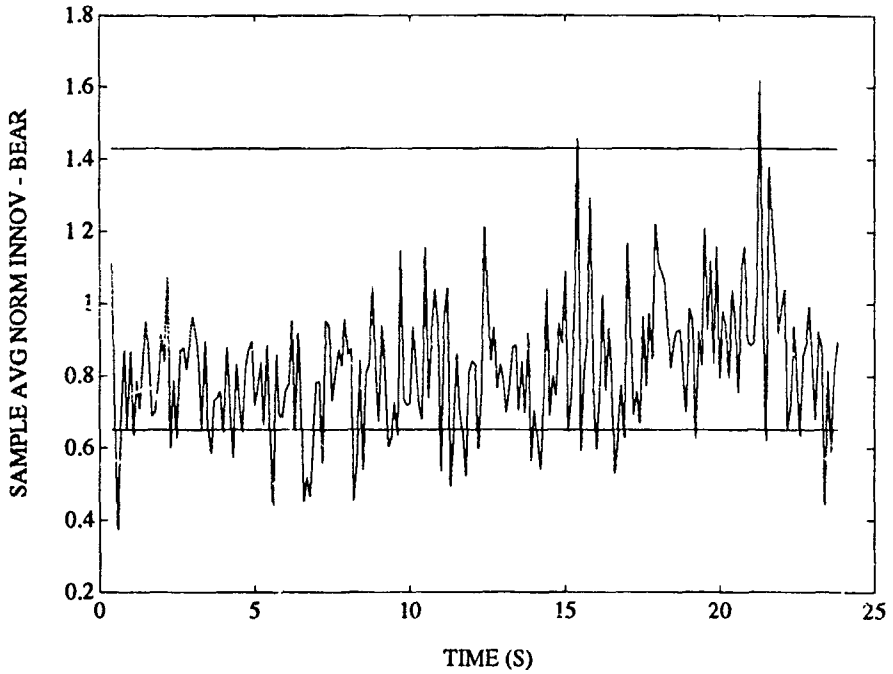

FIGURE C-51. CHI-SQUARE TEST OF BEARING INNOVATIONS FOR 2 STATE FILTER ON JINKING TARGET

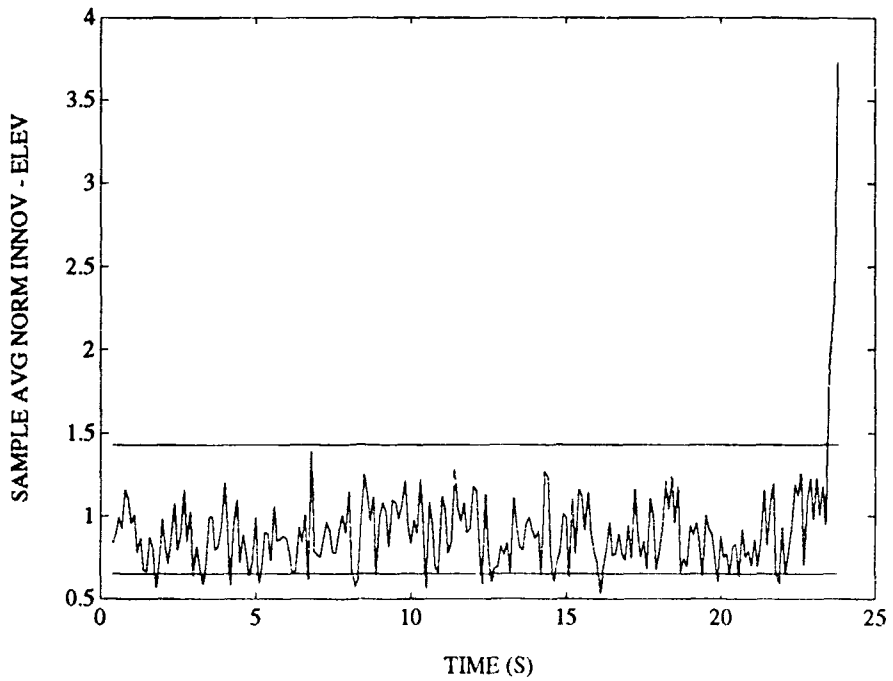

FIGURE C-52. CHI-SQUARE TEST OF ELEVATION INNOVATIONS FOR 2 STATE FILTER ON JINKING TARGET

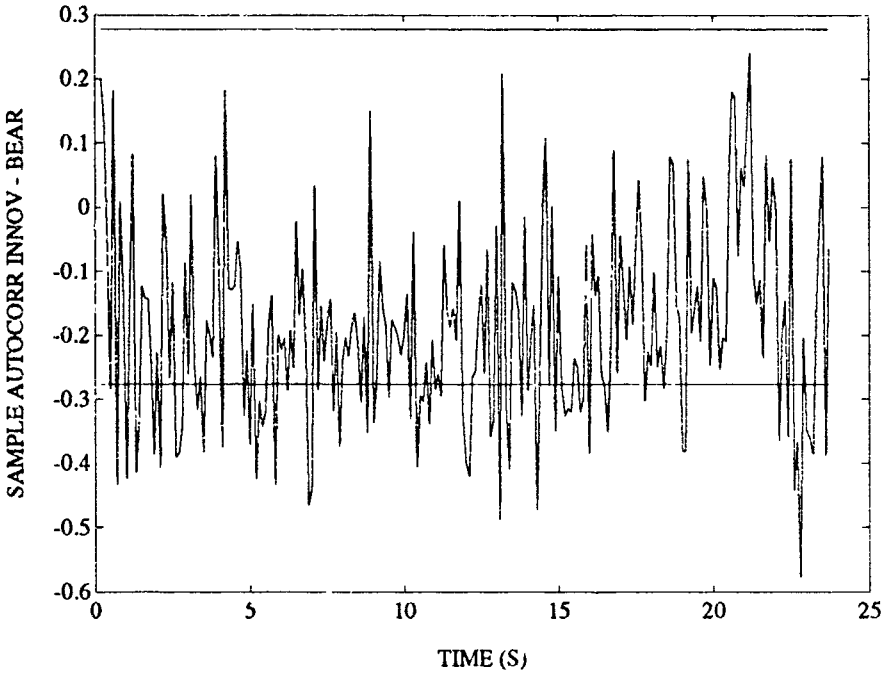

FIGURE C-53. WHITENESS TEST OF BEARING INNOVATIONS FOR 2 STATE FILTER ON JINKING TARGET

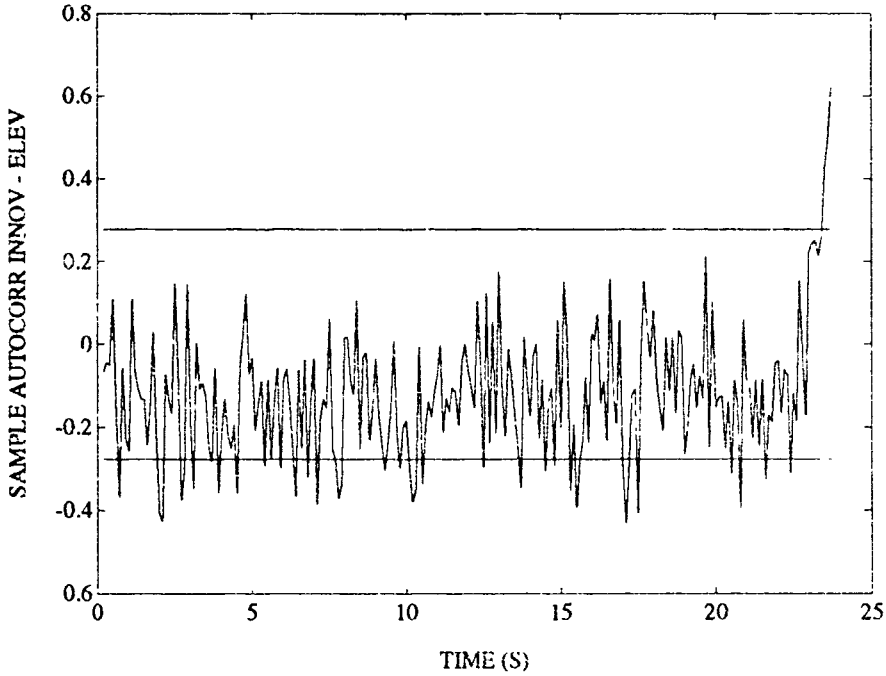

FIGURE C-54. WHITENESS TEST OF ELEVATION INNOVATIONS FOR 2 STATE FILTER ON JINKING TARGET

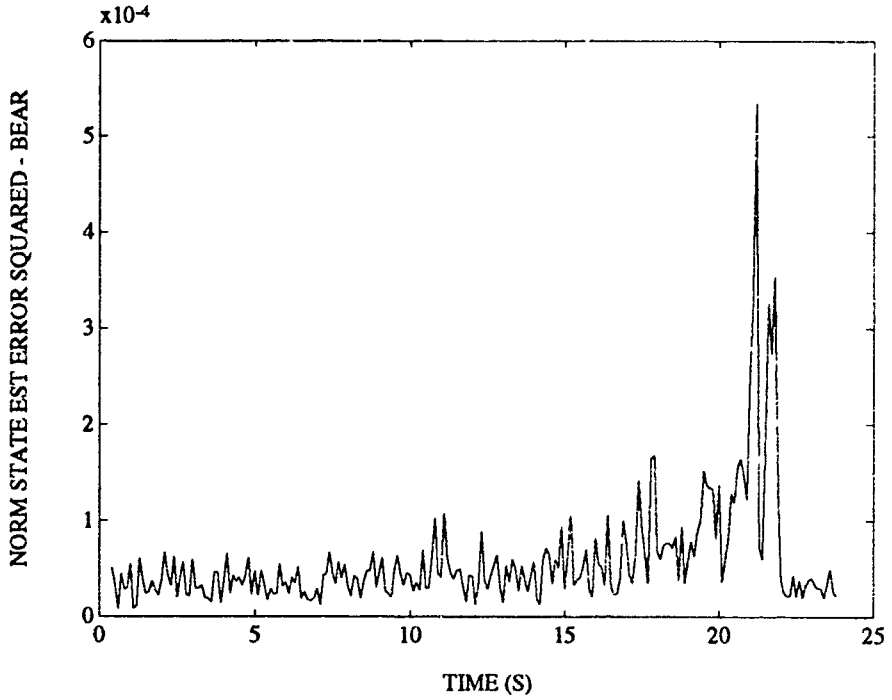

FIGURE C-55. CHI-SQUARE TEST OF BEARING ESTIMATION ERROR FOR 2 STATE FILTER ON JINKING TARGET

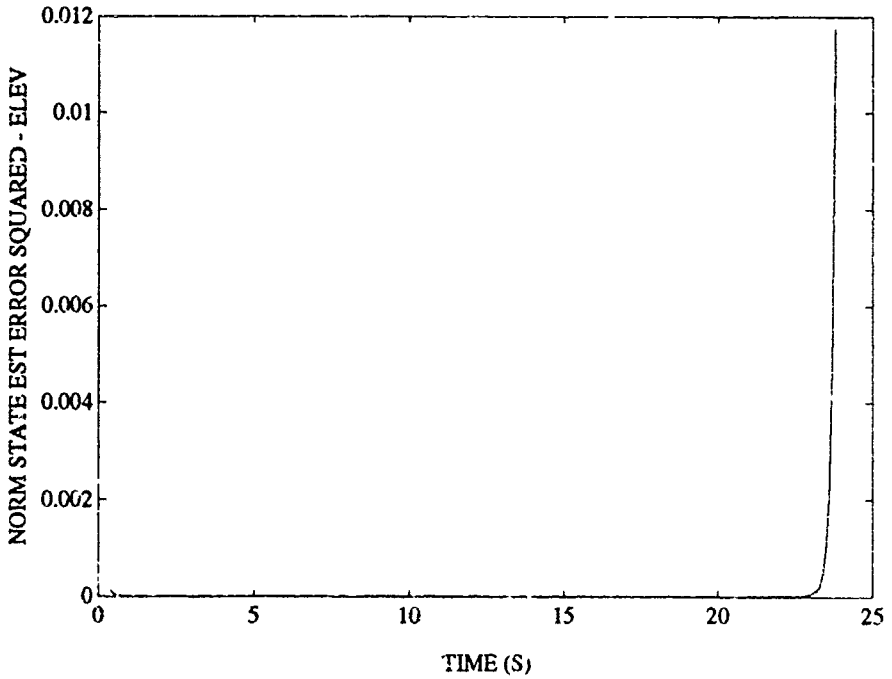

FIGURE C-56. CHI-SQUARE TEST OF ELEVATION ESTIMATION ERROR FOR 2 STATE FILTER ON JINKING TARGET

APPENDIX D
PLOTS OF 3 STATE FILTER RESULTS

This appendix presents the results of simulations performed fo. .he 3 state filters. The results are presented in the following order: radial target, crossing target, S-turn target, and jinking target.

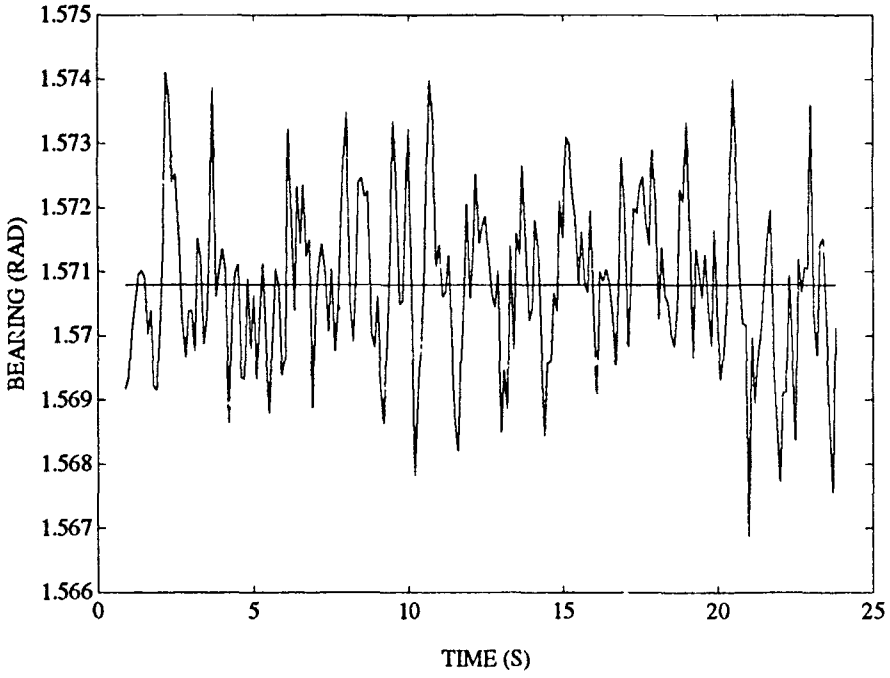

FIGURE D-1. SAMPLE BEARING ESTIMATE FOR 3 STATE FILTER ON RADIAL TARGET

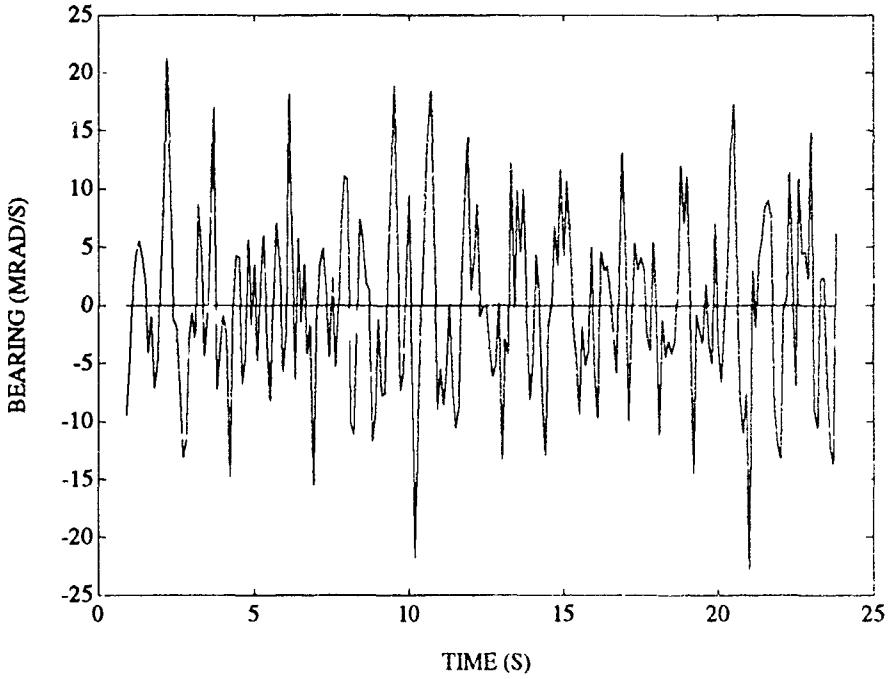

FIGURE D-2. SAMPLE BEARING RATE ESTIMATE FOR 3 STATE FILTER ON RADIAL TARGET

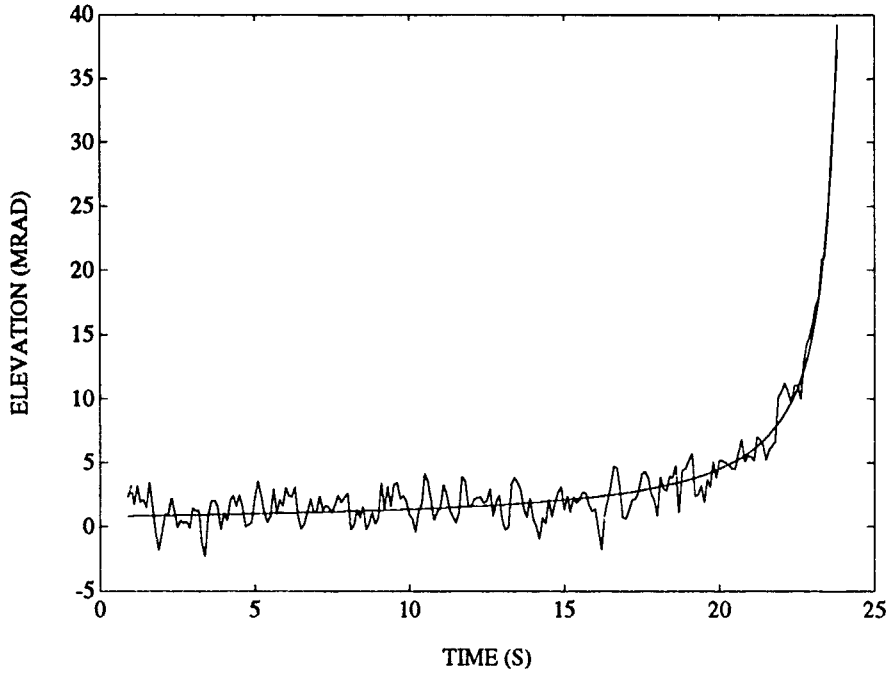

FIGURE D-3. SAMPLE ELEVATION ESTIMATE FOR 3 STATE FILTER ON RADIAL TARGET

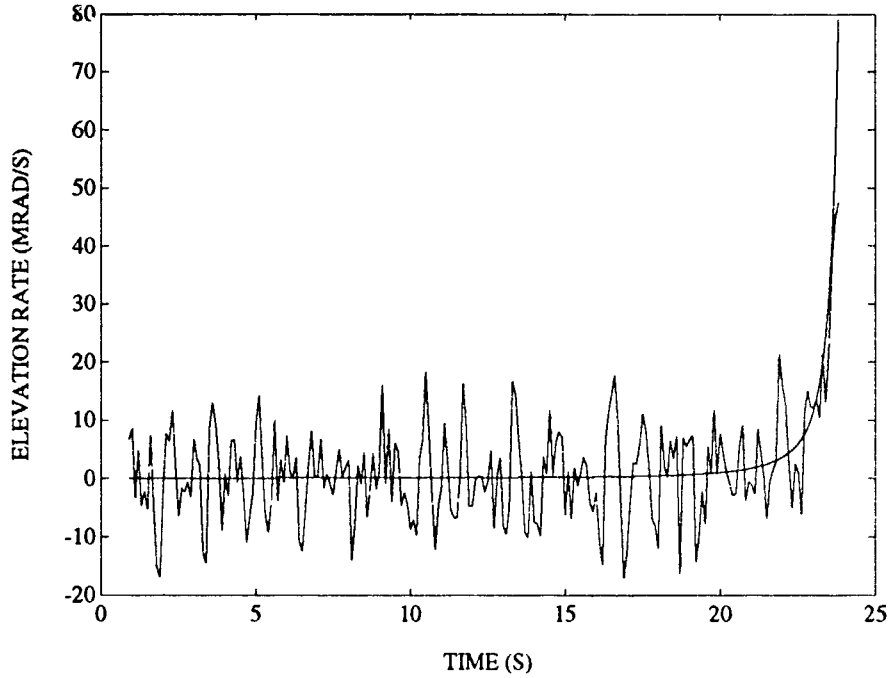

FIGURE D-4. SAMPLE ELEVATION RATE ESTIMATE FOR 3 STATE FILTER ON RADIAL TARGET

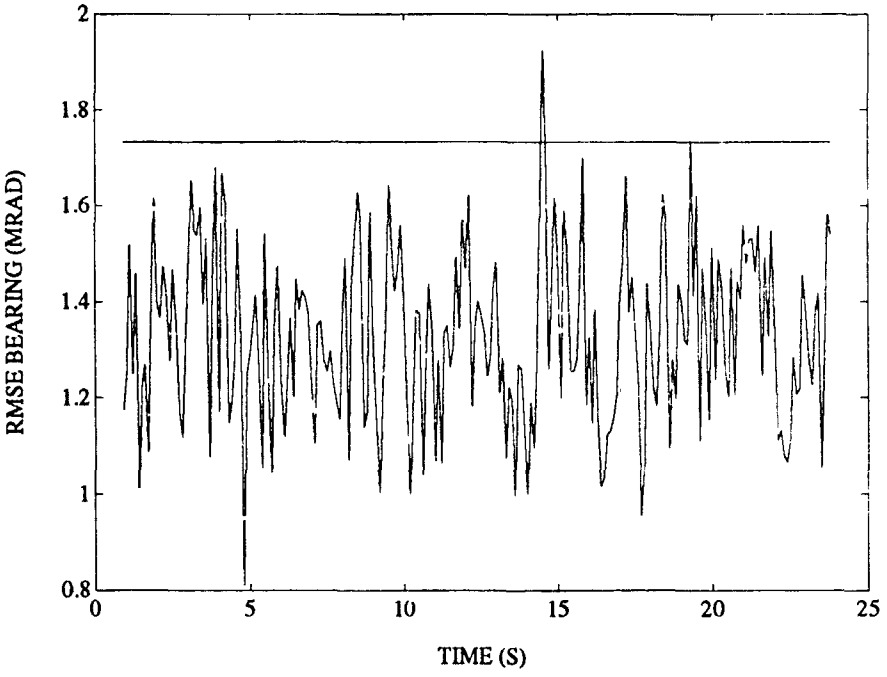

FIGURE D-5. RMS BEARING ERROR FOR 3 STATE FILTER ON RADIAL TARGET

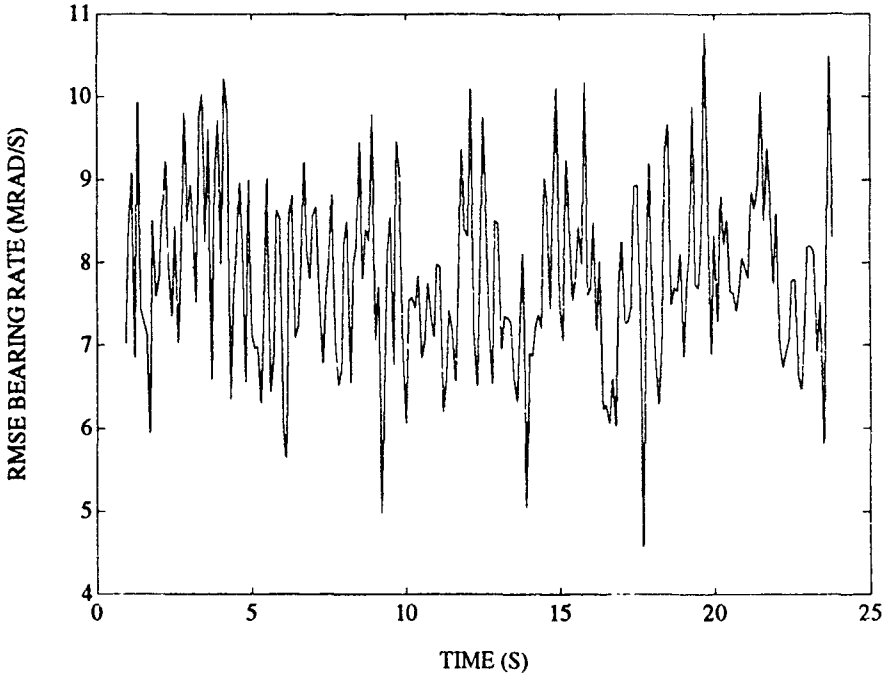

FIGURE D-6. RMS BEARING RATE ERROR FOR 3 STATE FILTER ON RADIAL TARGET

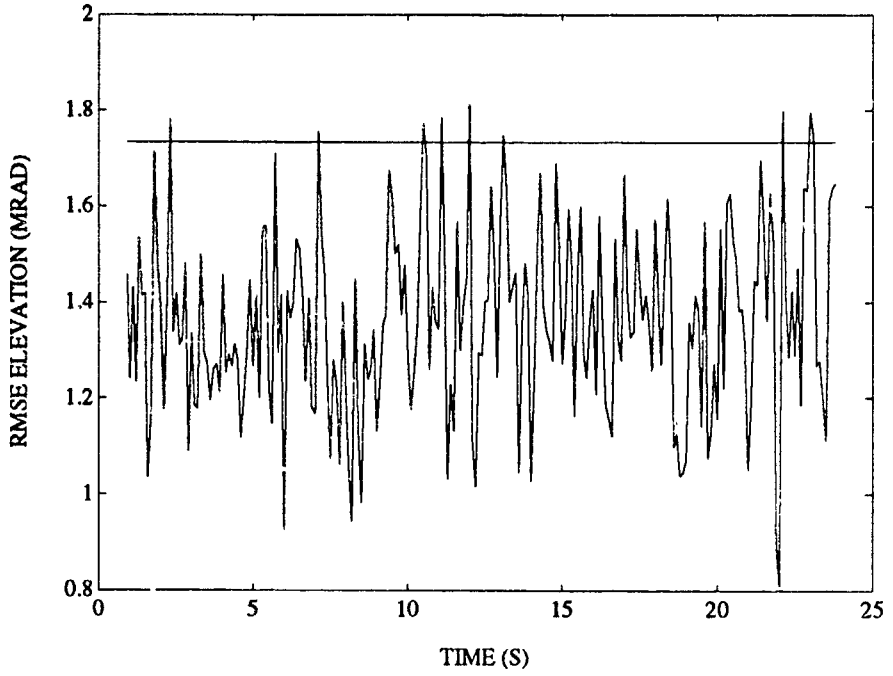

FIGURE D-7. RMS ELEVATION ERROR FOR 3 STATE FILTER ON RADIAL TARGET

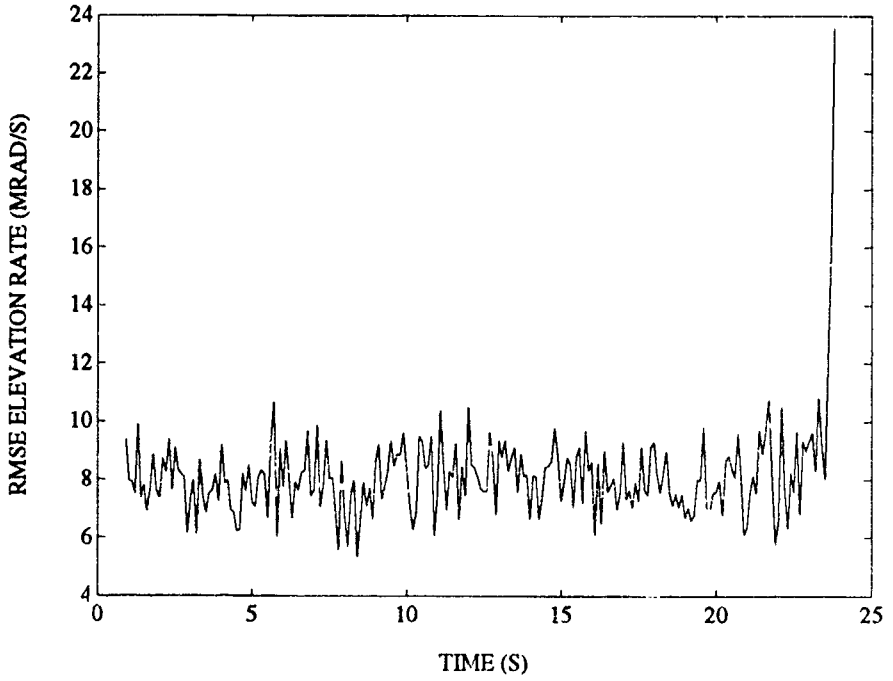

FIGURE D-8. RMS ELEVATION RATE ERROR FOR 3 STATE FILTER ON RADIAL TARGET

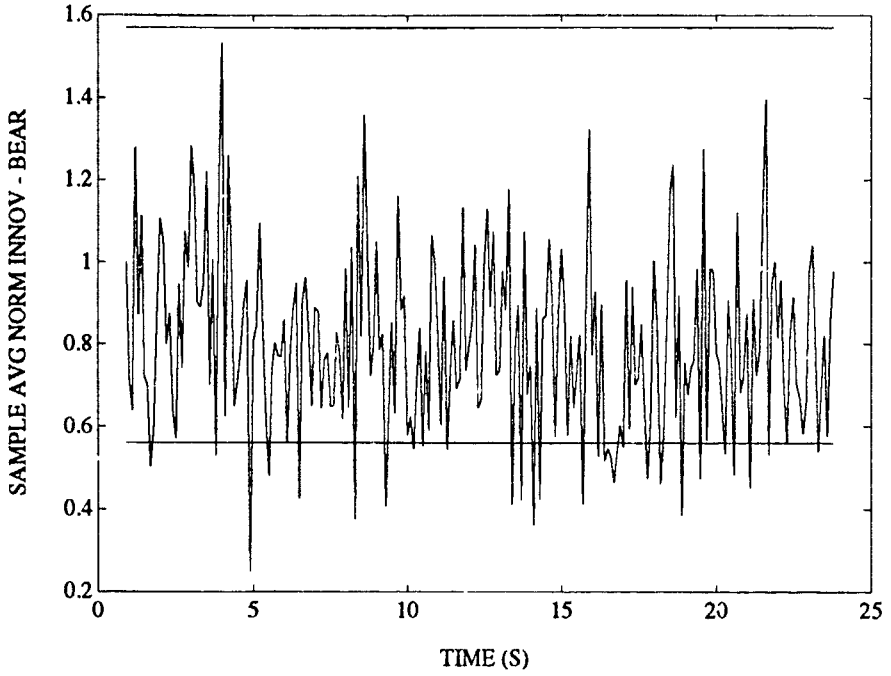

FIGURE D-9. CHI-SQUARE TEST OF BEARING INNOVATIONS FOR 3 STATE FILTER ON RADIAL TARGET

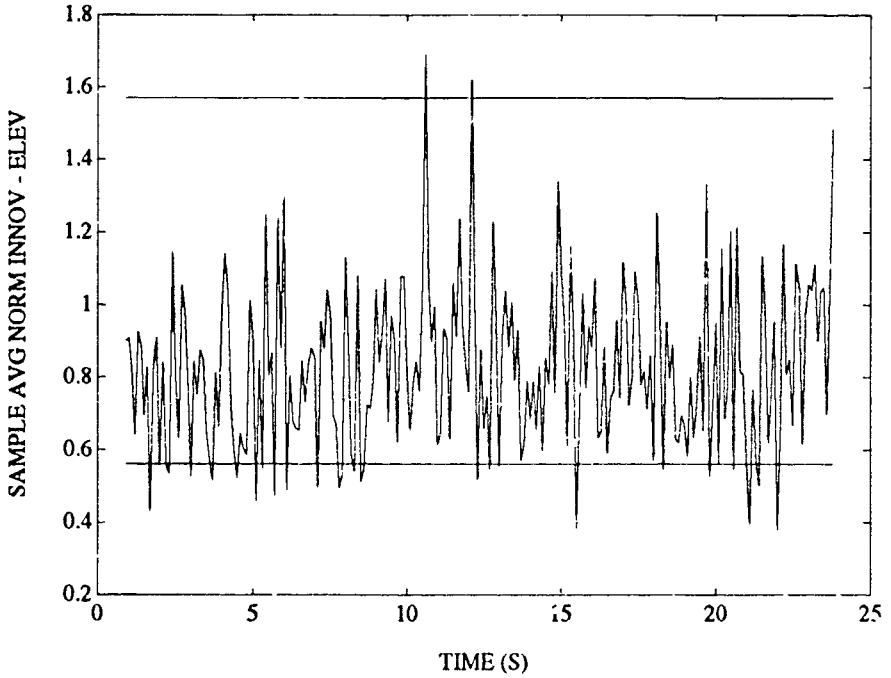

FIGURE D-10. CHI-SQUARE TEST OF ELEVATION INNOVATIONS FOR 3 STATE FILTER ON RADIAL TARGET

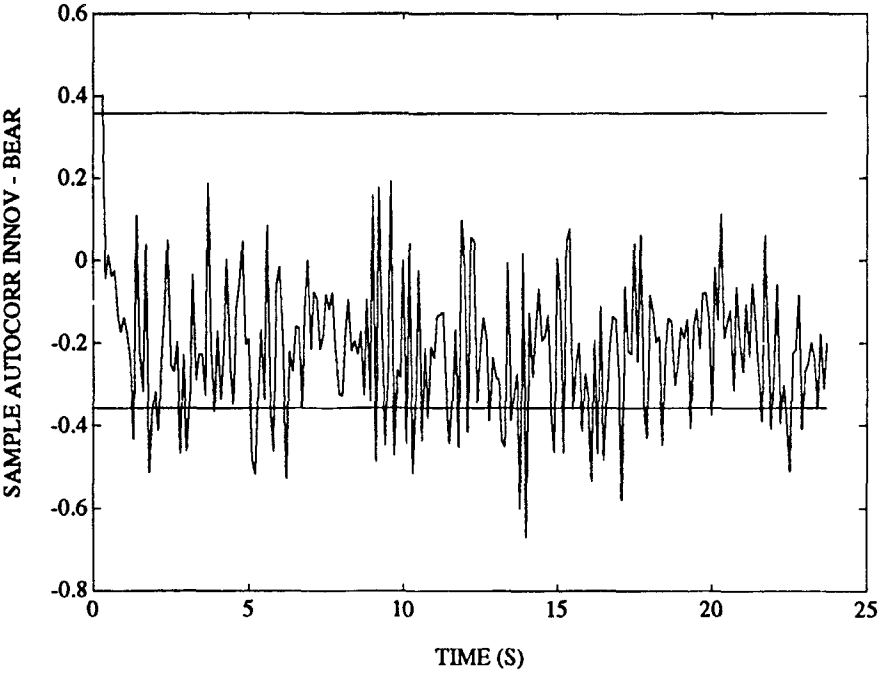

FIGURE D-11. WHITENESS TEST OF BEARING INNOVATIONS FOR 3 STATE FILTER ON RADIAL TARGET

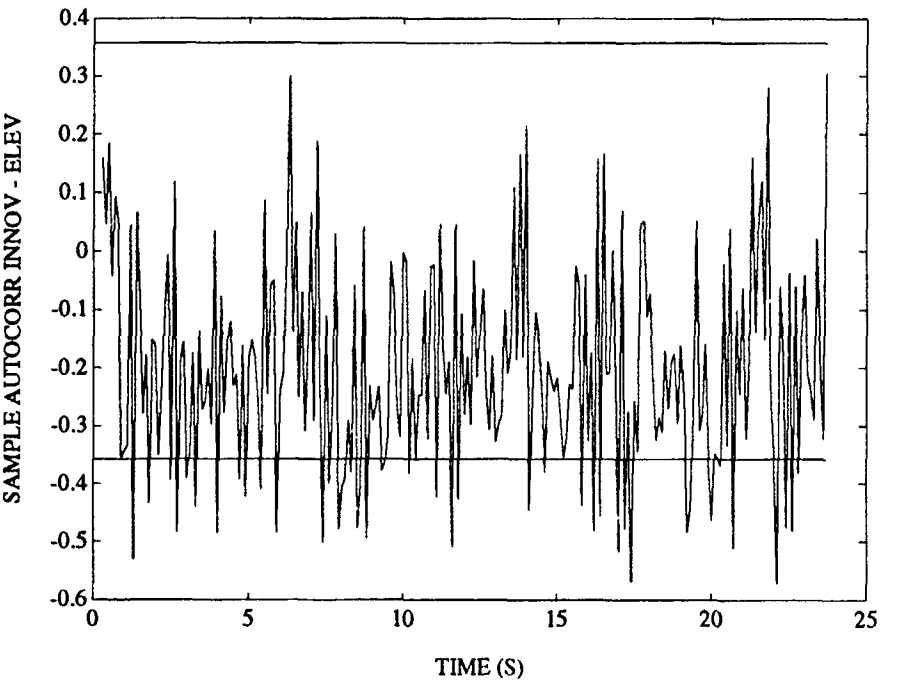

FIGURE D-12. WHITENESS TEST OF ELEVATION INNOVATIONS FOR 3 STATE FILTER ON RADIAL TARGET

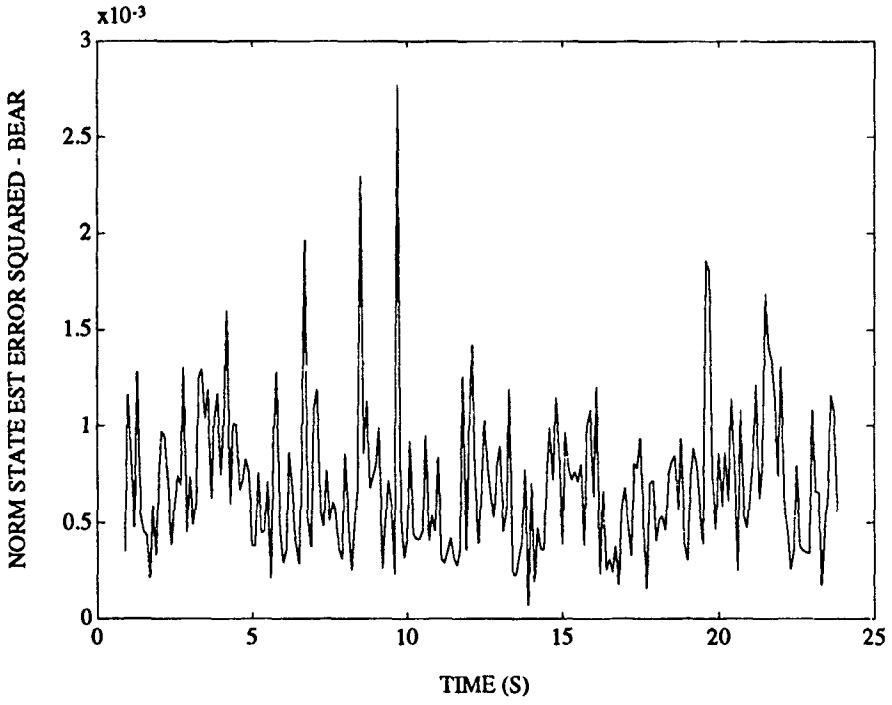

FIGURE D-13. CHI-SQUARE TEST OF BEARING ESTIMATION ERROR FOR 3 STATE FILTER ON RADIAL TARGET

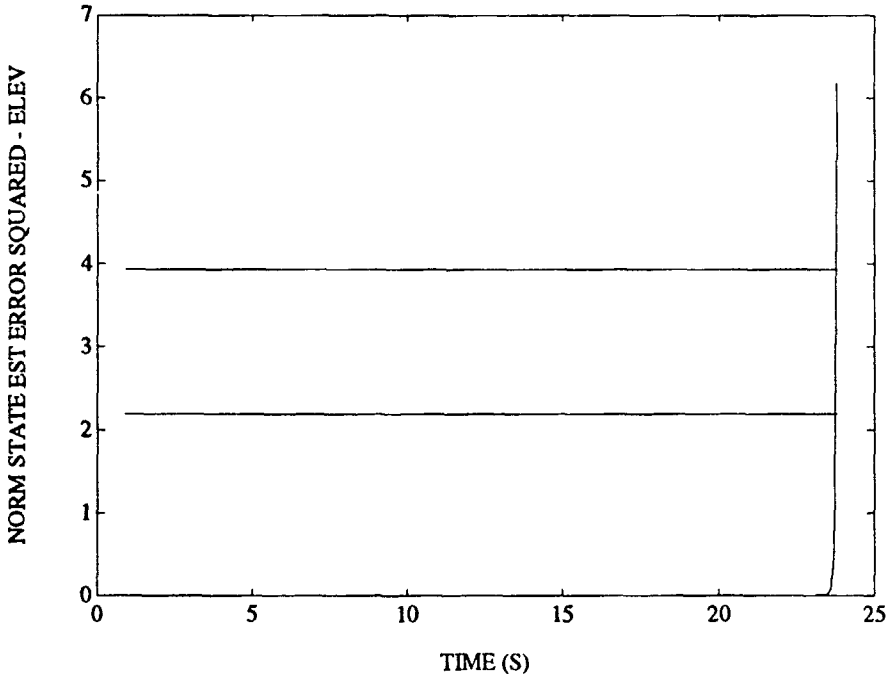

FIGURE D-14. CHI-SQUARE TEST OF ELEVATION ESTIMATION ERROR FOR 3 STATE FILTER ON RADIAL TARGET

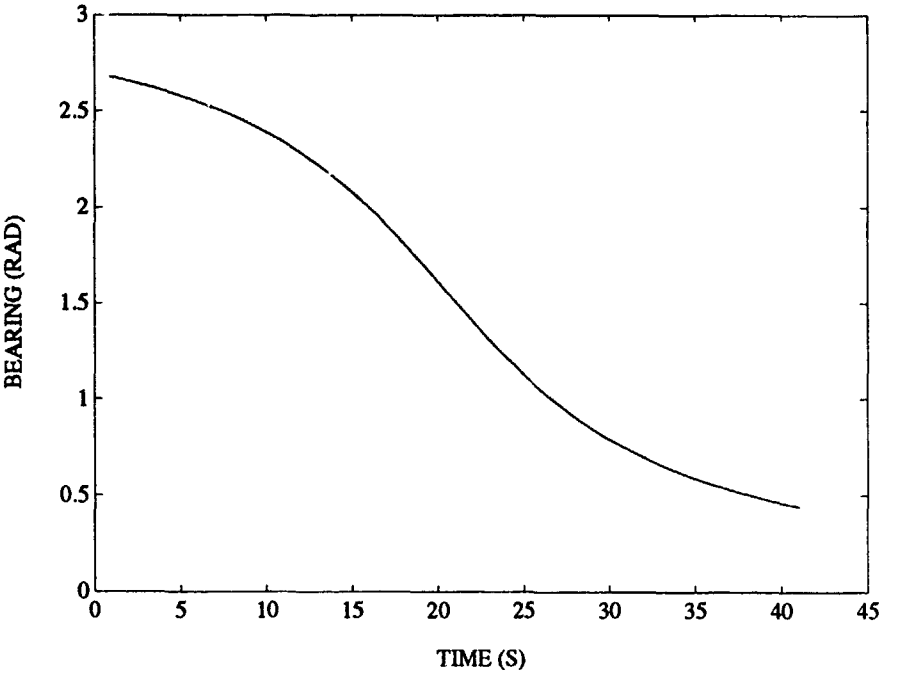

FIGURE D-15. SAMPLE BEARING ESTIMATE FOR 3 STATE FILTER ON CROSSING TARGET

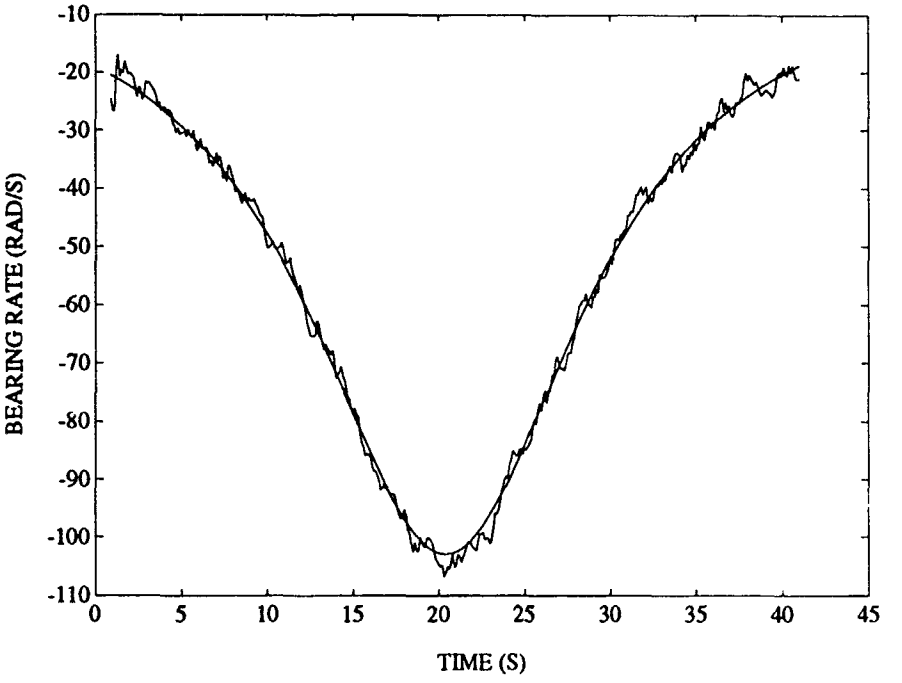

FIGURE D-16. SAMPLE BEARING RATE ESTIMATE FOR 3 STATE FILTER ON CROSSING TARGET

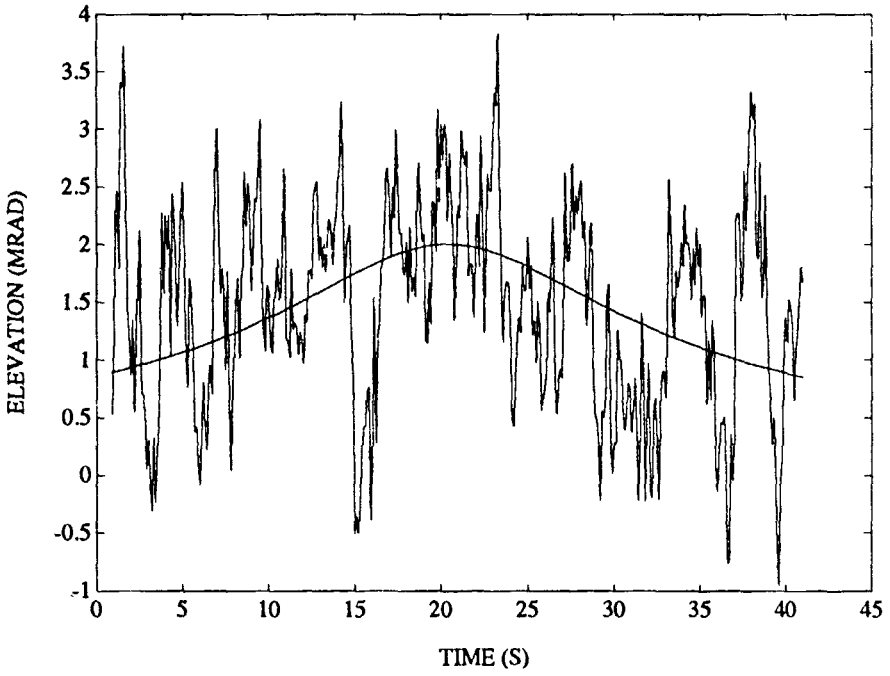

FIGURE D-17. SAMPLE ELEVATION ESTIMATE FOR 3 STATE FILTER ON CROSSING TARGET

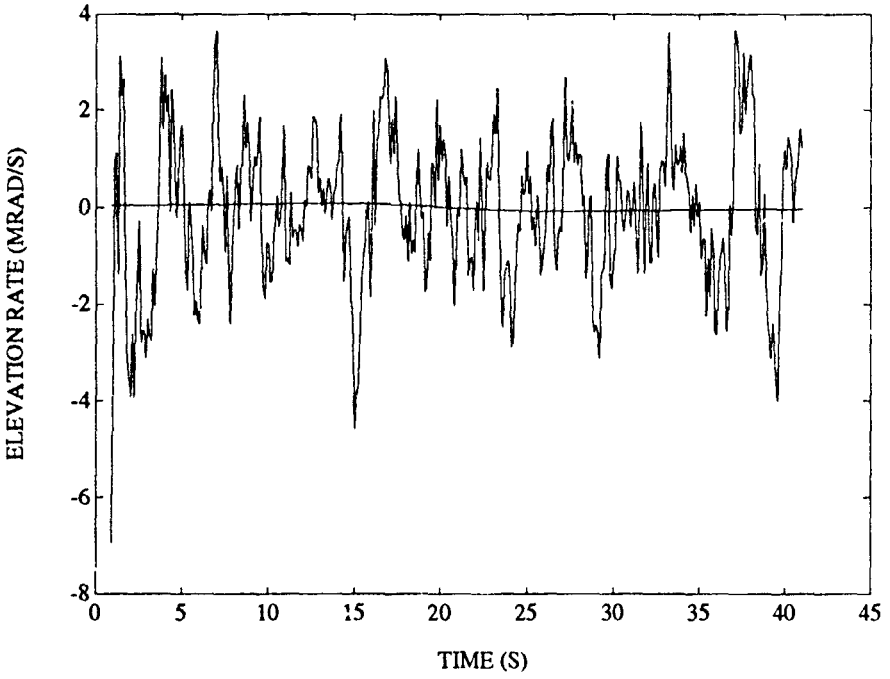

FIGURE D-18. SAMPLE ELEVATION RATE ESTIMATE FOR 3 STATE FILTER ON CROSSING TARGET

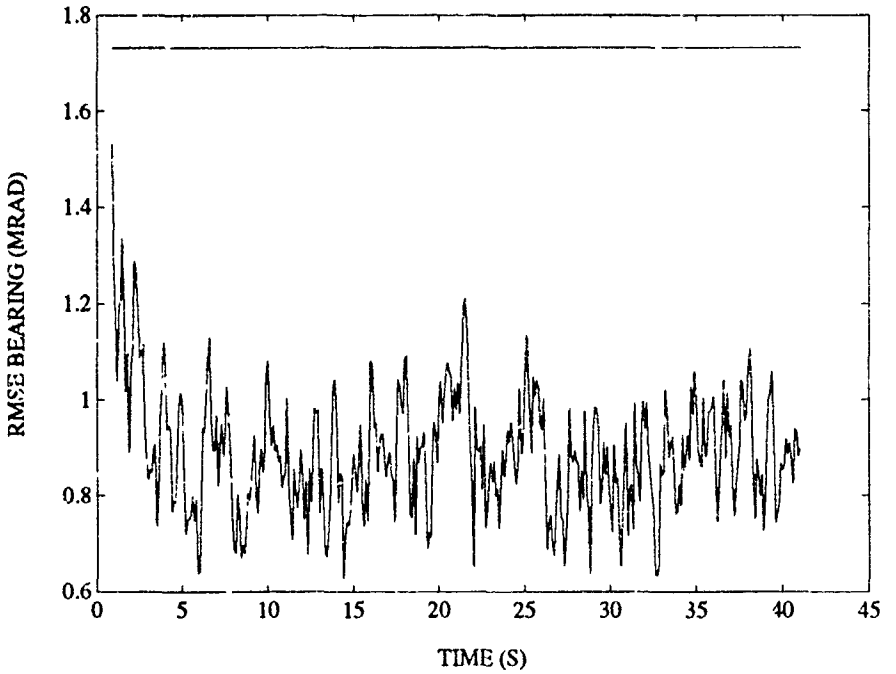

FIGURE D-19. RMS BEARING ERROR FOR 3 STATE FILTER ON CROSSING TARGET

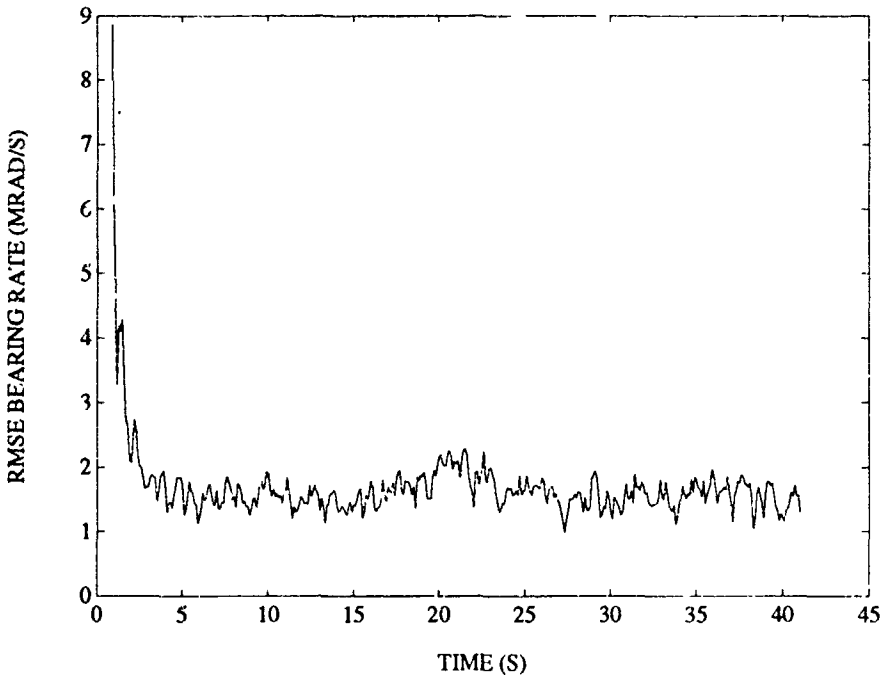

FIGURE D-20. RMS BEARING RATE ERROR FOR 3 STATE FILTER ON CROSSING TARGET

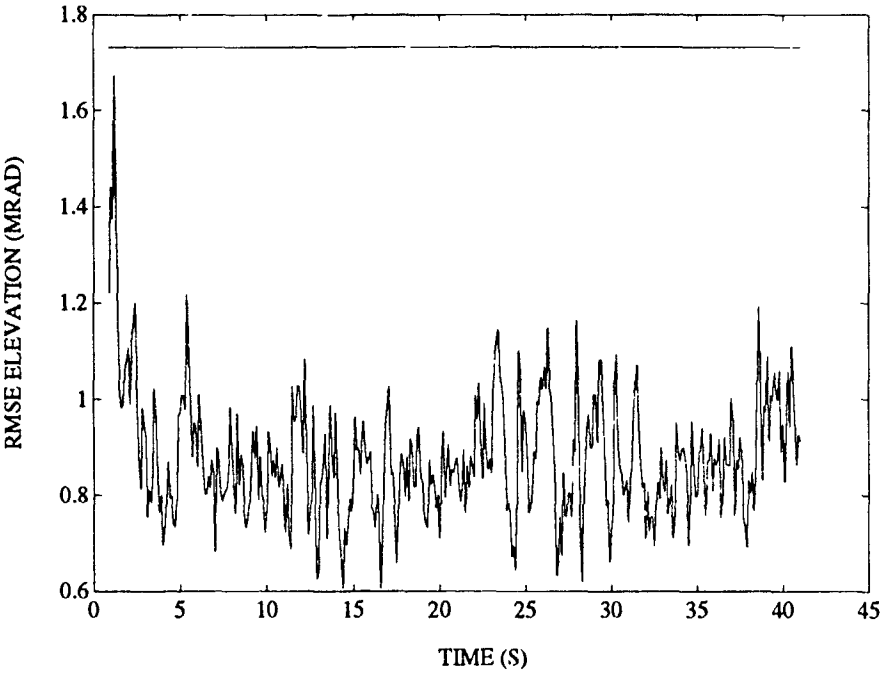

FIGURE D-21. RMS ELEVATION ERROR FOR 3 STATE FILTER ON CROSSING TARGET

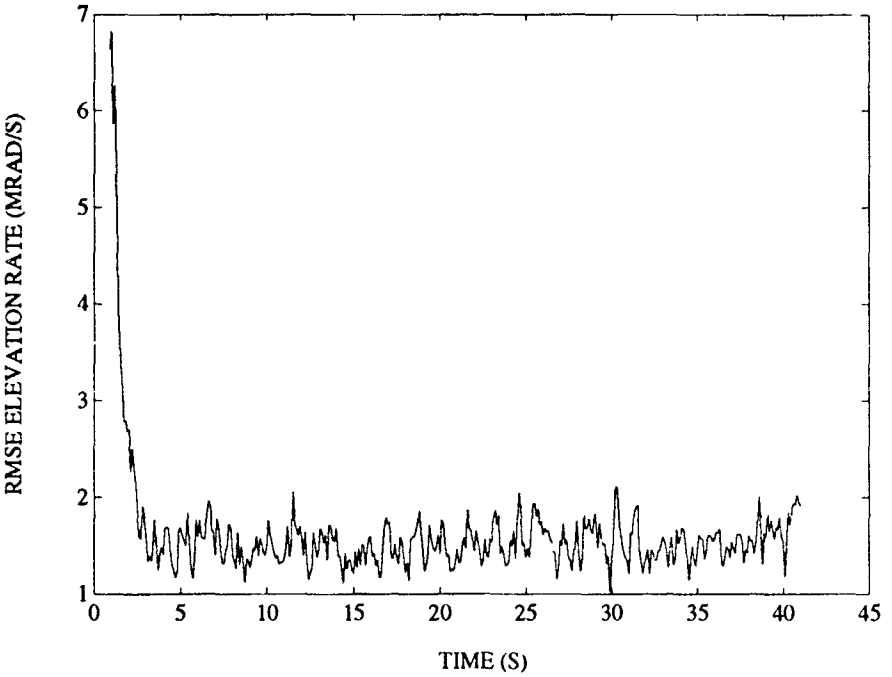

FIGURE D-22. RMS ELEVATION RATE ERROR FOR 3 STATE FILTER ON CROSSING TARGET

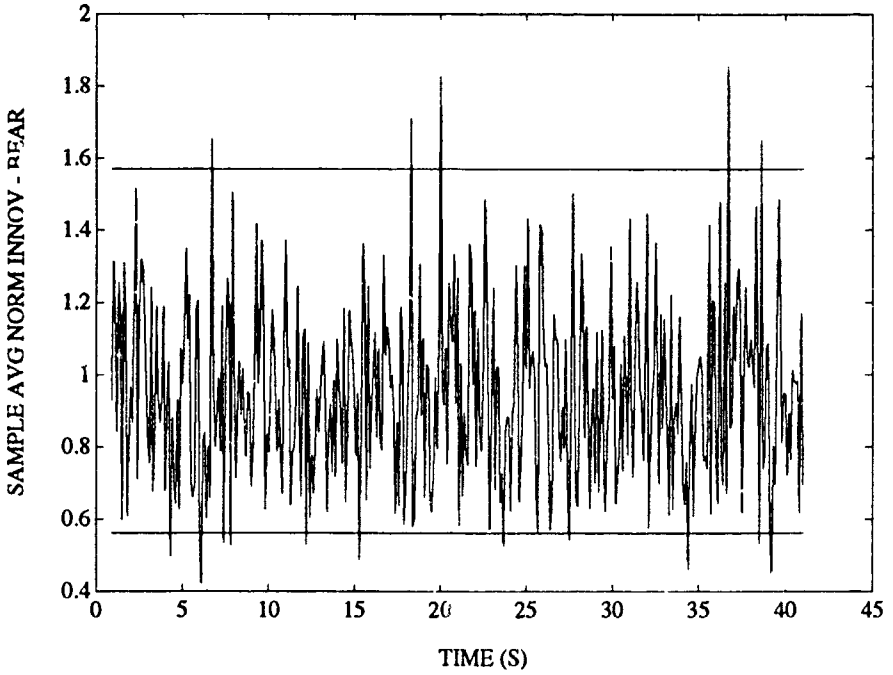

FIGURE D-23. CHI-SQUARE TEST OF BEARING INNOVATIONS FOR 3 STATE FILTER ON CROSSING TARGET

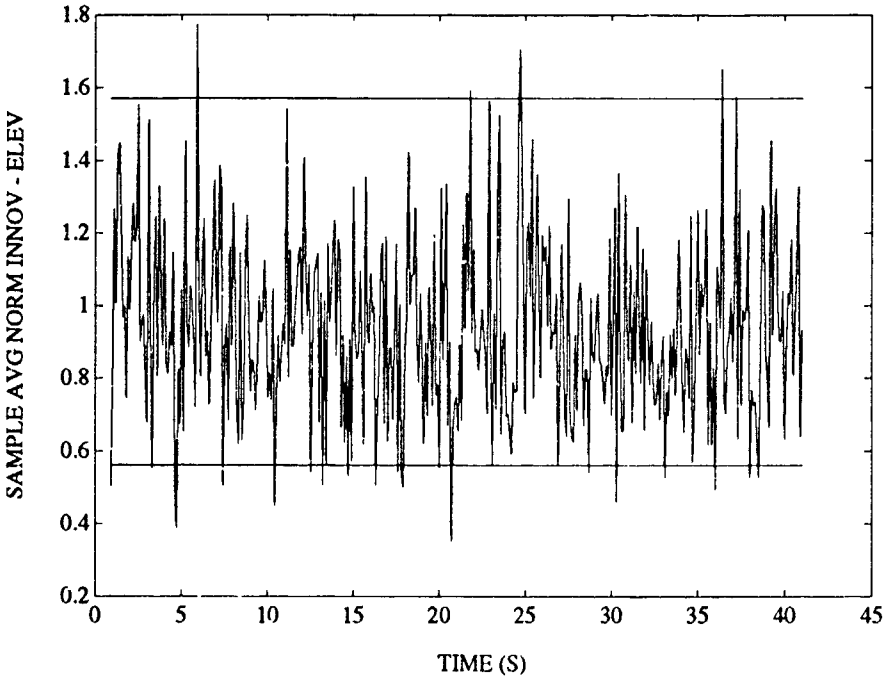

FIGURE D-24. CHI-SQUARE TEST OF ELEVATION INNOVATIONS FOR 3 STATE FILTER ON CROSSING TARGET

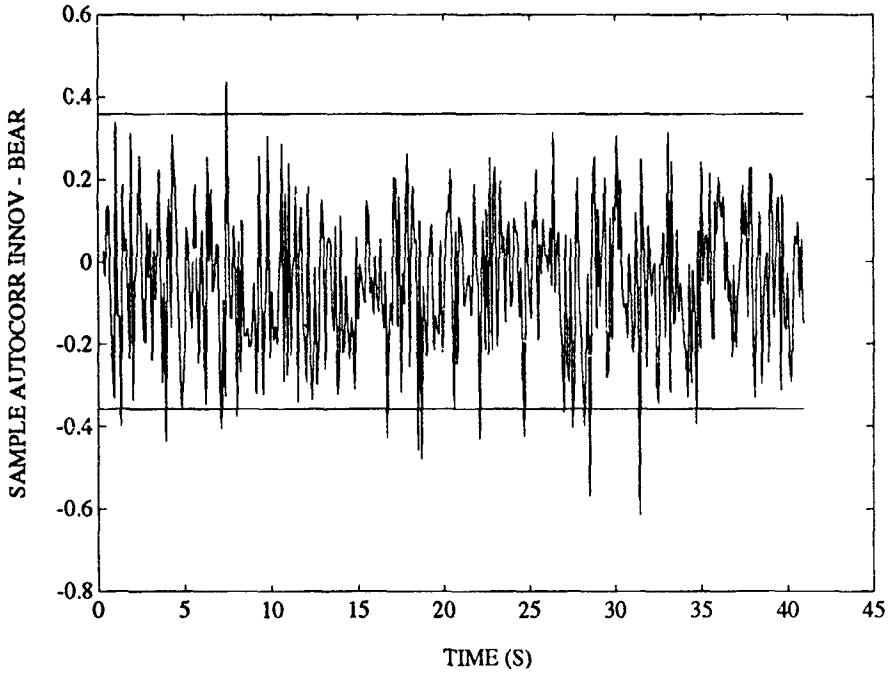

FIGURE D-25. WHITENESS TEST OF BEARING INNOVATIONS FOR 3 STATE FILTER ON CROSSING TARGET

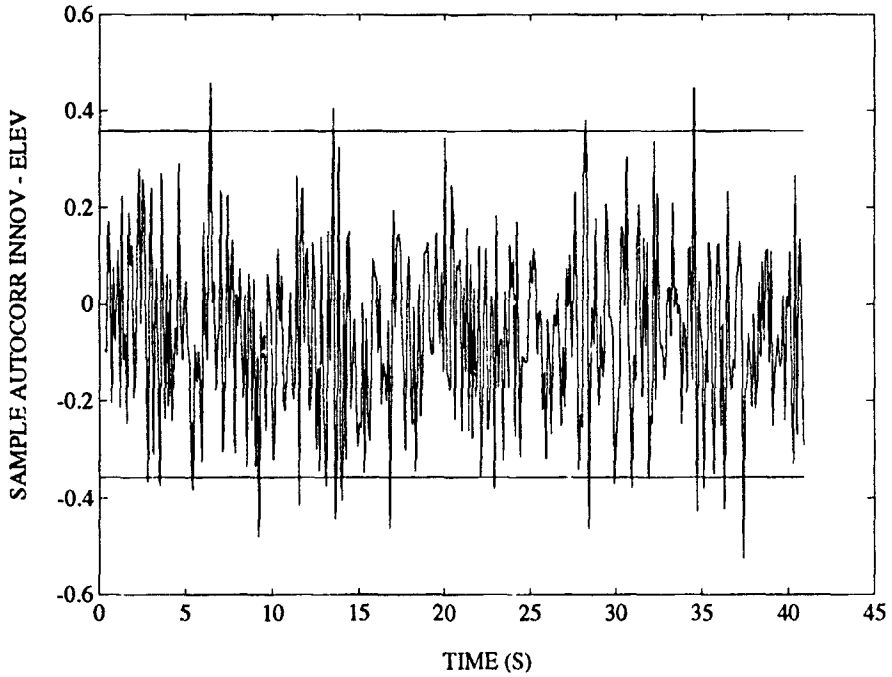

FIGURE D-26. WHITENESS TEST OF ELEVATION INNOVATIONS FOR STATE FILTER ON CROSSING TARGET

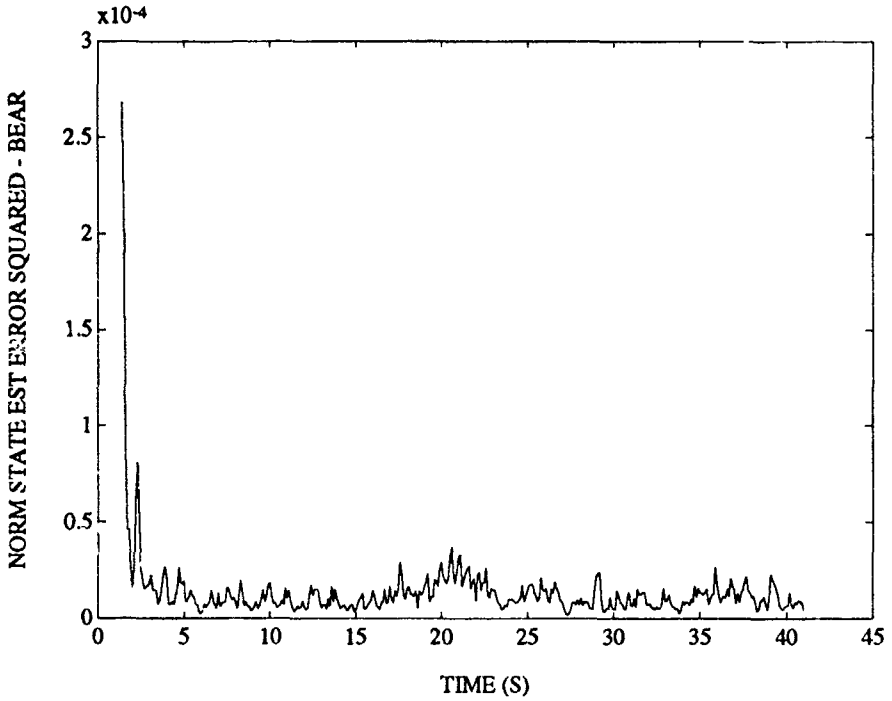

FIGURE D-27. CHI-SQUARE TEST OF BEARING ESTIMATION ERROR FOR 3 STATE FILTER ON CROSSING TARGET

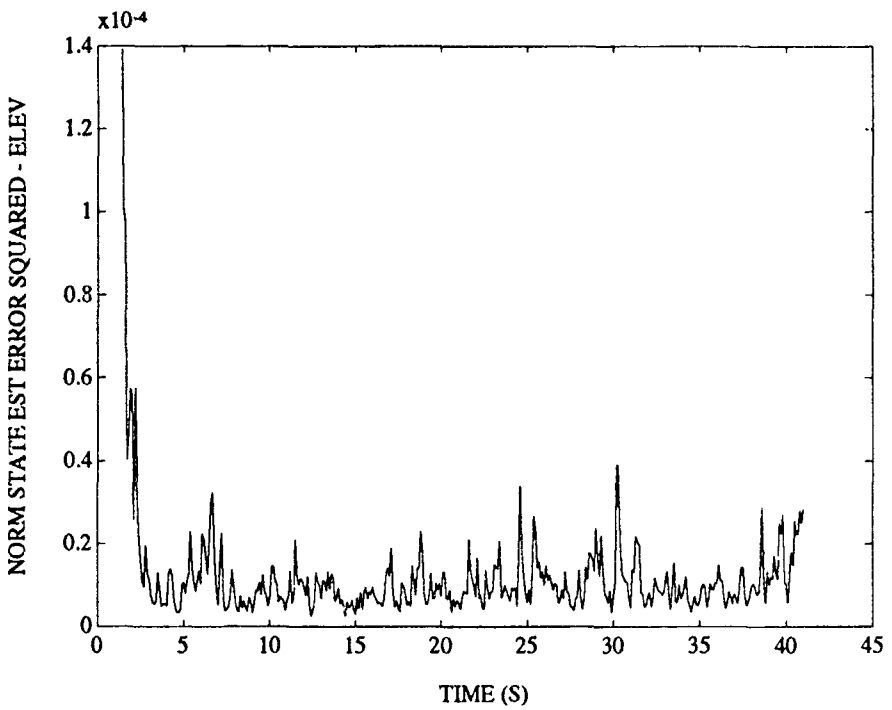

FIGURE D-28. CHI-SQUARE TEST OF ELEVATION ESTIMATION ERROR FOR 3 STATE FILTER ON CROSSING TARGET

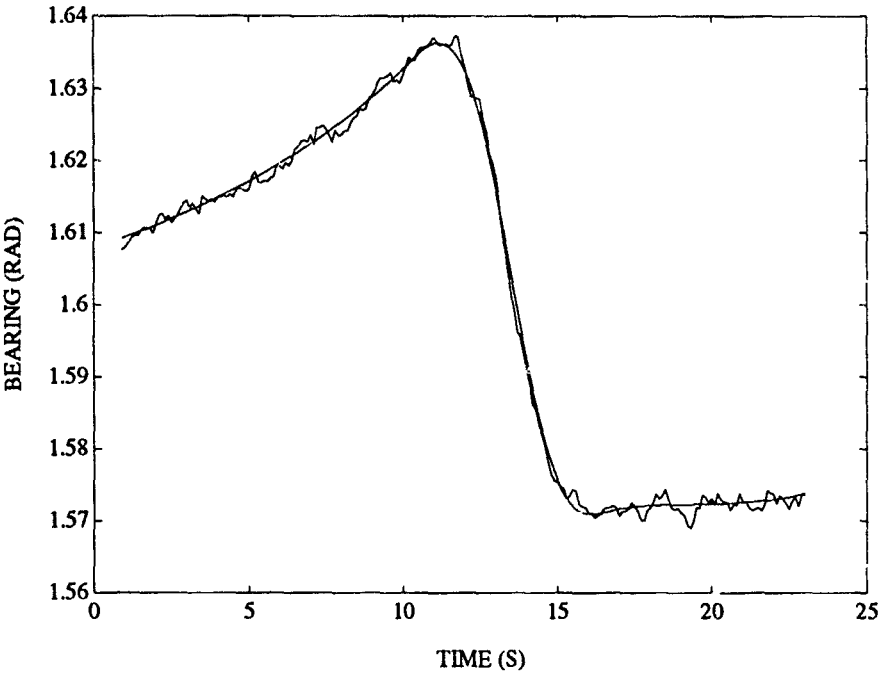

FIGURE D-29. SAMPLE BEARING ESTIMATE FOR 3 STATE FILTER ON S-TURN TARGET

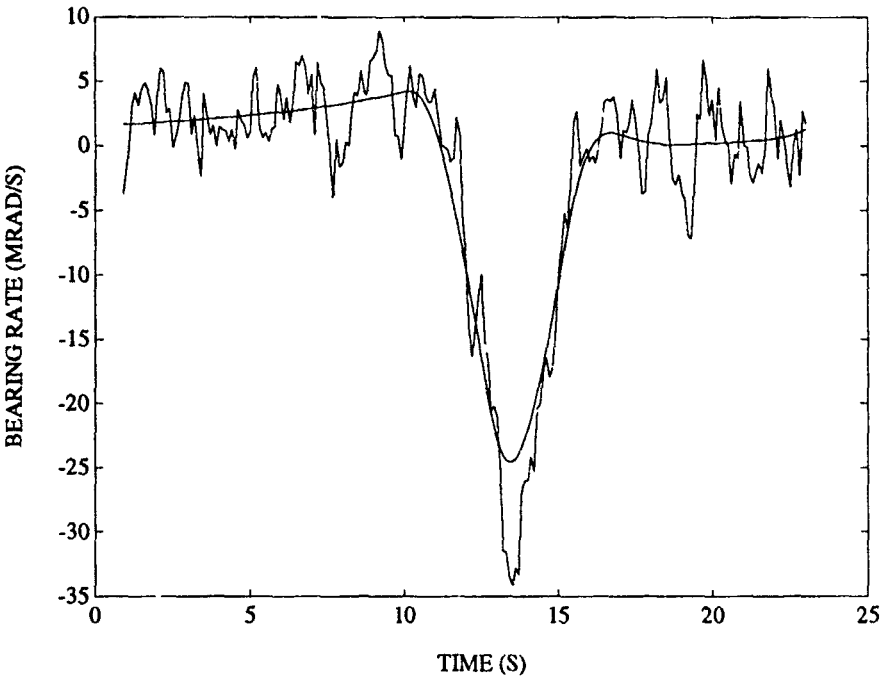

FIGURE D-30. SAMPLE BEARING RATE ESTIMATE FOR 3 STATE FILTER ON S-TURN TARGET

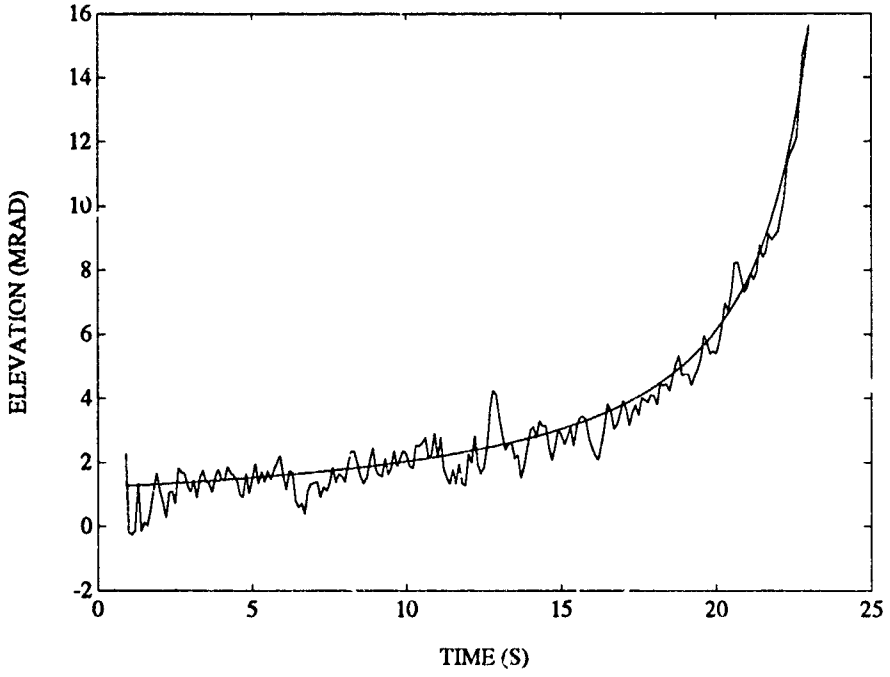

FIGURE D-31. SAMPLE ELEVATION ESTIMATE FOR 3 STATE FILTER ON S-TURN TARGET

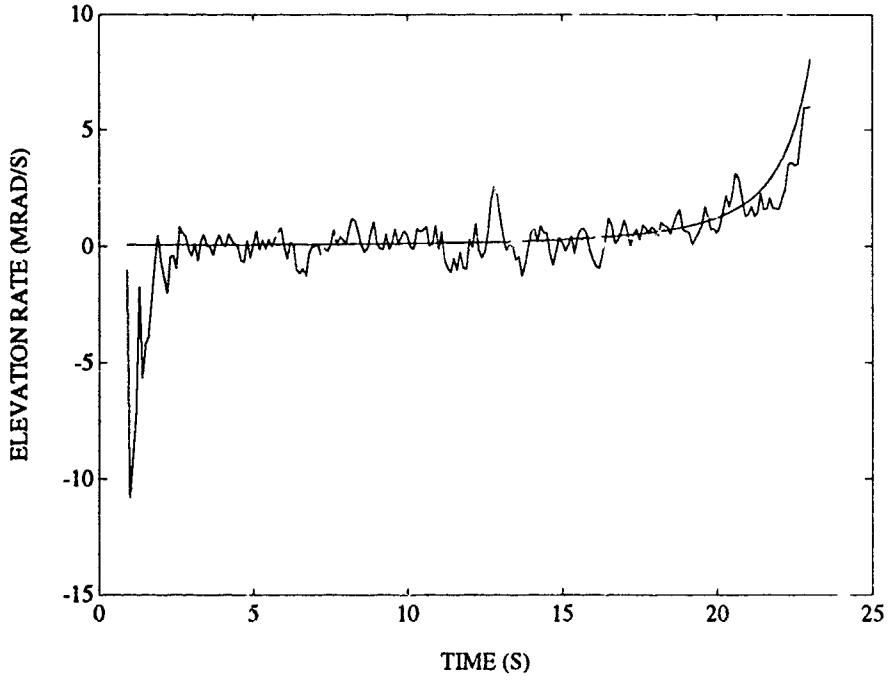

FIGURE D-32. SAMPLE ELEVATION RATE ESTIMATE FOR 3 STATE FILTER ON S-TURN TARGET

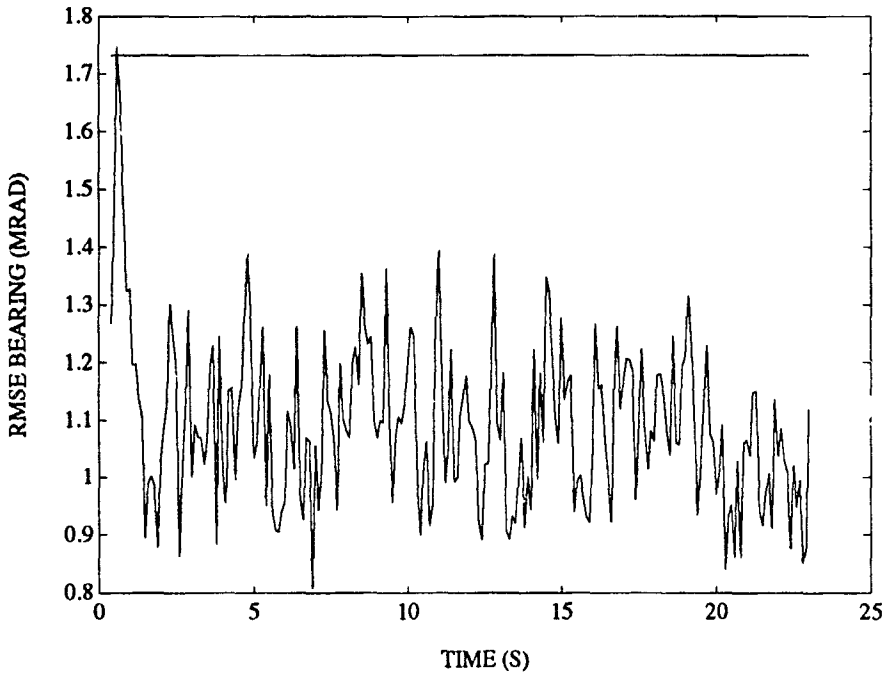

FIGURE D-33. RMS BEARING ERROR FOR 3 STATE FILTER ON S-TURN TARGET

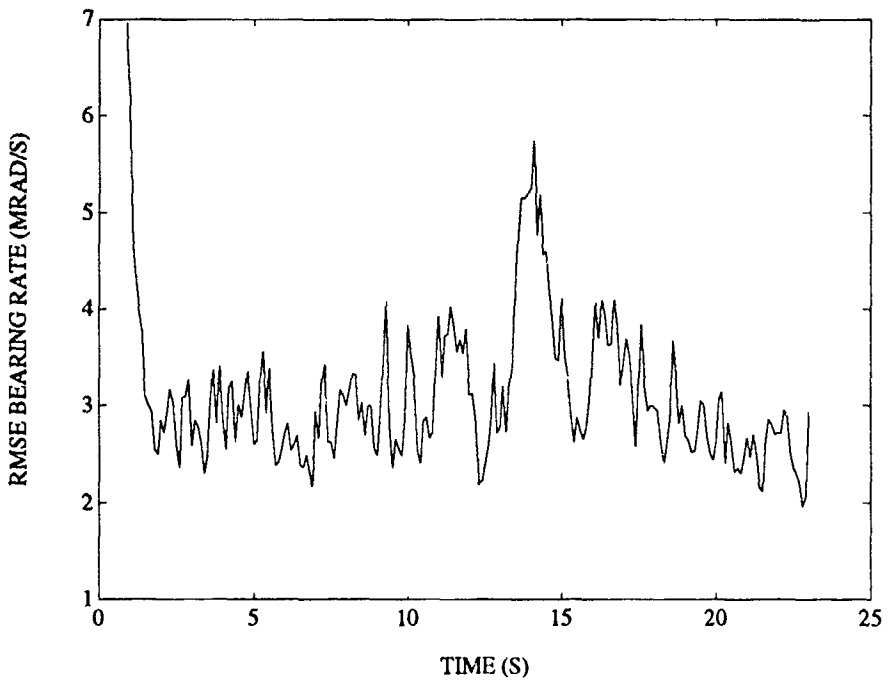

FIGURE D-34. RMS BEARING RATE ERROR FOR 3 STATE FILTER ON S-TURN TARGET

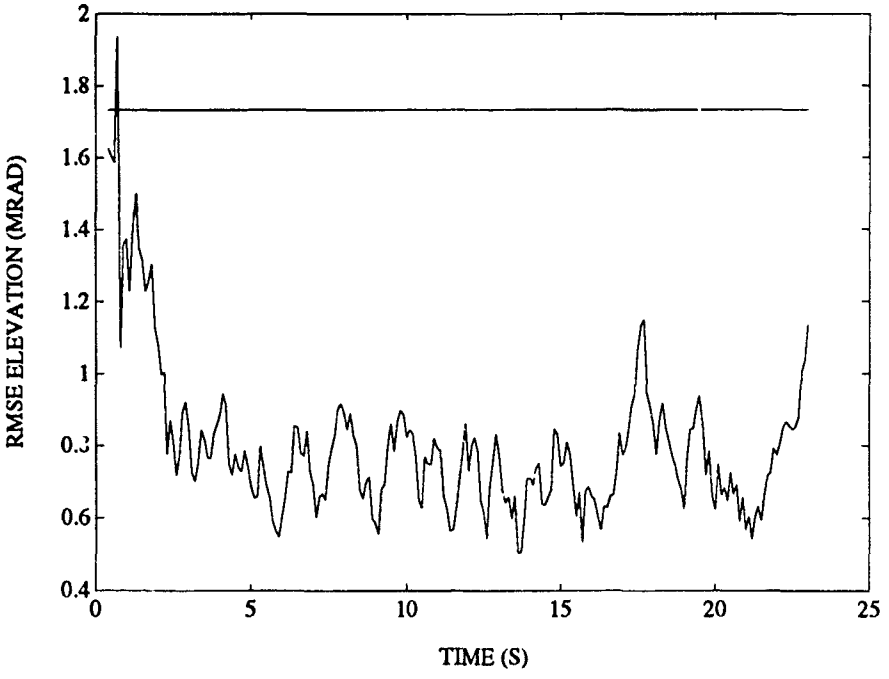

FIGURE D-35. RMS ELEVATION ERROR FOR 3 STATE FILTER ON S-TURN TARGET

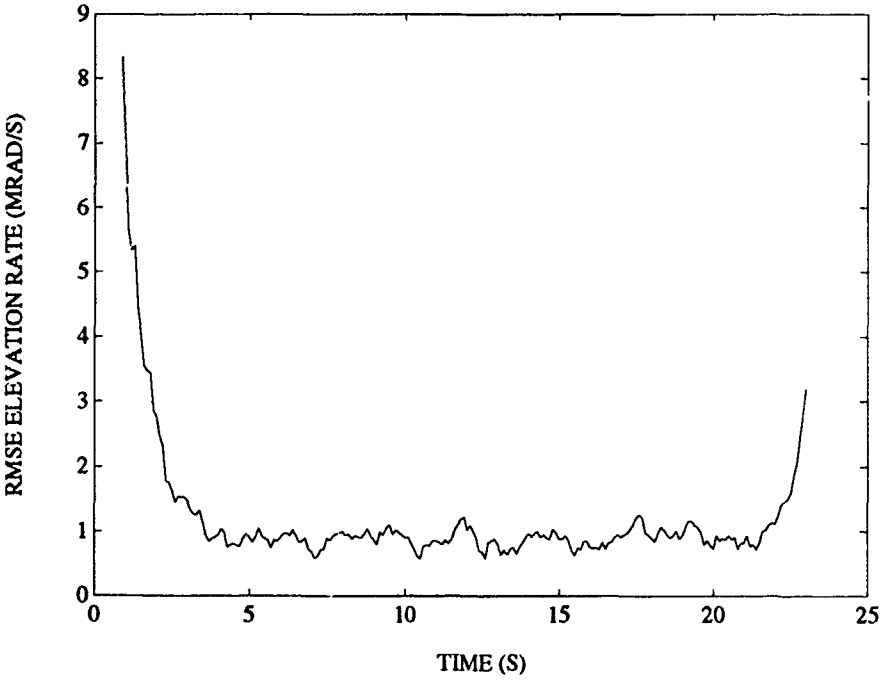

FIGURE D-36. RMS ELEVATION RATE ERROR FOR 3 STATE FILTER ON S-TURN TARGET

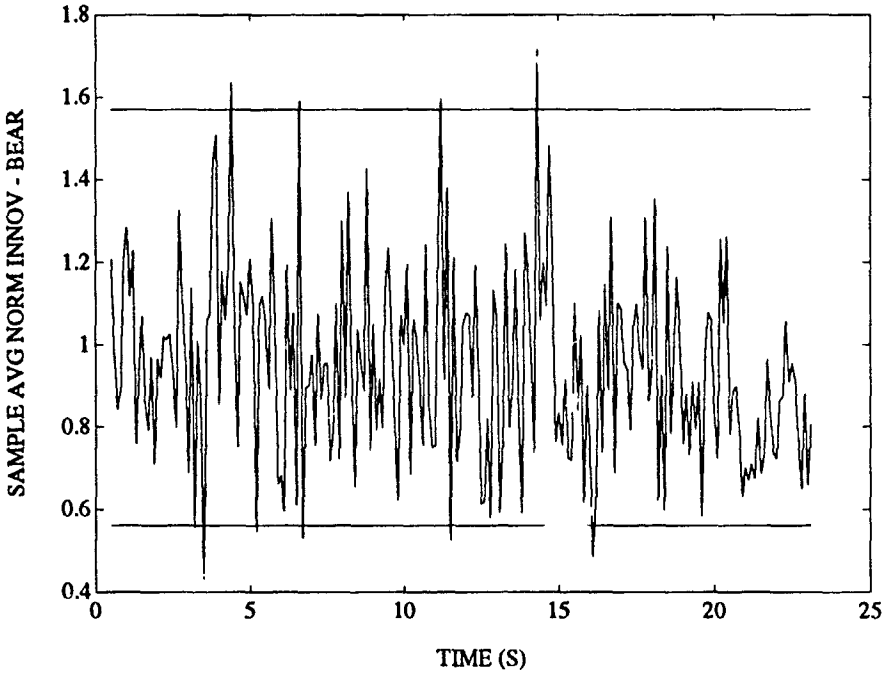

FIGURE D-37. CHI-SQUARE TEST OF BEARING INNOVATIONS FOR 3 STATE FILTER ON S-TURN TARGET

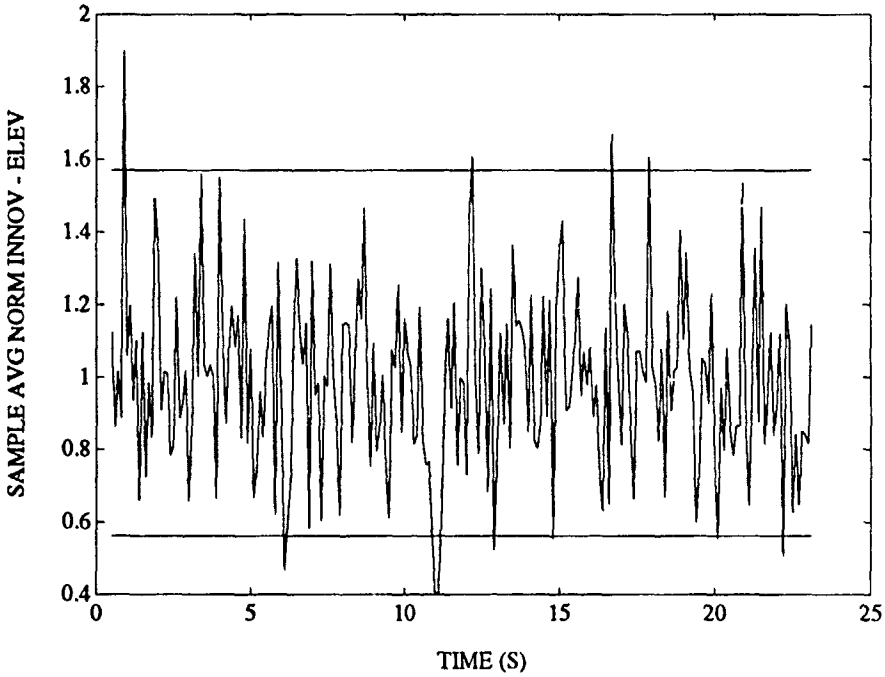

FIGURE D-38. CHI-SQUARE TEST OF ELEVATION INNOVATIONS FOR 3 STATE FILTER ON S-TURN TARGET

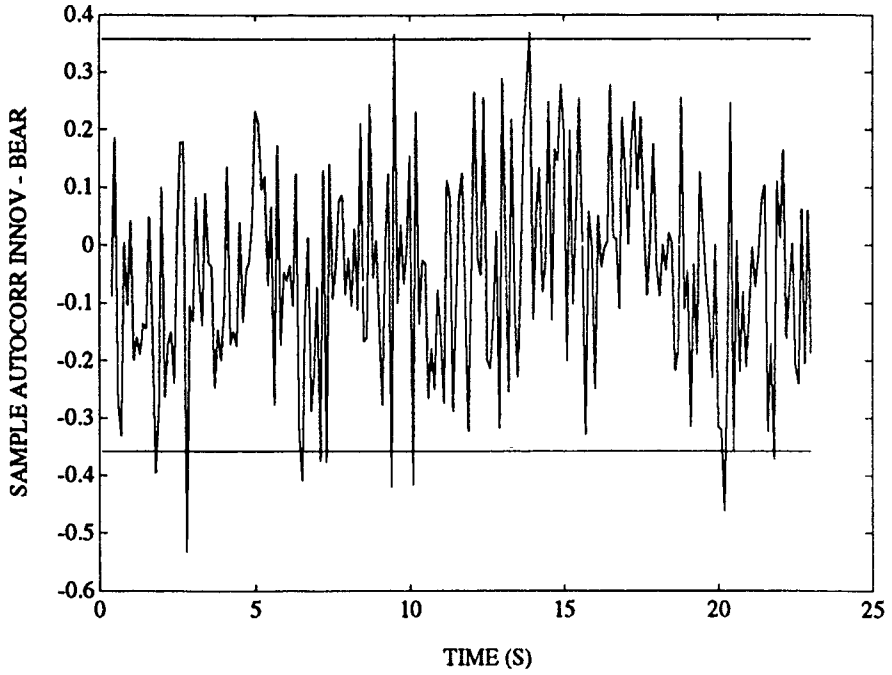

FIGURE D-39. WHITENESS TEST OF BEARING INNOVATIONS FOR 3 STATE FILTER ON S-TURN TARGET

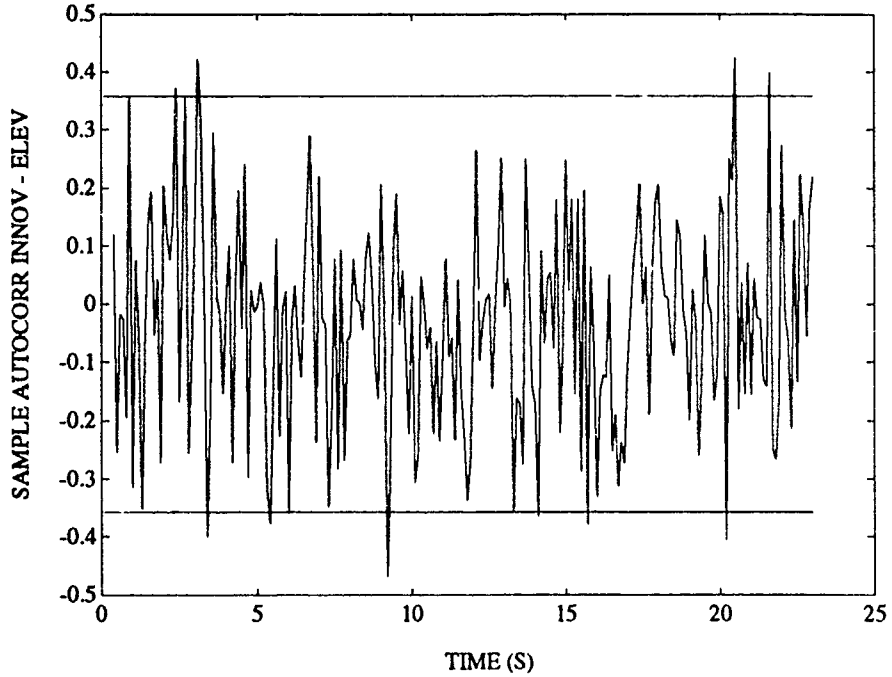

FIGURE D-40. WHITENESS TEST OF ELEVATION INNOVATIONS FOR 3 STATE FILTER ON S-TURN TARGET

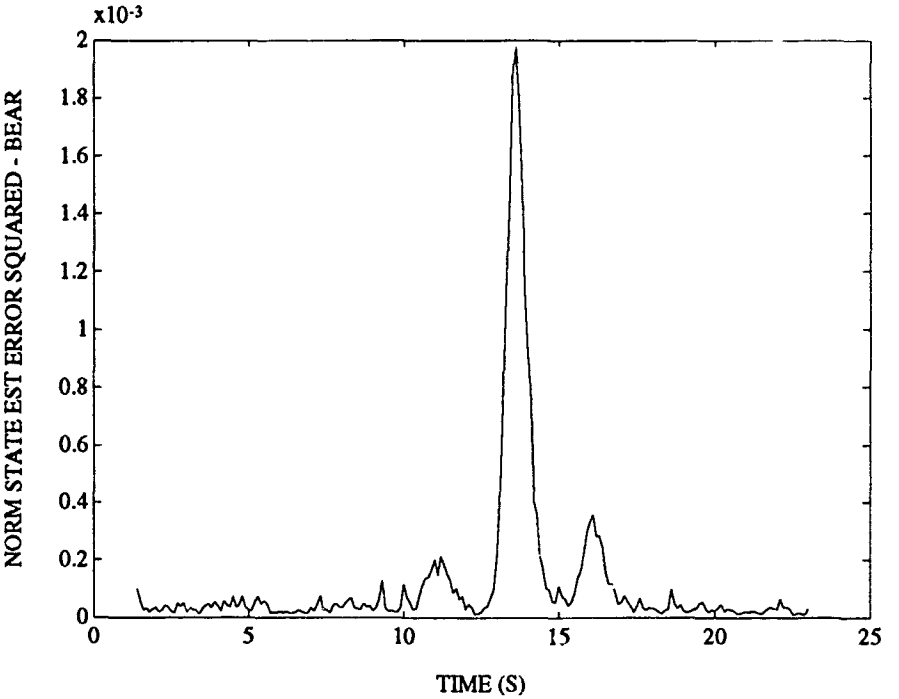

FIGURE D-41. CHI-SQUARE TEST OF BEARING ESTIMATION ERROR FOR 3 STATE FILTER ON S-TURN TARGET

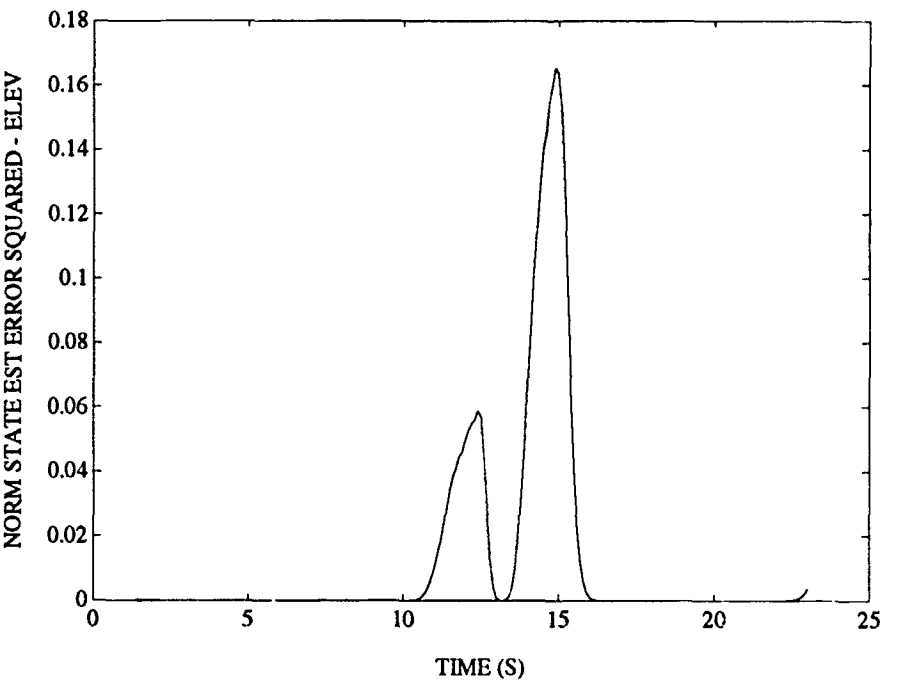

FIGURE D-42. CHI-SQUARE TEST OF ELEVATION ESTIMATION ERROR FOR 3 STATE FILTER ON S-TURN TARGET

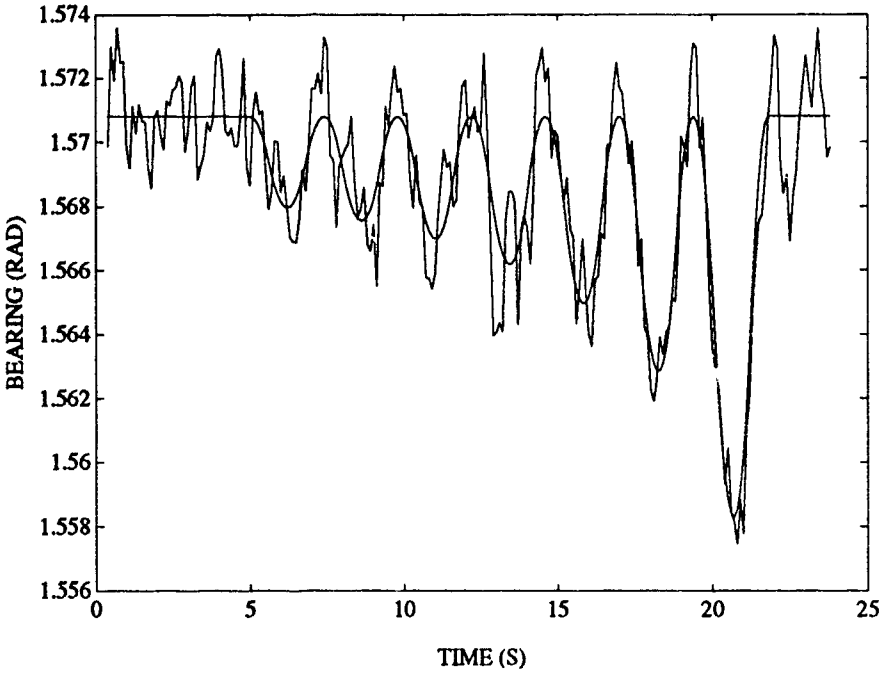

FIGURE D-43. SAMPLE BEARING ESTIMATE FOR 3 STATE FILTER ON JINKING TARGET

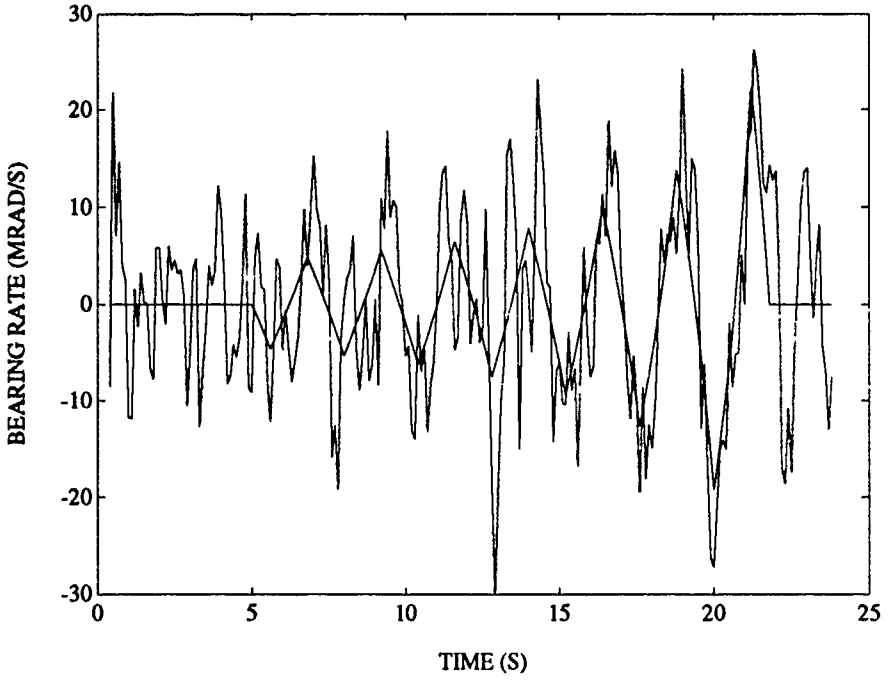

FIGURE D-44. SAMPLE BEARING RATE ESTIMATE FOR 3 STATE FILTER ON JINKING TARGET

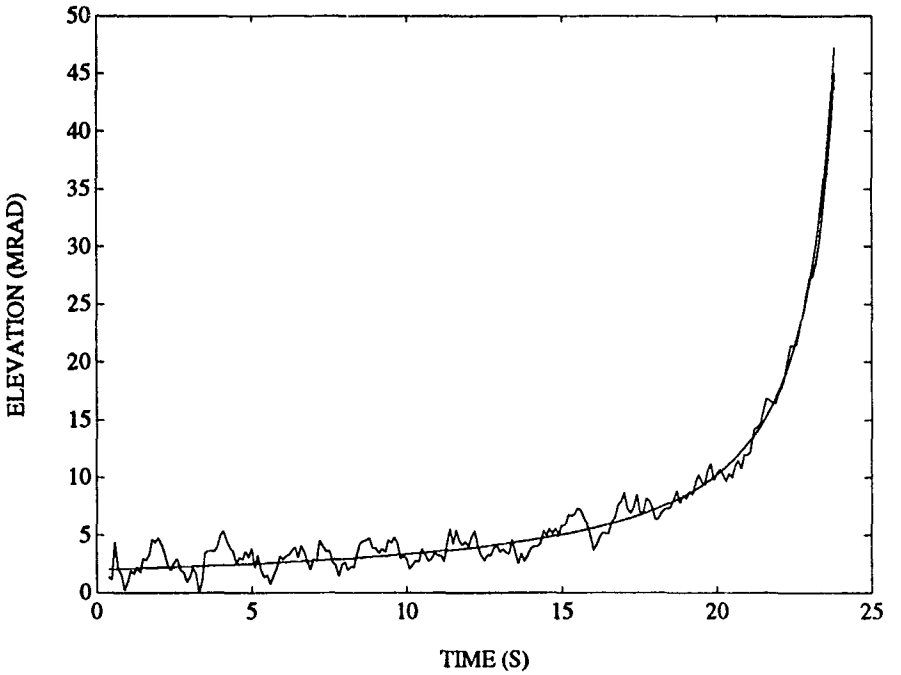

FIGURE D-45. SAMPLE ELEVATION ESTIMATE FOR 3 STATE FILTER ON JINKING TARGET

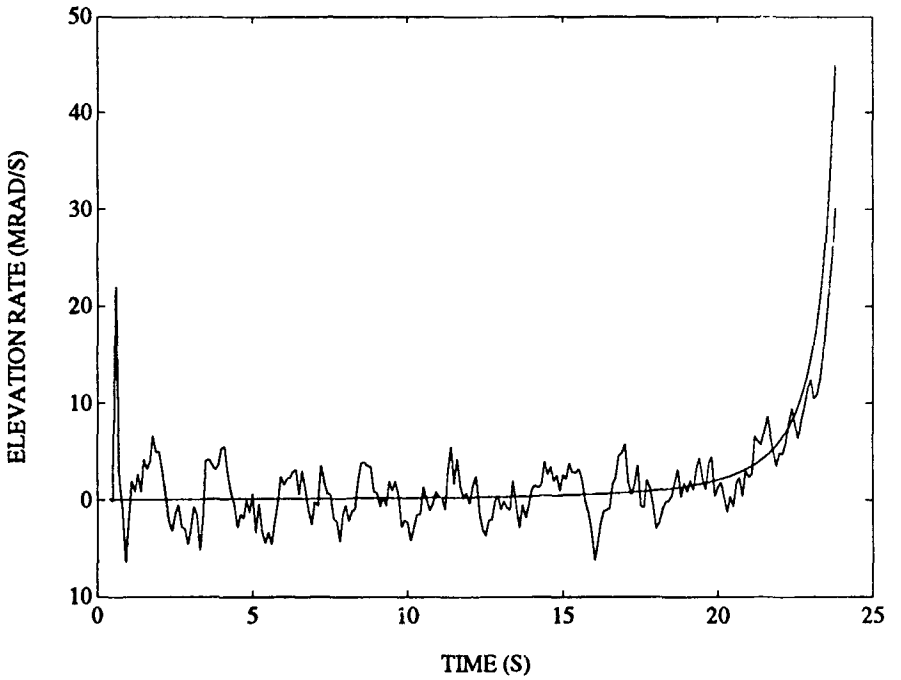

FIGURE D-46. SAMPLE ELEVATION RATE ESTIMATE FOR 3 STATE FILTER ON JINKING TARGET

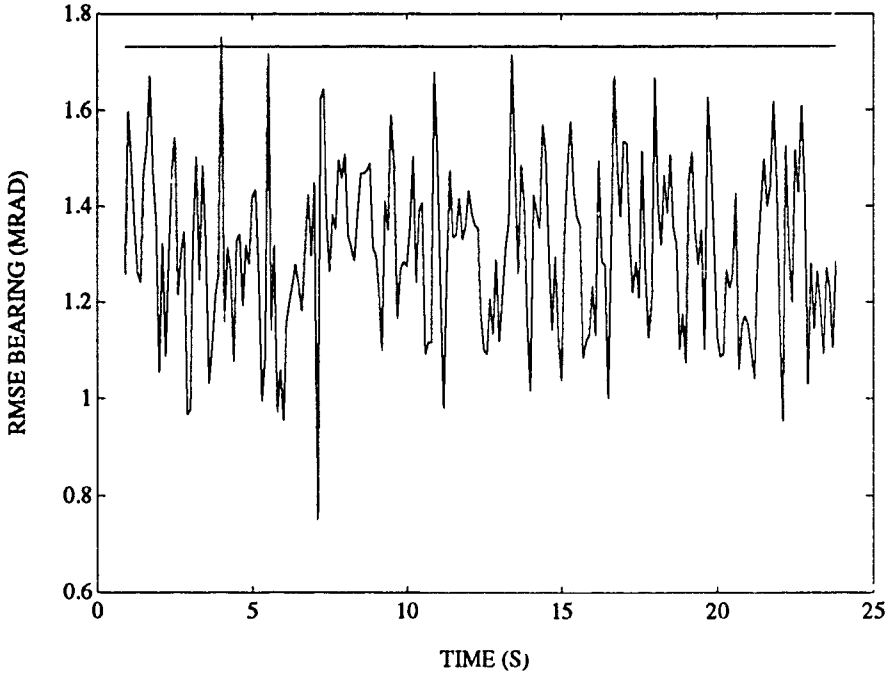

FIGURE D-47. RMS BEARING ERROR FOR 3 STATE FILTER ON JINKING TARGET

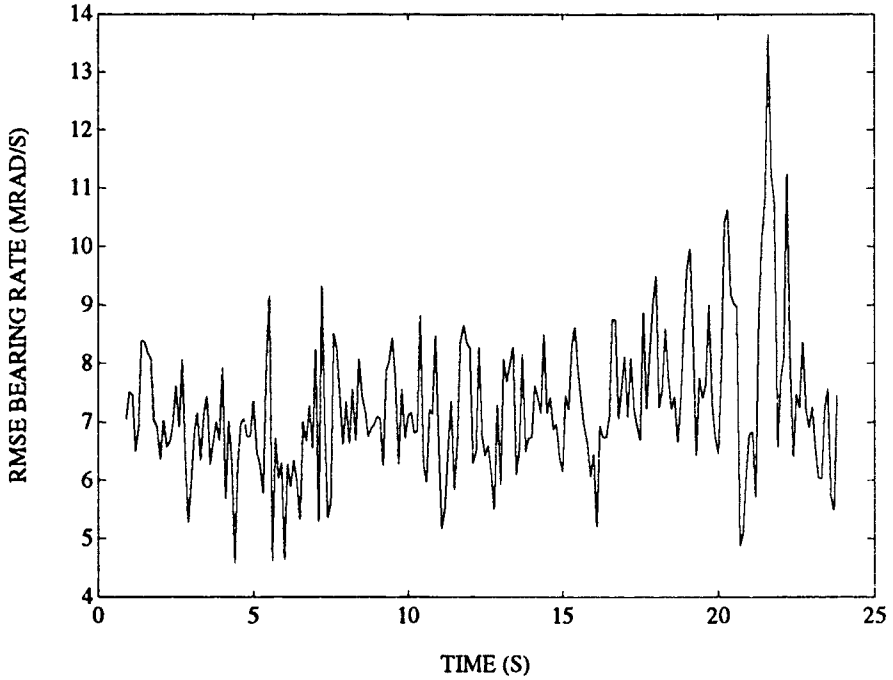

FIGURE D-48. RMS BEARING RATE ERROR FOR 3 STATE FILTER ON JINKING TARGET

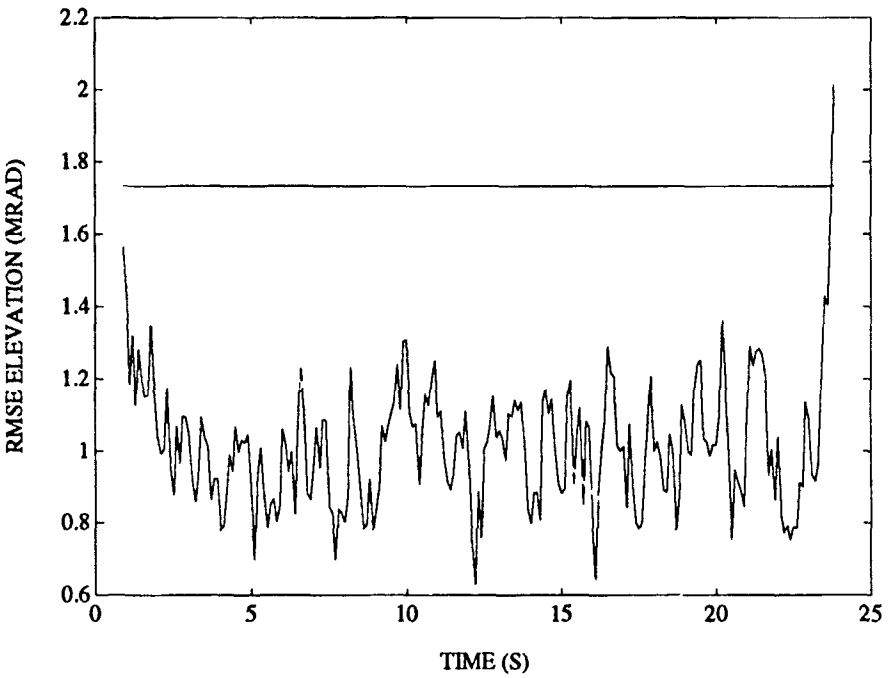

FIGURE D-49. RMS ELEVATION ERROR FOR 3 STATE FILTER ON JINKING TARGET

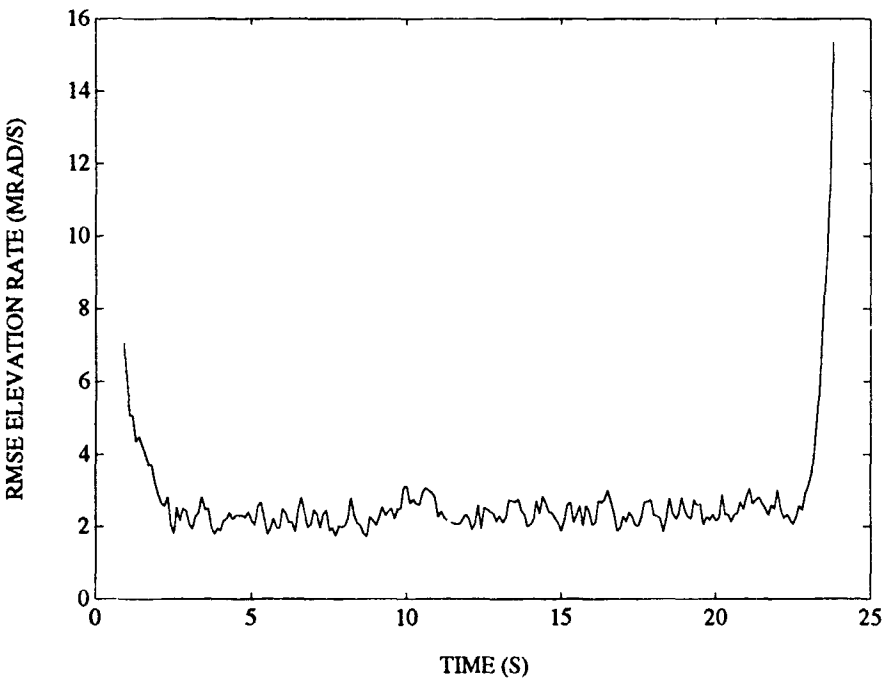

FIGURE D-50. RMS ELEVATION RATE ERROR FOR 3 STATE FILTER ON JINKING TARGET

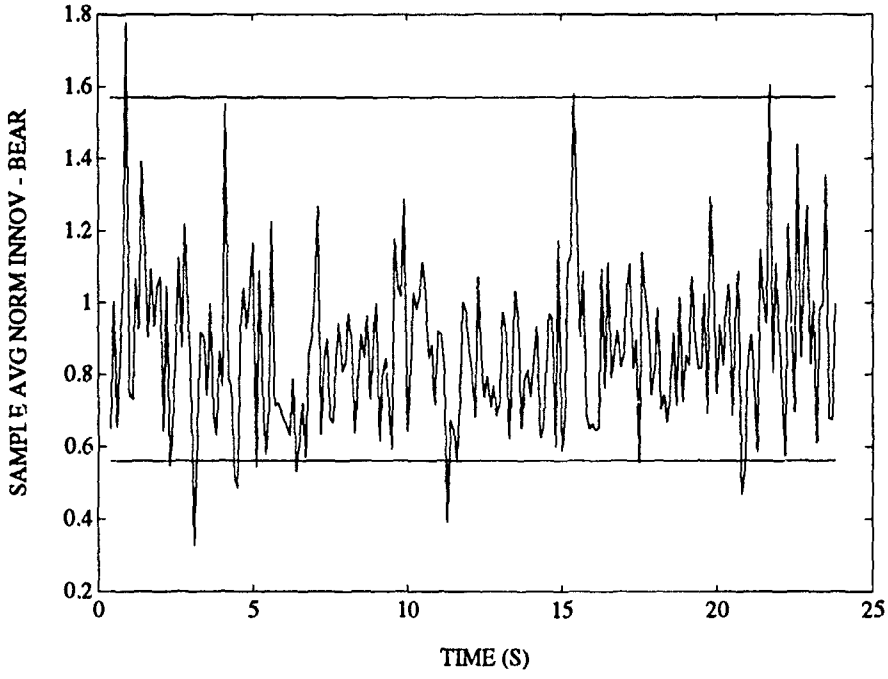

FIGURE D-51. CHI-SQUARE TEST OF BEARING INNOVATIONS FOR 3 STATE FILTER ON JINKING TARGET

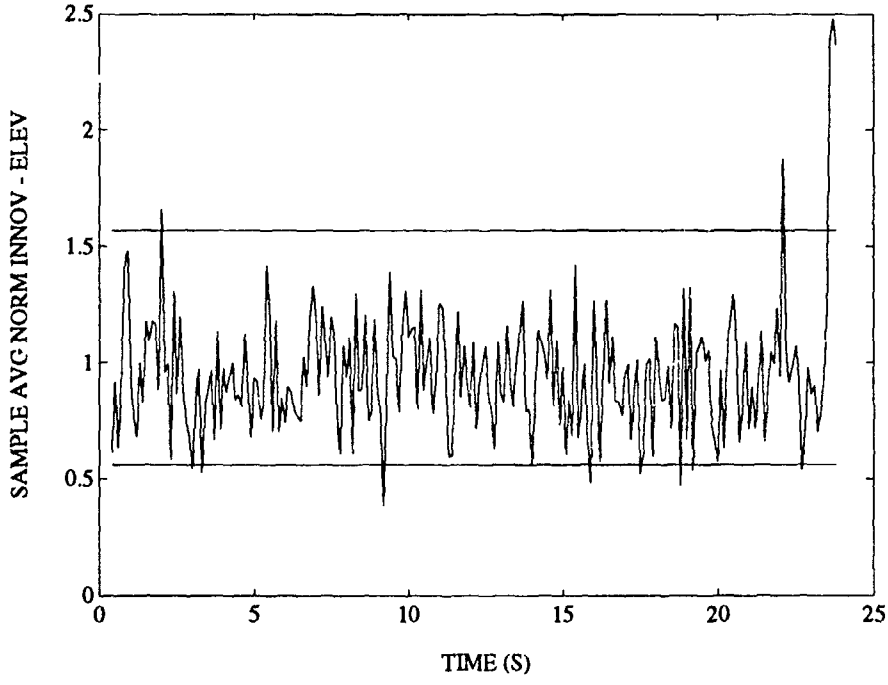

FIGURE D-52. CHI-SQUARE TEST OF ELEVATION INNOVATIONS FOR 3 STATE FILTER ON JINKING TARGET

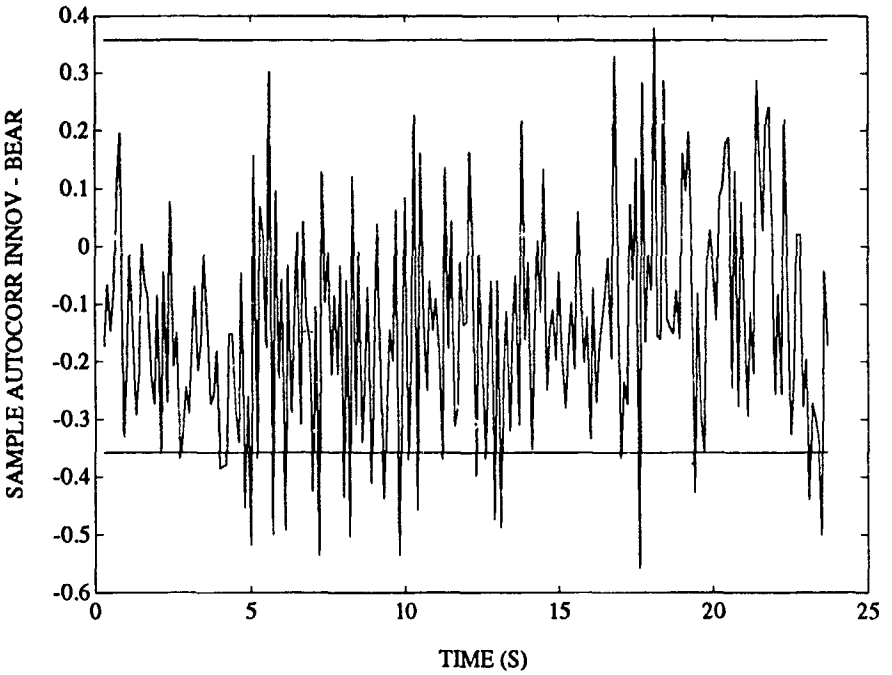

FIGURE D-53. WHITENESS TEST OF BEARING INNOVATIONS FOR 3 STATE FILTER ON JINKING TARGET

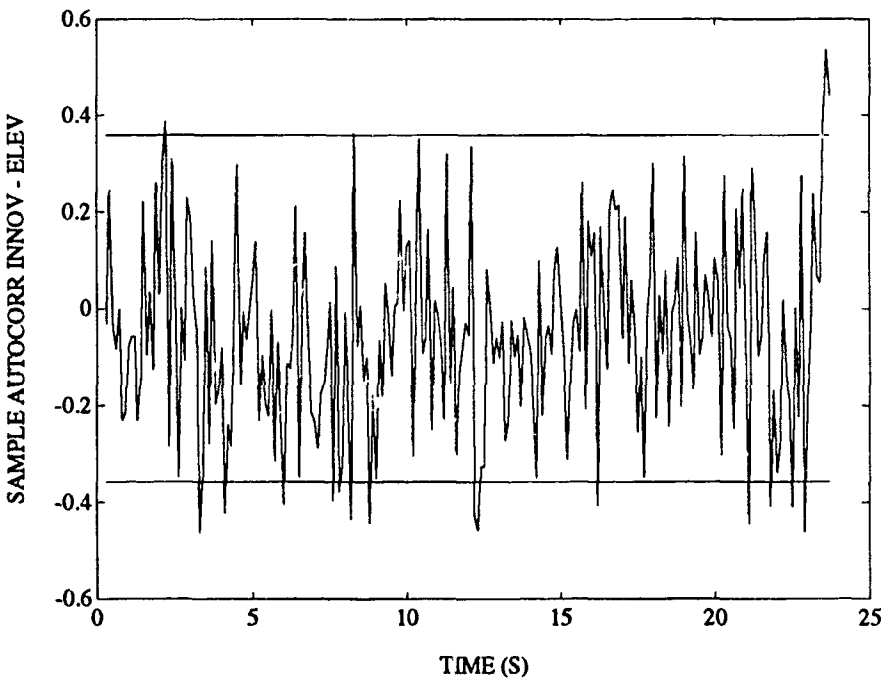

FIGURE D-54. WHITENESS TEST OF ELEVATION INNOVATIONS FOR 3 STATE FILTER ON JINKING TARGET

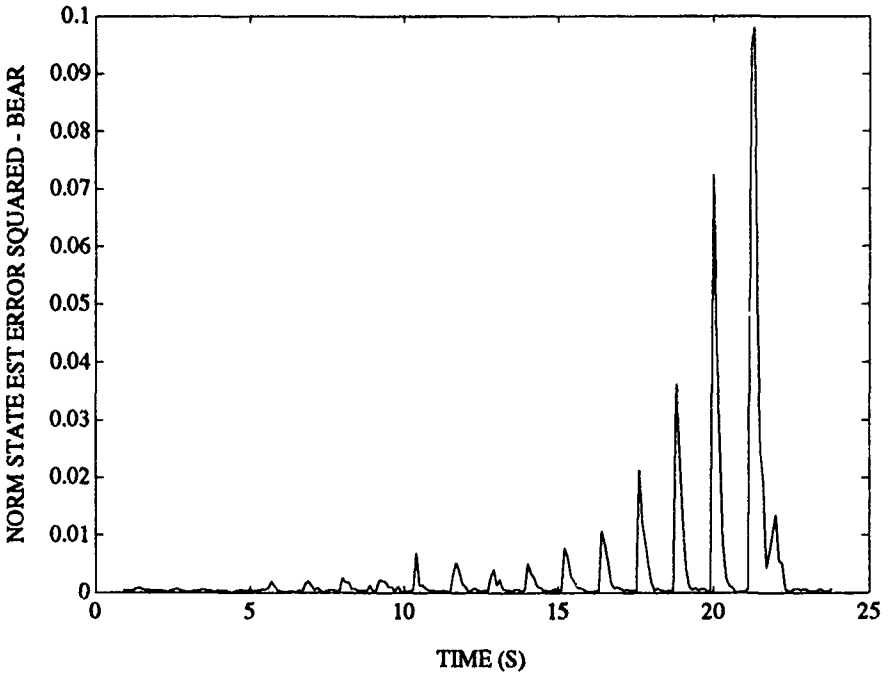

FIGURE D-55. CHI-SQUARE TEST OF BEARING ESTIMATION ERROR FOR 3 STATE FILTER ON JINKING TARGET

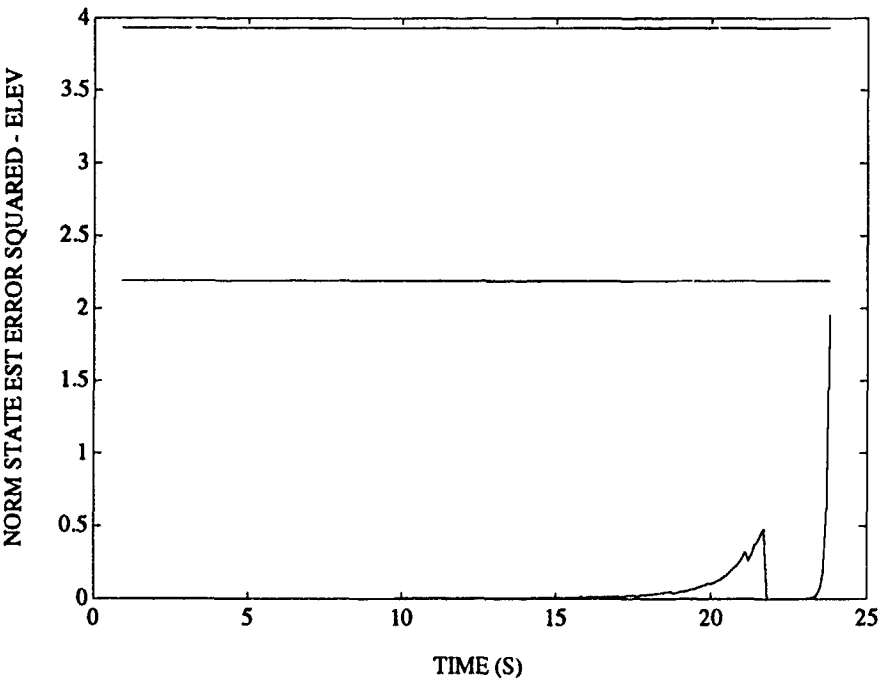

FIGURE D-56. CHI-SQUARE TEST OF ELEVATION ESTIMATION ERROR FOR 3 STATE FILTER ON JINKING TARGET

APPENDIX E
PLOTS OF COMPARISON OF 2 AND 3 STATE FILTERS

This appendix presents the results of simulations performed to compare the performance of the 2 and 3 state filters. The results are presented in the following order: radial target, crossing target, S-turn target, and jinking target.

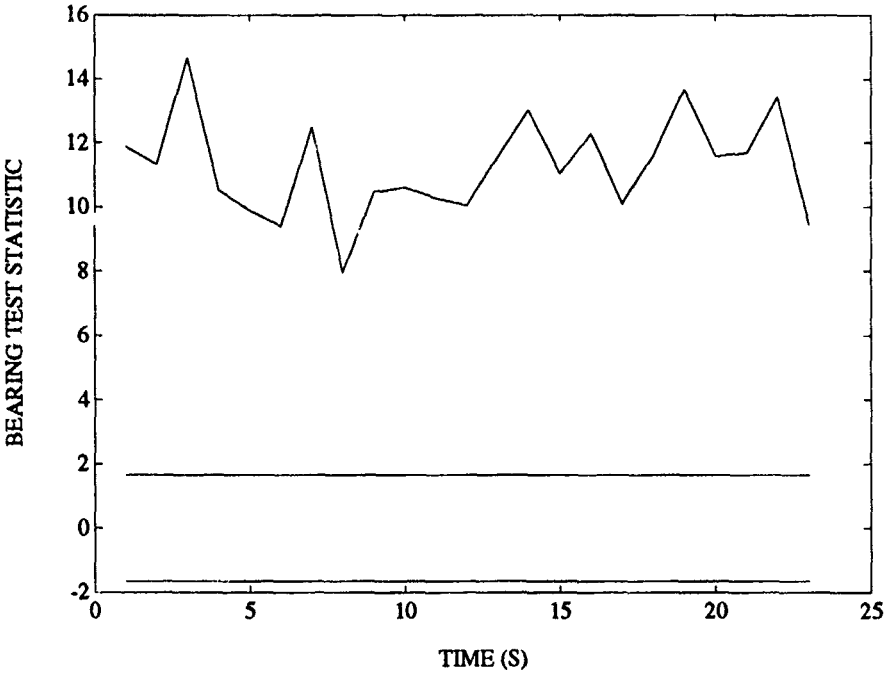

FIGURE E-1. COMPARISON OF BEARING ESTIMATES FROM 2 AND 3 STATE FILTERS ON RADIAL TARGET

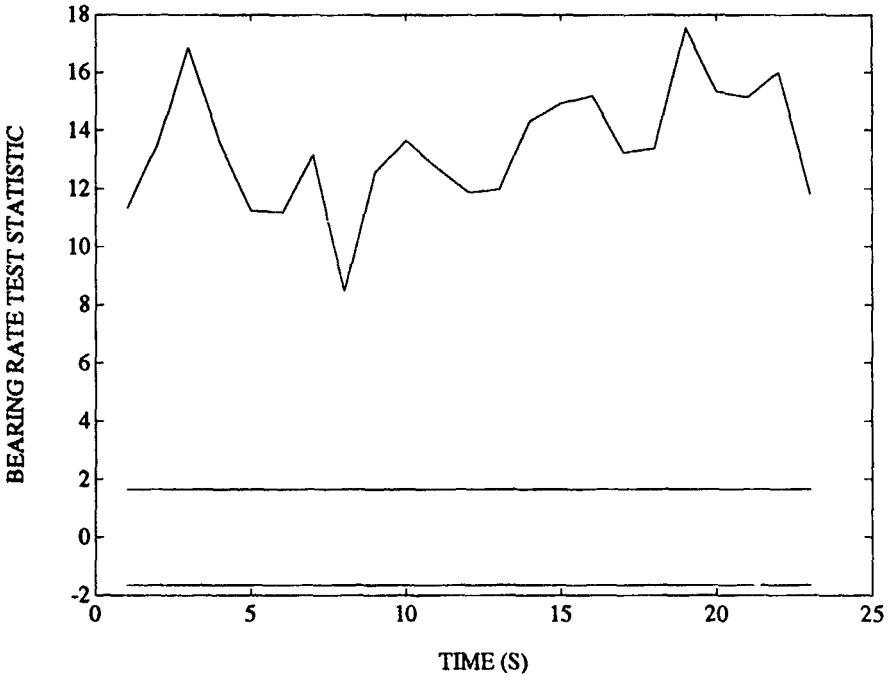

FIGURE E-2. COMPARISON OF BEARING RATE ESTIMATES FROM 2 AND 3 STATE FILTERS ON RADIAL TARGET

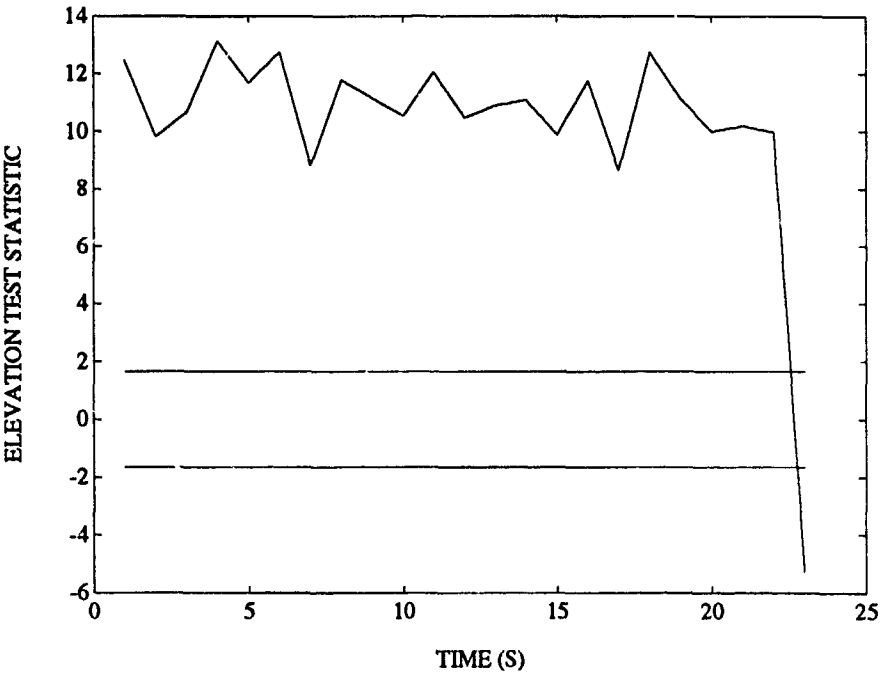

FIGURE E-3. COMPARISON OF ELEVATION ESTIMATES FROM 2 AND 3 STATE FILTERS ON RADIAL TARGET

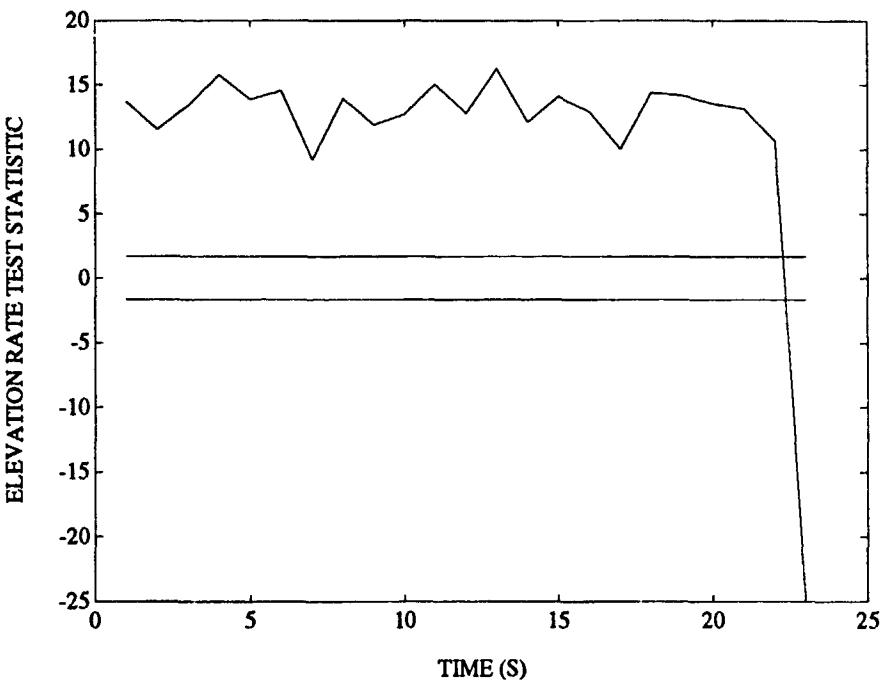

FIGURE E-4. COMPARISON OF ELEVATION RATE ESTIMATES FROM 2 AND 3 STATE FILTERS ON RADIAL TARGET

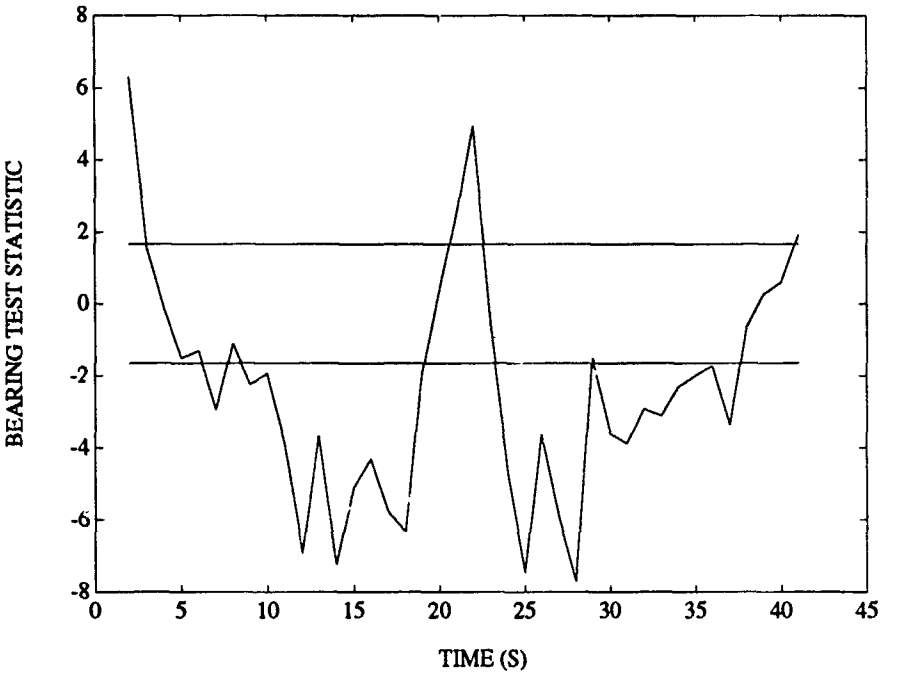

FIGURE E-5. COMPARISON OF BEARING ESTIMATES FROM 2 AND 3 STATE FILTERS ON CROSSING TARGET

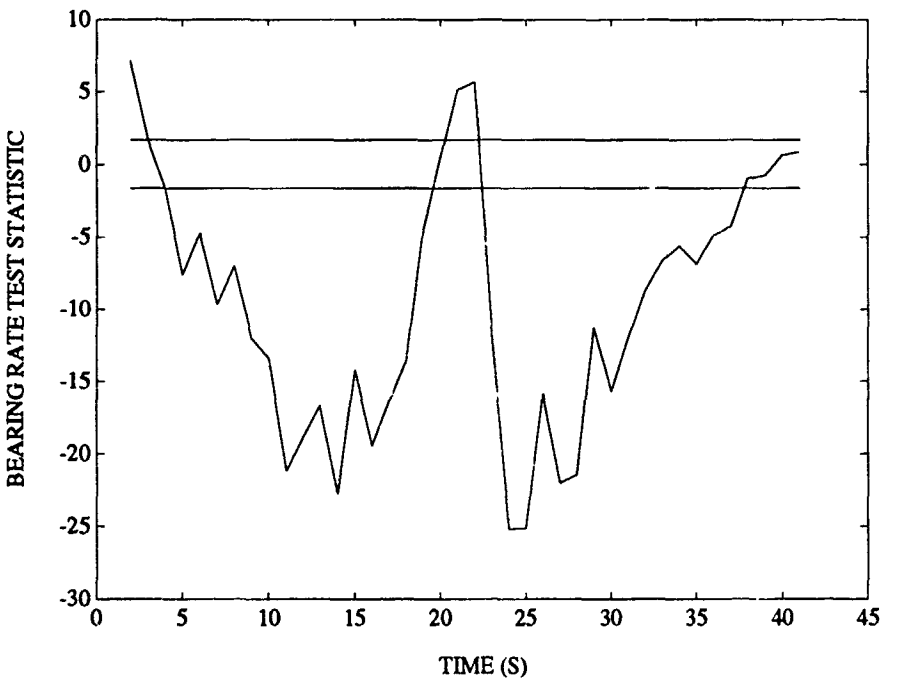

FIGURE E-6. COMPARISON OF BEARING RATE ESTIMATES FROM 2 AND 3 STATE FILTERS ON CROSSING TARGET

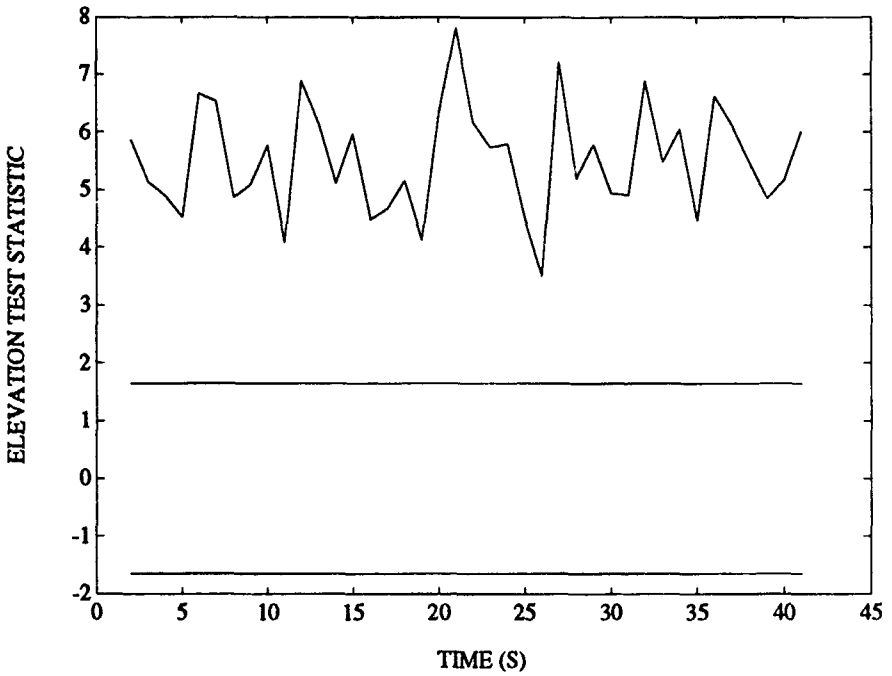

FIGURE E-7. COMPARISON OF ELEVATION ESTIMATES FROM 2 AND 3 STATE FILTERS ON CROSSING TARGET

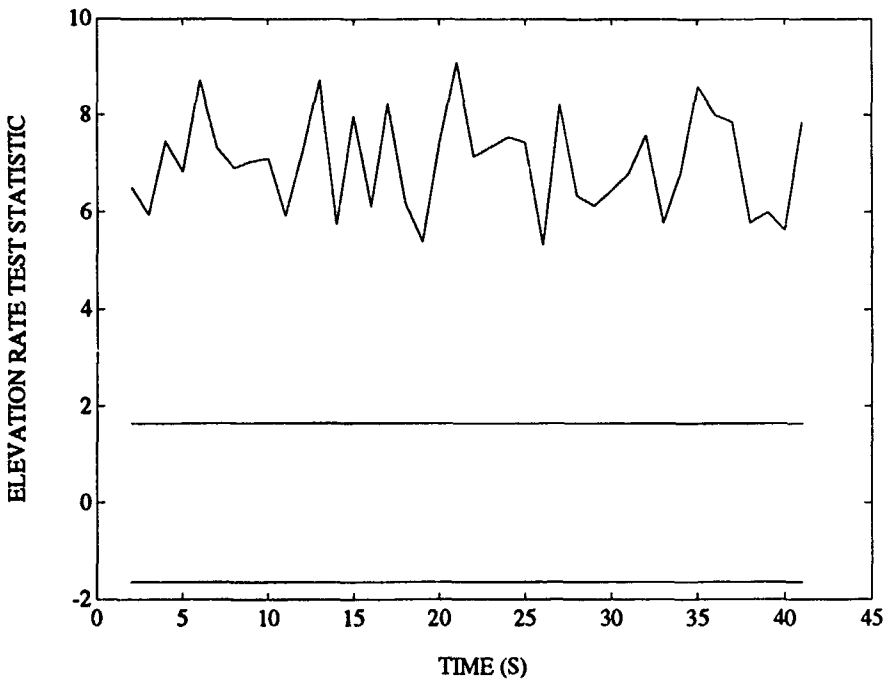

FIGURE E-8. COMPARISON OF ELEVATION RATE ESTIMATES FROM 2 AND 3 STATE FILTERS ON CROSSING TARGET

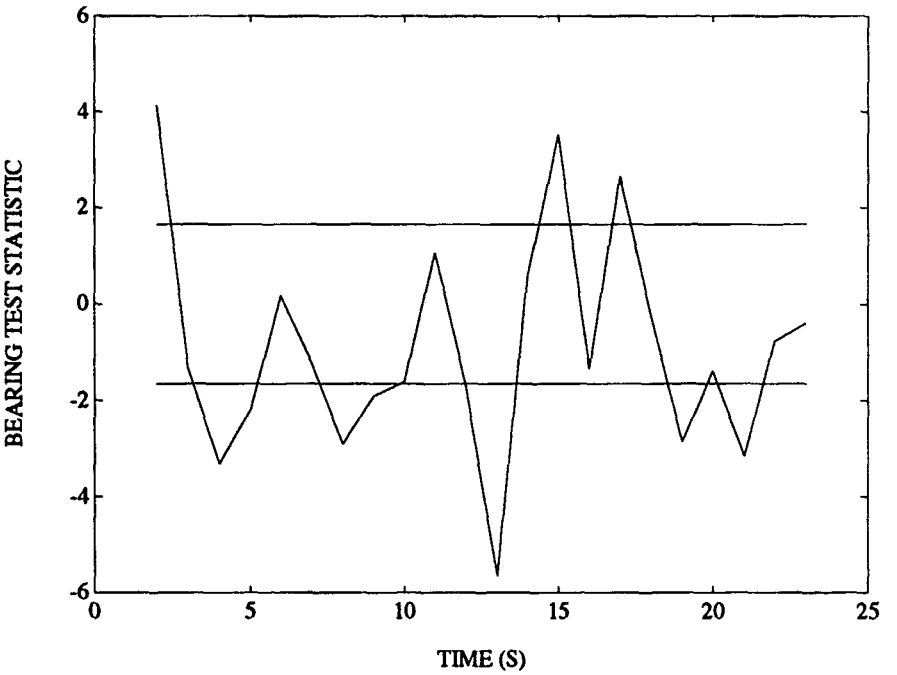

FIGURE E-9. COMPARISON OF BEARING ESTIMATES FROM 2 AND 3 STATE FILTERS ON S-TURN TARGET

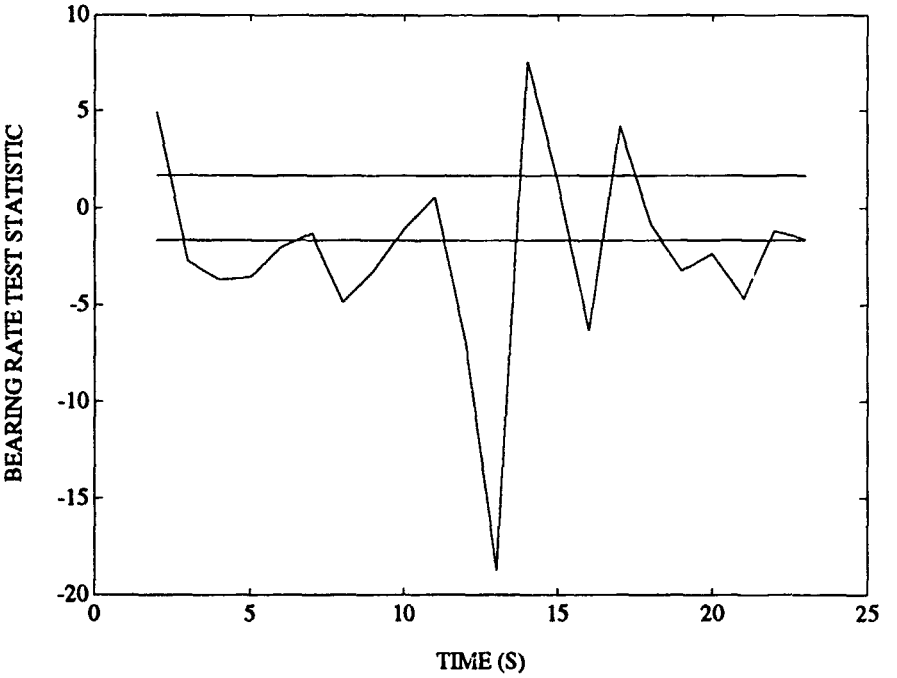

FIGURE E-10. COMPARISON OF BEARING RATE ESTIMATES FROM 2 AND 3 STATE FILTERS ON S-TURN TARGET

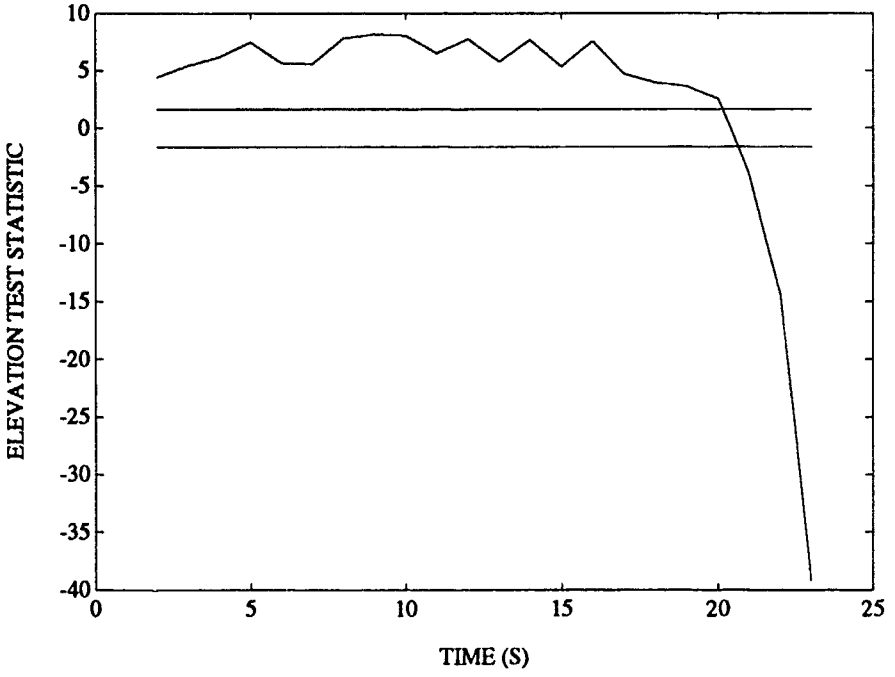

FIGURE E-11. COMPARISON OF ELEVATION ESTIMATES FROM 2 AND 3 STATE FILTERS ON S-TURN TARGET

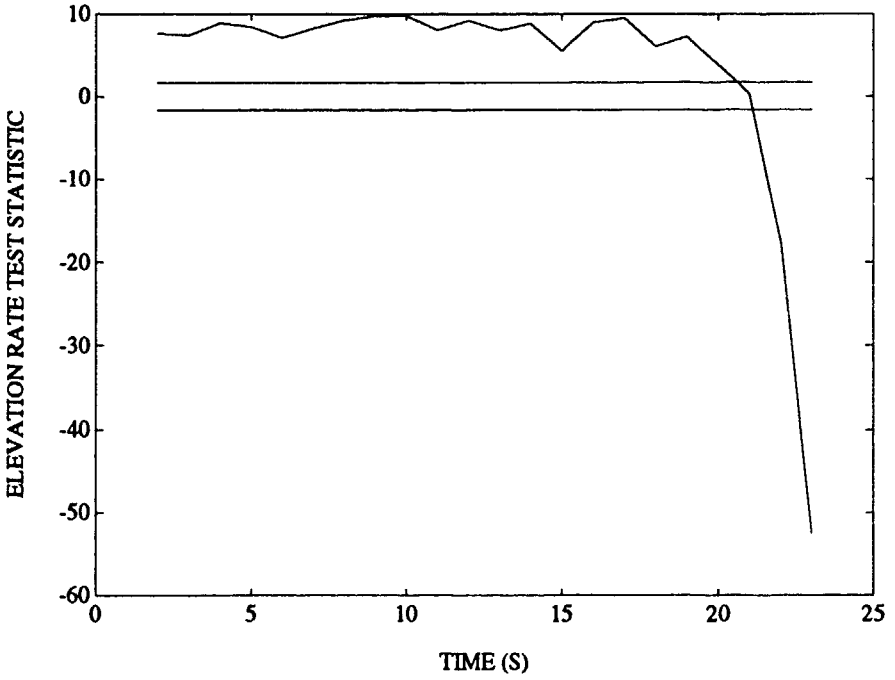

FIGURE E-12. COMPARISON OF ELEVATION RATE ESTIMATES FROM 2 AND 3 STATE FILTERS ON S-TURN TARGET

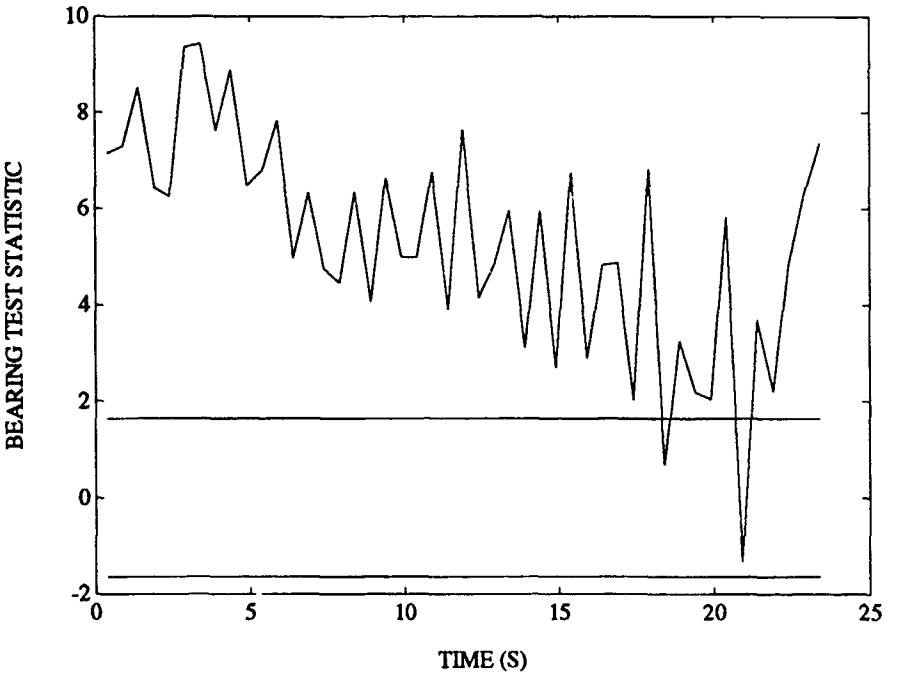

FIGURE E-13. COMPARISON OF BEARING ESTIMATES FROM 2 AND 3 STATE FILTERS ON JINKING TARGET

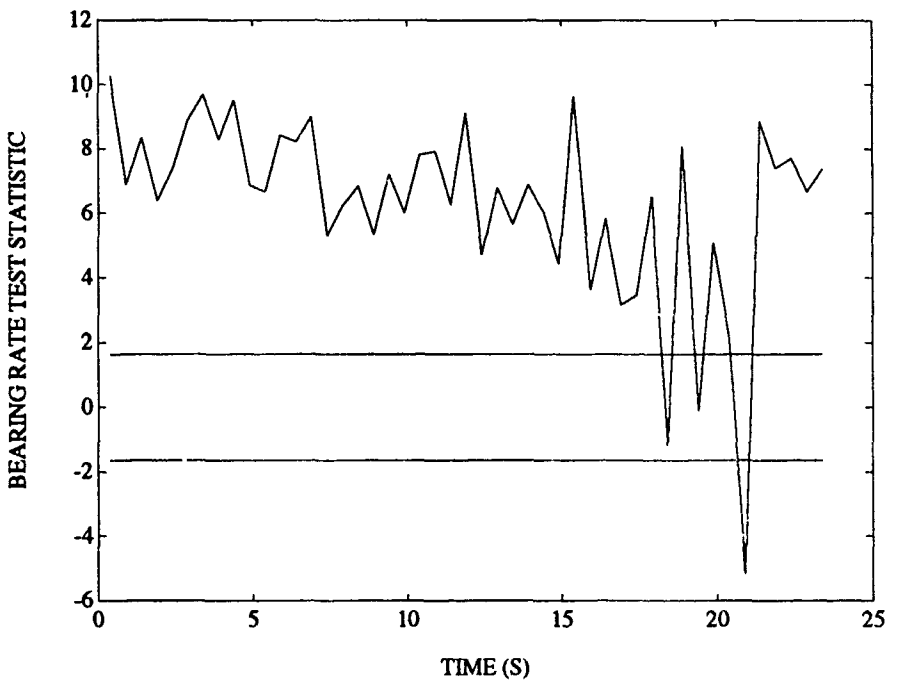

FIGURE E-14. COMPARISON OF BEARING RATE ESTIMATES FROM 2 AND 3 STATE FILTERS ON JINKING TARGET

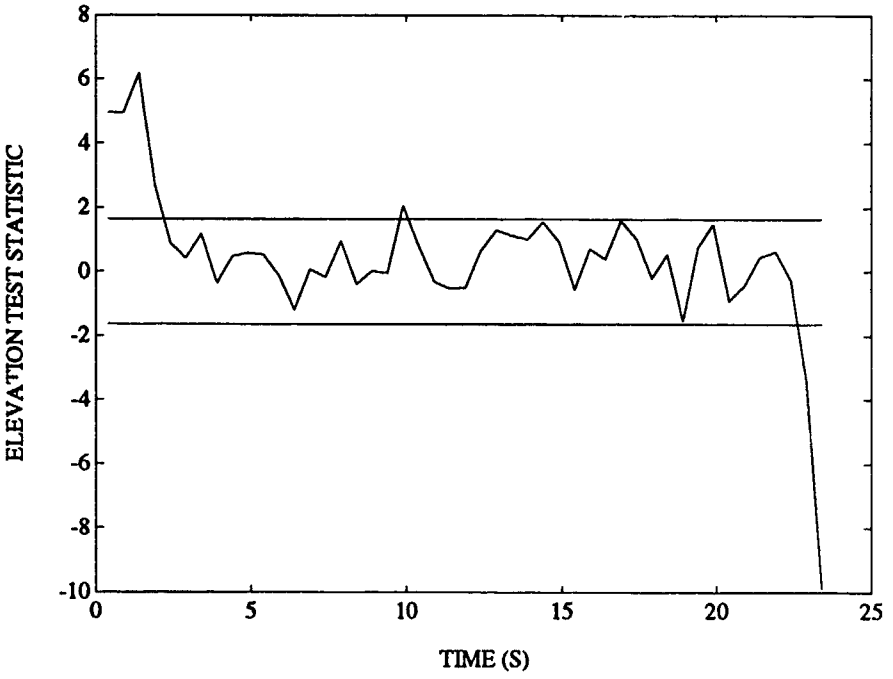

FIGURE E-15. COMPARISON OF ELEVATION ESTIMATES FROM 2 AND STATE FILTERS ON JINKING TARGET

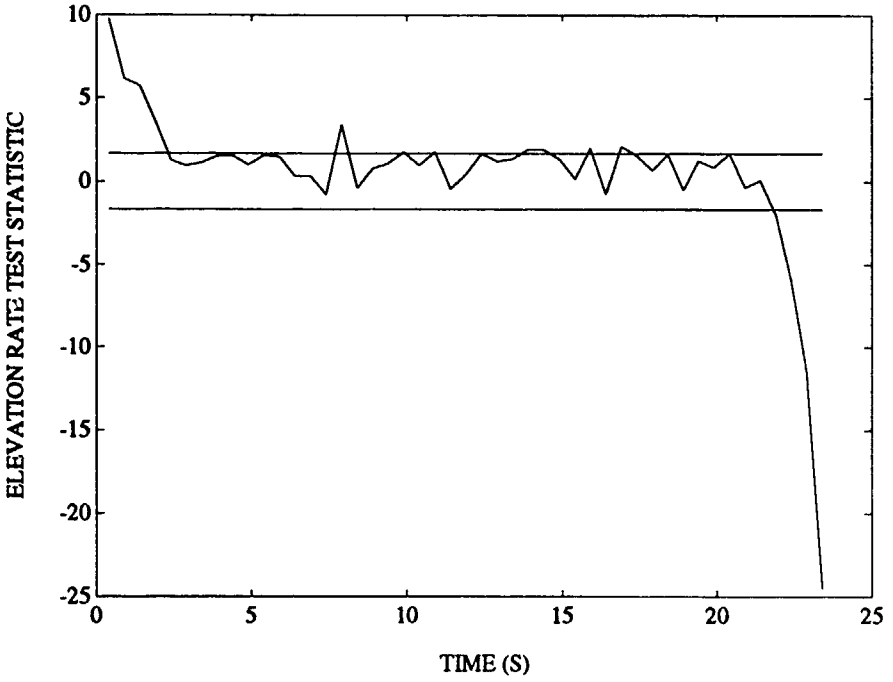

FIGURE E-16. COMPARISON OF ELEVATION RATE ESTIMATES FROM 2 AND 3 STATE FILTERS ON JINKING TARGET

DISTRIBUTION

	Copies
DEFENSE TECHNICAL INFORMATION CENTER CAMERON STATION ALEXANDRIA, VA 22304-6145	2
ATTN TECHNICAL LIBRARY ONT-0215 CDR WALLACE DIRECTOR OFFICE OF NAVAL TECHNOLOGY 800 N QUINCY ST ARLINGTON, VA 22217-5000	1
ATTN DIRECTOR OF RESEARCH US NAVAL ACADEMY ANNAPOLIS, MD 21402	1
ATTN TECHNICAL LIBRARY JOHN HOPKINS UNIVERSITY APPLIED PHYSICS LABORATORY 1100C JOHNS HOPKINS RD LAUREL, MD 20707	1
ATTN TECHNICAL LIBRARY SUPERINTENDENT NAVAL POST GRADUATE SCHOOL MONTEREY, CA 93940	1
ATTN CODE 804 COMMANDING OFFICER NAVAL WEAPONS SUPPORT CENTER CRANE, IN 47522-5030	1
ATTN CODE 7500 COMMANDING OFFICER NAVAL OCEAN SYSTEMS CENTER SAN DIEGO, CA 02152	1

	Copies
ATTN CODE 06D21 CODE 06D23 CODE 06D24 PMS 400B COMMANDER NAVAL SEA SYSTEMS COMMAND NAVAL SEA SYSTEMS COMMAND HEADQUARTERS WASHINGTON DC 20361	1 1 1
ATTN MICHAEL CALA COMMANDER CENTER FOR NAVAL ANALYSES PO BOX 16268 ALEXANDRIA, VA 22302	1
ATTN JEWC/DVP COMMANDER JOINT ELECTRONIC WARFARE CENTER SAN ANTONIO, TX 78243-5000	1
ATTN CODE 5023 COMMANDER NAVAL AIR DEVELOPMENT CENTER JOHNSVILLE WARMINSTER, PA 18974	1
ATTN JOHN MONTGOMERY COMMANDER NAVAL RESEARCH LABORATORY TACTICAL EW DIVISION WASHINGTON DC 20375-5000	1
ATTN TECHNICAL LIBRARY COMMANDER NAVAL AIR WEAPON CENTER CHINA LAKE, CA 93555-6001	1

	Copies
ATTN TECHNICAL LIBRARY COMMANDER NAVAL SECURITY GROUP COMMAND 3801 NEBRASKA AVE NW WASHINGTON DC 20393	1
ATTN TECHNICAL LIBRARY COMMANDER NAVAL AIR WARFARE CENTER WEAPONS DIVISION POINT MUGU, CA 93042-5000	1
ATTN SIGNT/EW COMMANDING GENERAL MARINE CORPS RESEARCH DEVELOPMENT AND ACQUISITION COMMAND QUANTICO, VA 22134-5080	1
ATTN TECHNICAL LIBRARY DIRECTOR DEFENSE ADVANCED RESEARCH PROJECTS AGENCY 3701 N FAIRFAX DR ARLINGTON, VA 22203-1714	1
ATTN W44 DIRECTOR NATIONAL SECURITY AGENCY 9800 SAVAGE RD FORT MEADE, MD 20755-6000	1
ATTN TECHNICAL SUPPORT GROUP DIRECTOR NAVAL TECHNICAL INTELLIGENCE COMMAND 4301 SUITLAND RD WASHINGTON DC 20390	1
ATTN HUGH VANLANDINGHAM VIRGINIA POLYTECHNIC INSTITUTE AND STATE UNIVERSITY DEPARTMENT OF ELECTRICAL ENGINEERING BLACKSBURG, VIRGINIA 24061-0111	1

INTERNAL DISTRIBUTION	Copies
A	4
B	4
B32/BLAIR	1
C	1
D	1
D25	1
D4	1
E	1
E231	10
E232	2
E281/HALI	1
F	1
F01	1
F02	1
F07/DORSEY	1
F0X	1
F10	4
F20	5
F21	20
F22	1
F23	1
F24	1
F30	3
F40	2
F41	2
F42	2
F43	1
F50	2
G	1
G52	1
J	1
K	1
N	1
N05/GASTON	1
N20/HENDERSON	1
N22	1
N24	1
N25	1
N70	2
N74/GIDEP	1
R	1

REPORT DOCUMENTATION PAGE

Form Approved
OMB No 0704-0188

1. AGENCY USE ONLY *(Leave blank)*	2. REPORT DATE	3. REPORT TYPE AND DATES COVERED
	December 1992	

4. TITLE AND SUBTITLE
Tracking Filters for Precision Electronic Support Measures (ESM) Systems

5. FUNDING NUMBERS

6. AUTHOR(S)
J. Darren Parker

7. PERFORMING ORGANIZATION NAME(S) AND ADDRESS(ES)
Naval Surface Warfare Center
Dahlgren Division (F21)
Dahlgren, VA 22448-5000

8. PERFORMING ORGANIZATION REPORT NUMBER
NSWCDD/TR-92/503

9. SPONSORING/MONITORING AGENCY NAME(S) AND

10. SPONSORING/MONITORING AGENCY REPORT NUMBER

11. SUPPLEMENTARY NOTES

12a. DISTRIBUTION/AVAILABILITY
Approved for public release; distribution is unlimited.

12b. DISTRIBUTION CODE

13. ABSTRACT *(Maximum 200 words)*

Both an α,β and an α,β,γ filter have been used to estimate the true bearing and elevation of high-speed maneuvering targets from measurements made by a shipboard electronic support measures (ESM) sensor. The motivation for this research is the need for correlating radar and ESM tracks. Four Mach 3 target trajectories with a data rate of 10 Hz and a measurement noise standard deviation of 0.1 deg were used to test the filters. Consistency tests were used to determine the best values for the steady-state gains of the filters. Both filters are computationally simple and provide estimates of greater accuracy than the ESM measurements. It was determined that an α,β filter provides better estimates than an α,β,γ filter for most of the tested target trajectories. Two exceptions are the bearing for a Mach 3 crossing target at ranges less than 20 km and the elevation of a Mach 3 target at ranges less than 5 km. Both filters are recommended for radar-to-ESM track correlation research. The α,β filter should be tested first, since it is simpler and provides better estimates for most of the cases tested.

14. SUBJECT TERMS
Electronic Warfare (EW) α,β and α,β,γ Filters Kalman Filters
Electronic Support Measures (ESM) Correlation Passive Tracking

15. NUMBER OF PAGES
133

16. PRICE CODE

17 SECURITY CLASSIFICATION OF REPORT	18. SECURITY CLASSIFICATION OF THIS PAGE	19. SECURITY CLASSIFICATION OF ABSTRACT	20. LIMITATION OF ABSTRACT
UNCLASSIFIED	UNCLASSIFIED	UNCLASSIFIED	UL